Tracers of Rapid Transport in the Lower Stratosphere

Thesis by

Elisabeth Jeanne Bailey Moyer

In Partial Fulfillment of the Requirements for the Degree of Doctor of Philosophy

California Institute of Technology

Pasadena, California

United States of America

2001

(Submitted October 6, 2000)

For my father

Carl Franz Bailey Moyer

1937 - 1997

who told me:

"Never wear shoes that

make you walk slower than the men."

Acknowledgements

The work presented in this thesis would not have been possible without the assistance and involvement of a great many people. I am indebted to my advisor, Yuk Yung, for his unending enthusiasm about science and for the freedom to pursue my own enthusiasms. Yuk inspired this entire endeavor, and did so in a way characteristic of both his joy in sharing ideas and his respect for the opinions of graduate students: one day he handed me a plot of ATMOS data that interested him and asked me what I thought it meant. The work described here represents my attempt to answer that question, as I followed that thread where it took me.

The design and construction of the WISP instrument was undertaken as part of the group of Chris Webster at JPL, who gave me the facilities and the field experience necessary to do it. The instrument is based on the design of the many other diode laser absorption spectroscopy instruments built by the group; designing a new instrument would have been impossible without this heritage and without the expertise and assistance of group members, including Chris Webster, Bob Herman, David Scott, Greg Flesch, and Jim Swanson.

I am indebted also to the many people in the atmospheric science community who lent their advice, assistance, and support, from my entrance in graduate school through the completion of WISP. Their conversations and willingness to teach are part of what has made science rewarding for me. In particular I would like to thank Fred Moore, David Fahey, Tommy Thompson, and Ross Salawitch. WISP would not have flown without the support of Randy Friedl and Marty Ross, who sponsored the instrument onto the payload for ACCENT. Ross Salawitch invited me to join the ATMOS science team. Bill Irion and Hope Michelsen were generous collaborators on the ATMOS data. Jack Kaye was

a benevolent force from above. Paul Wennberg and Ed Stolper at Caltech were patient providers of much-needed advice. Paul first suggested the ACCENT campaign as a flight opportunity and prodded me to make it happen; Ed spent many hours attempting to explain to me how the world actually works, with some degree of success. Irma Black resourcefully juggled the uncertain finances of this project and proofread the resulting thesis. I am also deeply grateful to the many others who became personally invested in the success of WISP, including the NASA Johnson staff, the Dyncorp WB-57 mechanics, and Paramount Machine and other shops that heroically turned parts around on a day's notice to meet flight deadlines.

WISP could not have been built without Thomas Moyer, my brother and chief engineering support, who took eight months of his time and a substantial cut in pay to help bring this project from concept to hardware. Tom was responsible for the mechanical design of the instrument and for a large part of my education. I value the practical skills of building apparatus that he taught me, but equally so the principles of engineering design and project management he instilled in me. I learned from him how to do a structural analysis; calculate an aerodynamic load; use torque-stripe paint; load a truck; put a contract out to bid; keep a bill of materials; clean your workbench at the end of the day; design with the machinist's time in mind; appreciate the beauty of off-the-shelf components; and a thousand other things that served me well then and will in the future. I treasure the time we spent working together.

Many other people played roles not directly related to the thesis work but vital to its success. My parents showed me what it means to keep learning for a lifetime. Mike Brown gave me eight years of wise editing and moral support. Sanjoy Mahajan was my sturdy shoulder, my physics encyclopedia, and my Lois Weisberg; he always managed to rekindle my interest in science when the spark faded. Bill Holzapfel taught me to solder, and gave me a model of an experimental scientist to aspire to. Ariel Anbar showed me that being a graduate student was no bar to scholarly curiosity and independent thought. Oliver Chadwick was uncommonly helpful during my brief foray into soil science. David Paige taught me to roll a kayak and make a telemark turn. Ashwin Vasavada named

WISP. Maria Orive and Geoff Bower were there when my father died. Mario Miralles and Brenda Bork gave me roots in the Millard Canyon community. For my connection to the San Gabriel mountains, which kept me sane, I am grateful to Leo Eisner, Erik Winfree, and the others who trekked up the long hill to visit, to the extended families of Pasadena mountain bikers and canyon dwellers, and to the many people I was privileged to spend time with who loved the mountains as I did.

This work was funded in part by an NSF Graduate Fellowship, by a NASA Graduate Fellowship in Global Change Science, and by a California Institute of Technology President's Fund grant.

῾ Χαῖρ', Ἰθάκη. μετ' ἄεθλα, μετ' ἄλγεα πικρὰ Θαλάσσης
ἀσπασίως τεὸν οὖδας ἱκάνομαι.

ANON., Anthologia Palatina,
Book IX no. 458 II. 1-2

Abstract

This thesis consists of three parts, each related to the use of tracer measurements to diagnose the small-scale structure and mechanisms by which air is transported, both vertically and horizontally, in the lower stratosphere.

1. I demonstrate that the isotopic composition of water vapor can diagnose rapid convective transport across the tropopause. I use data from the space shuttle- and balloon-borne Fourier transform solar occultation spectrometers ATMOS (Atmospheric Trace MOlecule Spectrometer) and Mark-IV to reconstruct the mean deuterium isotopic composition of water entering the stratosphere. Initial δD is -670 per mil (33% of deuterated water retained). I construct a one-dimensional model simulating isotopic fractionation during ascent to the tropopause and demonstrate that for all but the most rapid ascent, virtually all deuterated water is stripped from an air parcel in the last few kilometers of the uppermost troposphere. The observed stratospheric δD is then far heavier than modeled depletions under most conditions. I conclude that the observations can be matched only by substantial evaporation of lofted condensate or by ascent in highly supersaturated conditions, and infer that mean stratospheric air must have experienced rapid convection to at least near-tropopause altitudes. This study serves to demonstrate that the isotopic composition of water vapor is a valuable tracer that can be used to constrain mechanisms of stratosphere-troposphere transport.

2. I use *in-situ* tunable diode laser measurements of CO, H_2O, and N_2O taken over Fairbanks, AK to show rapid transport by streamers of air in the lower stratosphere. I was part of a team that used ALIAS and JPL-H2O, two tunable diode laser spectrome-

ters built by the Webster group of the Jet Propulsion Laboratory, to obtain data in the upper troposphere and lower stratosphere on 21 ER-2 flights between April and September, 1997, during the POLARIS (Photochemistry of Ozone Loss in the Arctic Region In Summer) mission. I use this dataset to identify episodes of rapid polewards advection in the lowermost stratosphere in which filaments of air move from tropics to 65 N latitude in weeks. I find that the lowermost stratosphere is a region of intense filamentary activity, but that tropical filamentation is absent above the 420 K surface, in contradiction to the results of previous trajectory simulations. Individual filaments extend from the "overworld" stratosphere to the local tropopause, showing that the boundary between "overworld" and "middleworld" is not a true dynamical barrier. The filamentation is strongly seasonal, in agreement with previous trajectory results, but with a longer period of activity. I conclude that the tropopause transition layer extends to 420 K θ, and that transport in this layer is coupled to changes in the tropospheric subtropical jet.

3. I describe the design and construction of a new lightweight open-path tunable-diode-laser instrument for measurements of water vapor isotopic composition from aircraft platforms. I initiated and led an effort to design and build an instrument capable of resolving transport issues such as those mentioned in (1). WISP (Water Isotope SPectrometer) is a 3-channel tunable-diode-laser spectrometer, with two mid-infrared and one near-infrared laser sources. Light is injected into a 94-pass Herriott cell for a total of 94 meters of pathlength. The expected threshold sensitivity is a few parts in 10^5 absorption. Detection of HDO has an expected SNR > 10 up to near-tropopause altitudes. All isotopomers of water vapor, and methane, are detected in a single scan, allowing improved accuracy as common systematics drop out of the ratio. I led the integration of the instrument on NASA's WB-57 aircraft as part of the ACCENT mission. The instrument can provide a versatile tool for tracer measurements in the tropopause region.

Contents

List of Figures

Chapter 1

Introduction

1.1 Stratospheric circulation and strat-trop exchange

Nearly six percent of the total mass of tropospheric air each year crosses the boundary of the tropopause and enters the stratosphere. It has been inferred since the 1940's, when Brewer first measured stratospheric water vapor, that the bulk of transport to the stratosphere occurs in the tropics, where the tropopause is highest and coldest and therefore capable of coldtrapping air to the observed stratospheric dryness (9). Measurements of tracers such as water vapor, bomb-produced ^{14}C, and anthropogenic chlorofluorocarbons and modeling of the residual circulation based on assimilated datasets have given us a broader understanding of the annual mass flux, geographic location and seasonal variability of the exchange of air between troposphere and stratosphere (e.g. 47, 60, 62). Despite nearly a half-century of scientific investigation, however, we still lack an understanding of the physical mechanism driving that exchange. In particular, we do not know whether the bulk of the mass flux is carried by localized convective cumulus towers that rise from near sea-surface levels in the tropics and penetrate the tropopause, or whether it results from more widespread and gradual regional uplift (e.g. 14, 37, 47). The last decade has witnessed a reversal of opinion on STE, from the assumption that air moves into the stratosphere primarily in convective events to an assumption it does so in widespread

gradual ascent with no convective influence. The discovery of widespread coverage of near-tropopause cirrus clouds has lent support to the scenario of more gradual ascent (e.g. 72, 42). However, existing data cannot definitively confirm or disprove either scenario. Nor can they determine what governs the water vapor content of the stratosphere, or explain its apparent increase in the last several decades, which cannot be accounted for by changes in tropopause temperature. The set of suggested explanations is diverse, including that the region of ascent is widening and that dehydration of air entering the stratosphere is set by overshooting convection even if mean ascent is gradual (68). It is both remarkable and disturbing that in the face of a potentially changing climate we lack a predictive theory of how air and water enter the stratosphere.

The distinction between the proposed mechanisms is significant for stratospheric robustness to anthropogenic changes. If air injected into the stratosphere is derived from near the earth's surface and transported upwards in rapid convection without significant mixing, then short-lived pollutants may reach the stratosphere and pose a danger to its chemical stability, but emissions from near-tropopause aircraft are a negligible concern. If, on the other hand, the dominant mechanism for stratospheric injection is gradual ascent through the uppermost troposphere, then the relative concern over surface vs. aircraft emissions is inverted. Even if convection influences only stratospheric water content, and not the bulk circulation, it still has strong implications for climate. Water vapor is the primary greenhouse gas, with twice the direct radiative impact of carbon dioxide, and has an equally important indirect effect through the formation of clouds (25, 54). It is essentially the sole source of HO_x radicals, the dominant oxidant in the troposphere and lower stratosphere. If water vapor content is governed by convection, it is likely more responsive to changes in tropical ocean surface temperatures, and hence vulnerable to global temperature trends. In general, our ability to predict the stratospheric consequences of anthropogenic perturbations in the troposphere is severely hampered if we lack full understanding of how the two parts of the atmosphere interact. Gaining that understanding is a major priority in atmospheric research.

Figure 1.1 shows the current view of stratosphere-troposphere exchange (STE) and

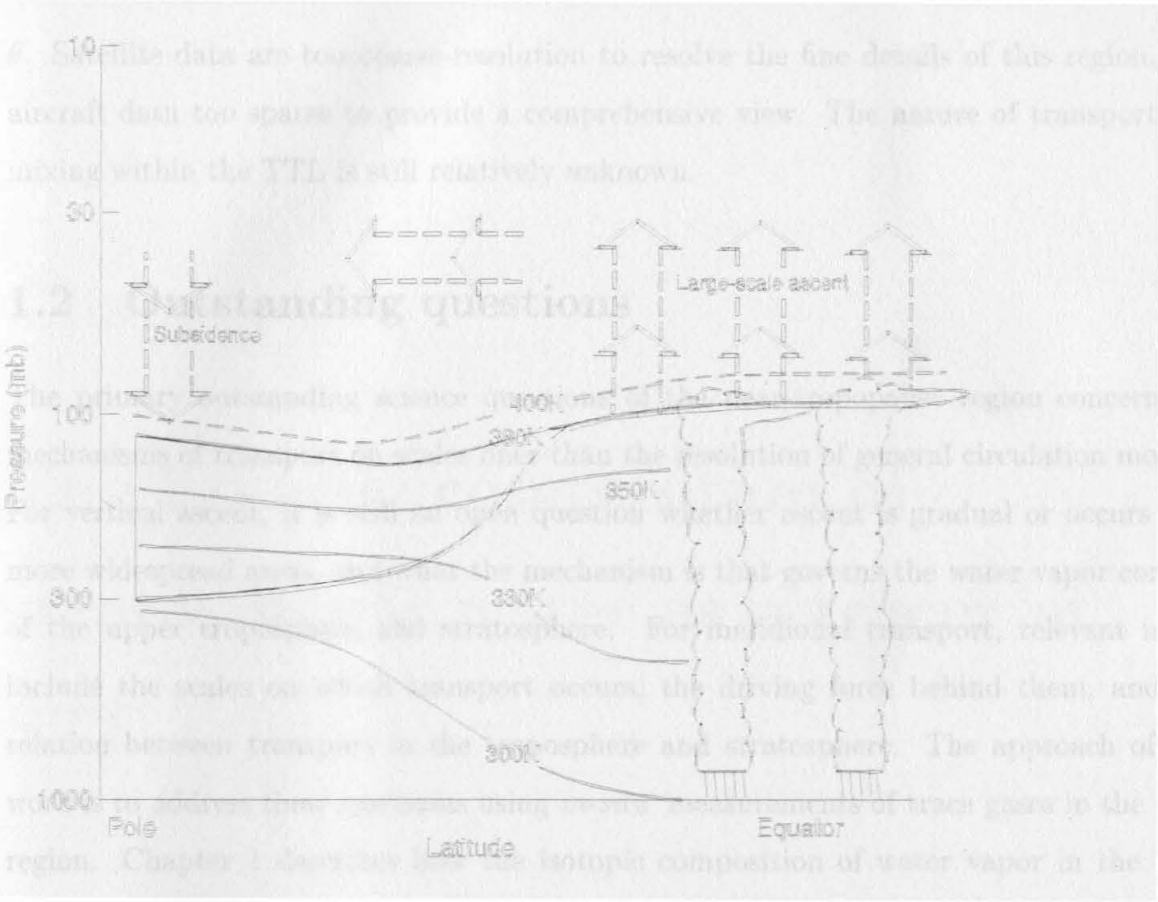

Figure 1.1: Schematic diagram of stratosphere-troposphere exchange, from (29).

stratospheric circulation. Air is assumed to ascend in the tropics via some combination of convective or gradual processes. Meridional transport to higher latitudes is presumably driven by extratropical wave forcing, but the location of that forcing is uncertain (29); it may lie at the polar end of the midlatitudes, or in the subtropics (Holton, J. *pers. comm.*). The structure of that transport is also unclear. The region between the 380 K θ surface, (the tropical tropopause level) and the slanting mid- and high-latitudes tropopause is known as the "middleworld", where tropospheric and stratospheric air can mix along isentropes. In the "overworld" above, all air must have entered by ascent in the tropics. There is growing consensus, however, that the 380 K surface is not a sharp distinction between two disparate regions, and that the vicinity both above and below 380 K, represents a "tropopause transition region" (TTL) in which transport is enhanced and meridional mixing is strong. In this figure the TTL is shown as extending to 400 K

θ. Satellite data are too coarse-resolution to resolve the fine details of this region, and aircraft data too sparse to provide a comprehensive view. The nature of transport and mixing within the TTL is still relatively unknown.

1.2 Outstanding questions

The primary outstanding science questions of the near-tropopause region concern the mechanisms of transport on scales finer than the resolution of general circulation models. For vertical ascent, it is still an open question whether ascent is gradual or occurs over more widespread areas, and what the mechanism is that governs the water vapor content of the upper troposphere and stratosphere. For meridional transport, relevant issues include the scales on which transport occurs, the driving force behind them, and the relation between transport in the troposphere and stratosphere. The approach of this work is to address these questions using *in-situ* measurements of trace gases in the TTL region. Chapter 1 describes how the isotopic composition of water vapor in the TTL can be used the discriminate between mechanisms of STE, and chapters 4 and 5 describe the construction of an instrument to measure it. Chapters 2 and 3 examine fine-scale filamentary horizontal transport in the TTL using *in-situ* measurements of CO, a short-lived tracer of tropospheric origin, and draw inferences about its distribution, seasonal variation and dynamical forcing.

Chapter 2

The isotopic composition of stratospheric water as a tracer of STE

2.1 Abstract

Measurements of the isotopic composition of stratospheric water by the ATMOS instrument are used to infer the convective history of stratospheric air. The average water vapor entering the stratosphere is found to be highly depleted of deuterium, with δD_w of -670 $\pm$ 80 (67% deuterium loss). Model calculations predict, however, that under conditions of thermodynamic equilibrium, dehydration to stratospheric mixing ratios should produce stronger depletion to δD_w of -800 to -900 (80-90 % deuterium loss). Deuterium enrichment of water vapor in ascending parcels can occur only in conditions of rapid convection; enrichments persisting into the stratosphere require that those conditions continue to near-tropopause altitudes. We conclude that either the predominant source of water vapor to the uppermost troposphere is enriched convective water, most likely evaporated cloud ice, or troposphere-stratosphere transport occurs closely associated with tropical deep convection.

2.2 Introduction

The original Brewer-Dobson proposal for the circulation between troposphere and stratosphere involved slow ascent throughout the tropics, where the tropopause is highest and coldest, with the cell extending some distance into the troposphere (9). While subsequent research has confirmed the tropics as the location of most troposphere-stratosphere transport (abbrev. STE by convention) (e.g. 63), the speed and scale of the processes which move air across the tropopause and into the stratosphere are not yet well known. Tropopause temperature measurements suggest that the scale of STE may be more localized or episodic, since much of the tropical tropopause is too warm to freeze-dry air to observed stratospheric values (e.g. 20). Theories of STE now span a large range of temporal and spatial scales, from extremely rapid injection during isolated convective events which perturb the local temperature structure (1-10^3 km^2) (e.g. 13), to slower seasonal ascent over the coldest subregion of the tropics ($\approx 10^7$ km^2) (47), with proposals for dehydration in the stratosphere itself during gravity-wave temperature fluctuations allowing ascent over even larger areas (52).

Upward mass transport in the underlying tropical troposphere, on the other hand, is believed to be highly localized and inhomogeneous, occurring primarily in convective cumulus towers (57). STE may result simply from the extension of some cumuli into the stratosphere proper, or it may represent a qualitatively different process, with a transition between a middle troposphere in which upward motion is dominated by localized convection and an uppermost troposphere where slower mean motions are also important (e.g. 30). Observations of stratospheric water vapor content have not provided a means of resolving between these scenarios.

These scenarios differ in the process by which ascending air is dehydrated. During gradual ascent, dehydration must proceed by simple condensation and fallout of moisture. Dehydration in convective systems can be more complicated, since cumulus towers can carry with them enormous quantities of water as ice – near-tropopause ice:vapor ratios can exceed 100 (35) – and final water vapor mixing ratios may be net of both evaporation and

condensation. Dehydration in stratospheric waves may also involve cycles of condensation and re-evaporation, but without significant transport of ice particles. Determination of not only the final water content of stratospheric air, but of the process by which that content is reached, can thus discriminate between transport scenarios, providing insight into the larger question of how air is exchanged between troposphere and stratosphere.

We propose that the isotopic composition of stratospheric water vapor is a useful tracer for this purpose, because it records the condensation and evaporation experienced by each air parcel that crosses the tropopause. Whenever several phases of water are present in thermodynamic equilibrium, the heavier isotopes partition preferentially into the condensed phases. As water condenses out of an air parcel, then, deuterated water is preferentially removed and the residual vapor is progressively lightened. The degree of preference, or fractionation factor, α ($\alpha \equiv$ D:H$_{condensate}$ / D:H$_{vapor}$), is quite strong for deuterated water, with α ranging from 1.08 at room temperature to over 1.4 for ice condensation at the $\approx$ 190 K tropical tropopause (40, 44). Stratospheric air, with a water vapor concentration four orders of magnitude less than that at sea surface, should be highly depleted in deuterium, but the exact degree of depletion will depend on the convective history of that air.

2.3 ATMOS observations of δD_W

Observations of stratospheric deuterated water by the Atmospheric Trace Molecular Spectroscopy (ATMOS) Fourier transform infrared spectrometer over the last decade provide the first large database of isotopic compositions that can be applied to the problem of STE. There have been few previous reported measurements of HDO and H_2O in the lower stratosphere, where accurate spectroscopic measurement of both species is difficult, with none in the tropics, the presumed source region for stratospheric air and water; nor have there been simultaneous measurements of CH_4 and CH_3D. Observations in the mid-latitudes stratosphere have found water vapor strongly depleted of deuterium, but with δD_w increasing with altitude from $\approx$ -600 ‰ at 20 km to -350-450 ‰ at 35 km.

(58, 59, 16, 10, 51). (Deuterium content is given in δ notation, where δD_w is the fractional difference, in per mil, of the D/H ratio of measured water from that of standard mean ocean water (SMOW), at 1.5576×10^{-4} (23).) This increase has been presumed to be the result of oxidation of isotopically heavier atmospheric methane. (e.g. 17, 59).

This analysis uses data from all four ATMOS missions from 1985-1994, a total of 68 occultations in which HDO, H_2O, and CH_4 were retrieved (filters 2,9), and 67 in which CH_3D was retrieved (filter 3). Only occultations in the polar vortices, where dehydration on polar stratospheric clouds produces additional isotopic effects, have been excluded. Latitudinal coverage is near-global (24% tropical, 18% mid-latitudes, 58% high latitudes). The ATMOS instrument, coverage, and data reduction procedure are described in detail elsewhere (22, , and references therein).

Water vapor isotopic compositions are corrected for changes occurring in the stratosphere by subtraction of methane-derived contributions of HDO and H_2O at each data point; conservation of hydrogen and deuterium between water and methane in the stratosphere is demonstrated from these same data by (31, 1). Initial concentrations of CH_4 and CH_3D are taken as 1.7×10^{-6} and 9.9×10^{-10}, respectively, from (5) and the filter 3 $\ln[CH_3D]$: $\ln[CH_4]$ relationship (31). CH_3D concentrations are inferred from observed CH_4 in filters 2 and 9 using this relationship. This correction yields the isotopic composition of water as it first crosses the tropopause, with no assumptions as to the initial concentration of that water.

Figure 2.1 shows measurements of the isotopic composition of stratospheric water from all four ATMOS missions, before (1a) and after (1b) correction for methane contribution. After correction there is no trend in composition with altitude above 20 km. Slight deviations below 20 km are most likely due to the increased error in retrieval of water concentrations. The mean stratospheric water is highly depleted, with a $\overline{\delta D_w}$ of -670 $\pm$ 80 ‰ or 67% loss of deuterium (weighted mean of all extravortex observations from 18-32 km; error represents 1 σ of the distribution + systematic error.)

There is no significant variation in $\overline{\delta D_w}$ with mission, filter, or latitude, over the 9 year span of these measurements, nor in comparison with previous measurements dating

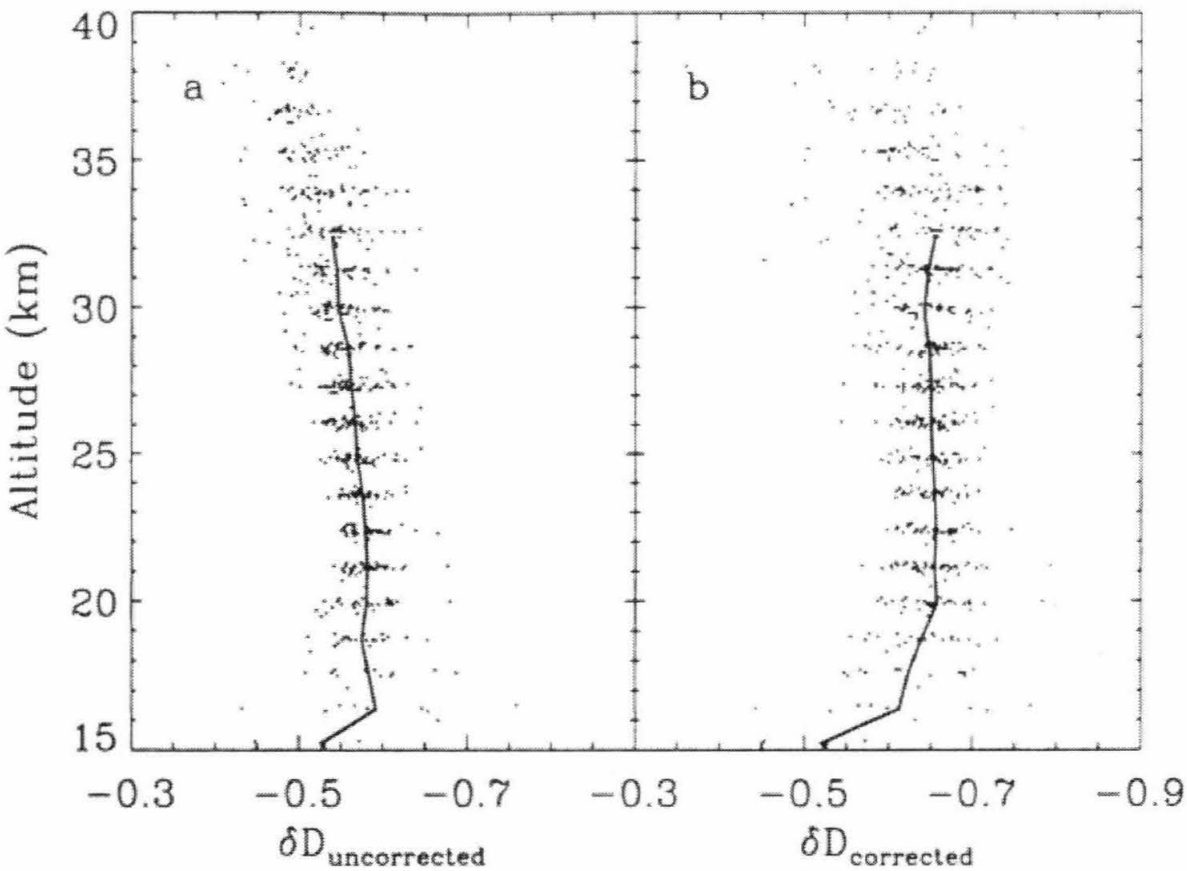

Figure 2.1: ATMOS measurements of the deuterium content of stratospheric water. The left panel shows uncorrected observations; the right panel the same data with the estimated contribution of H_2O and HDO from methane oxidation subtracted. The units are fractional difference from standard mean ocean water, or δD in per mil $\times 1000$. Data shown are those with $\text{error}_{H_2O} \leq 10\%$, $\text{error}_{CH_4} \leq 10\%$, and $\text{error}_{HDO} \leq 30\%$, $\approx 75\%$ of the total dataset. Solid lines represent weighted mean profiles from 15-32 km. Distribution σ for corrected δD_w is 35 ‰; total error with systematic errors is 80 ‰.

to 1980 (e.g. 51). Mesoscale or seasonal variability in δD_w of entering stratospheric air should be discernible only in the lower tropical stratosphere, where ATMOS HDO data is limited to only four occultations (28 observations). The distribution of δD_w values in these data is similar to that of the whole dataset, a Gaussian distribution with a peak at -680 ‰ and a width of 90 ‰, with no outliers that might suggest contributions from isotopically distinct processes. Although isentropic mixing should erase much spatial inhomogeneity, this consistency suggests that stratospheric water enters with a characteristic isotopic signature similar to the mean stratospheric value.

2.4 Implications of stratospheric δD_W

To explore the implications of the isotopic signature of stratospheric water, we have developed a multi-phase cloud model that computes isotopic trajectories during the ascent of air to the tropopause. The model represents the one-dimensional lifting of air parcels, with the concentrations and isotopic compositions of vapor, liquid, and ice tracked throughout. Air parcels are stepped upward until the water vapor mixing ratio equals the mean lower stratospheric value in these data of 3.6 ppm. (Model results are robust with respect to this value; variations in water vapor of $\pm$ 20% produce only minor isotopic changes). Isotopic fractionation occurs during the initial evaporation of seawater, the condensation of liquid and ice, and the conversion of liquid to ice as the cloud glaciates. Cloud liquid is allowed to re-equilibrate with cloud vapor, while ice is effectively removed from the vapor. Free parameters of the model are: surface temperature and relative humidity, temperatures of the onset of ice nucleation and the completion of glaciation, the relative importance of droplet freezing to evaporation and re-deposition during glaciation, the degree of supersaturation over ice in the final stages of ascent, and the precipitation (or lack thereof) in all condensing stages. Although simplified, the model captures the full range of possible conditions for a simple convective updraft.

In the first set of model runs isotopic partitioning was assumed to occur at thermodynamic equilibrium in all stages, with the temperature dependence of α taken from

(40, 44). In these conditions, model-generated final isotopic compositions at the tropical tropopause in these conditions are all considerably lighter than observed stratospheric water (Figure 2a). Stratospheric water vapor is highly depleted of deuterium, but it is less depleted than would be expected given the extent of dehydration experienced. While at lower altitudes, where liquid is present, vapor isotopic compositions can be substantially altered by choice of model parameters, all trajectories converge during the nearly 7 km of ascent in ice-only conditions from the homogeneous freezing point of liquid water at $\approx$ 233 K to the tropical tropopause at $\approx$ 190 K. Dehydration in those last kilometers strips out virtually all deuterium: vapor concentration must drop by a factor of over a hundred, with strong fractionation at α = 1.3-1.4, so vapor D/H must drop by over 80% over this altitude range alone. Even if no depletion occurred until the onset of ice condensation, the final δD under these conditions would still be less than -800.

The deuterium content of stratospheric water can be increased only if we postulate that (1) air parcels in this 10-17 km region receive additional contributions from sources that are not in equilibrium with the vapor, or (2) isotopic fractionation is weaker than equilibrium values imply. For postulate (1), lofted cloud ice is the only plausible source of non-equilibrated water in the upper troposphere or lower stratosphere. While liquid water can rapidly exchange and equilibrate with its environment, the isotopic composition of ice remains essentially fixed (33). Ice particles carried upwards from their altitudes of condensation thus preserve anomalously heavy isotopic compositions in relation to their surrounding vapor, and, if later evaporated, serve to enrich the vapor D/H ratio.

The second postulate, that isotopic fractionation has been reduced, is possible during ice deposition in highly supersaturated air parcels, where kinetic effects prevent the vapor and condensate from achieving their equilibrium isotopic partitioning (33). Figure 2b shows isotopic trajectories calculated using this kinetic fractionation, for a range of supersaturations (S). Because the condensing material extracts less deuterium, the residual vapor remains heavier; at S of 1.5 to 2 (150 - 200 %), depending on convective parameters, sufficient deuterium is left at the tropopause to match the observed stratospheric isotopic composition.

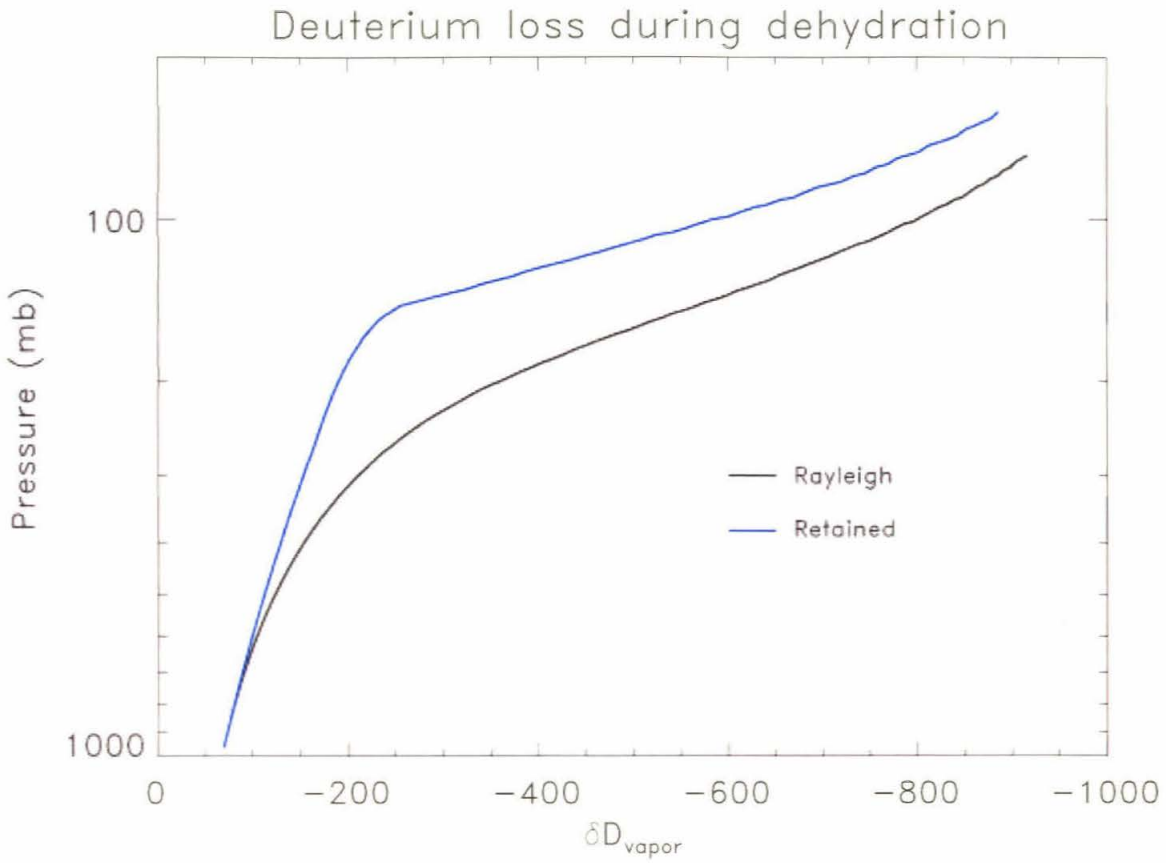

Figure 2.2: Model calculations of water vapor δD during ascent, for conditions of thermodynamic equilibrium. The two cases here define the envelope of all possible scenarios for deuterium loss during ascent, with the assumption of no supersaturation or mixing. The blue profile represents the case where all liquid condensate is retained with the air parcel up to the freezing level, re-equilibrating with the vapor, and where the phase transition occurs by simple freezing of cloud droplets.

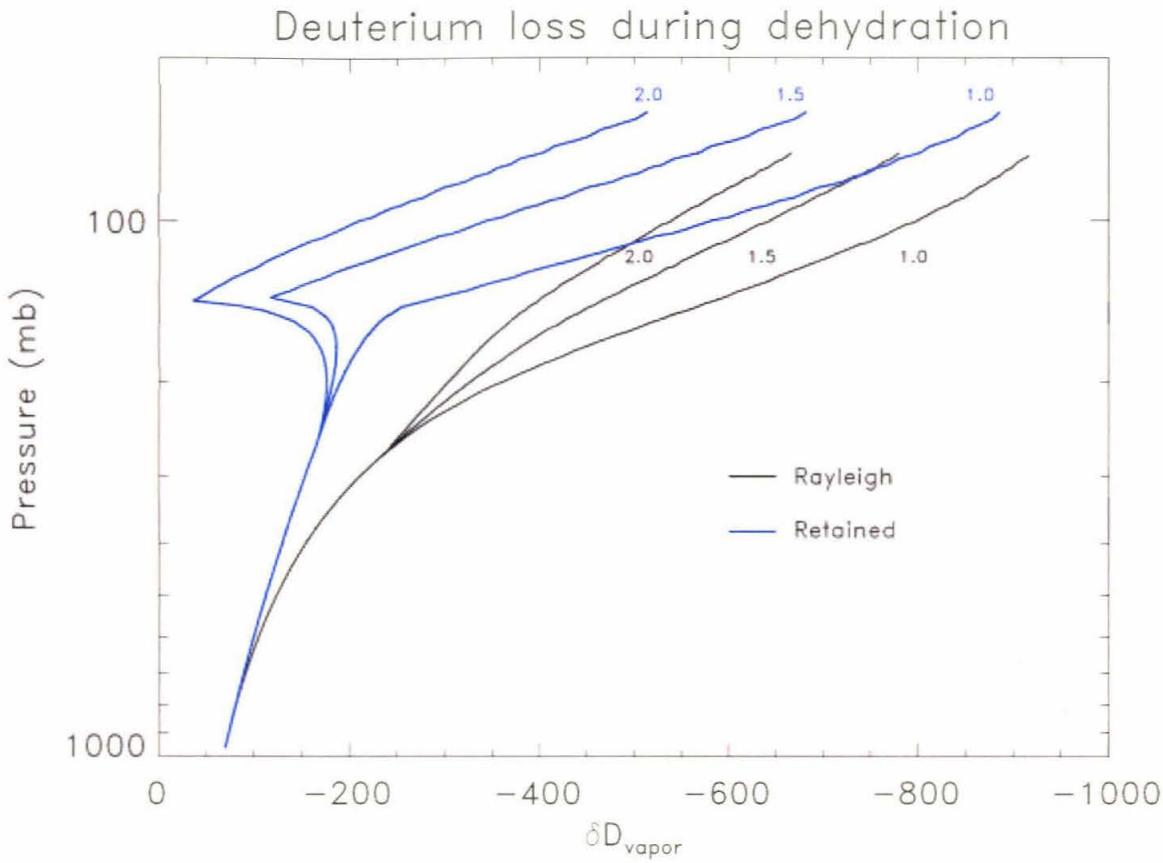

Figure 2.3: Model calculations showing the isotopic composition of water vapor during ascent to the stratosphere, with fractionation factor modified by supersaturated conditions. As in figure 2.2 the black and blue lines represent immediate removal and total retention of liquid condensate, respectively, and bracket the full range of possible δD values. High-S conditions both reduce the fractionation factor and allow for strong enhancements during the transition from liquid-solid in the liquid-retaining cases. Here glaciation is allowed to proceed by evaporation of droplets and recondensation as ice; at high S, $\alpha_{\text{vapor}-\text{ice}}$ is less than $\alpha_{\text{vapor}-\text{liquid}}$ and deuterium is pumped into the vapor. Complete vapor deposition of ice should be regarded as an endmember case only.

Either of these scenarios is possible only in strong convective systems. Supersaturations of 1.5 - 2 can be sustained only by updraft velocities typical of the strongest cumulus cores; in steady state, approximately 20 - 50 m/s for the ice particle size distribution observed during the STEP campaign in tropical near-tropopause cloud systems (e.g. 35, 61, 53) Ice crystal evaporation, on the other hand, can significantly alter the isotopic composition of vapor only if the ice crystals are substantially out of equilibrium with that vapor, i.e. if evaporation occurs at altitudes significantly higher than the level of condensation, again a condition possible only in strong convective updrafts. (Temperature fluctuations of 5-8 degrees in stratospheric waves can produce only minor enrichments.)

Deuterium enrichment by either of these processes must occur near the tropopause in order for some effect to persist into the stratosphere. Water vapor in a rising air parcel is depleted from its original composition to observed stratospheric values in less than 3 km of ascent at upper tropospheric temperatures, so non-equilibrium deuterium contributions must be occurring in the last 3 km beneath the tropopause. Most water entering the stratosphere must experience convective conditions to at least the uppermost troposphere.

2.5 Conclusions

ATMOS deuterated water data constrain the process of STE to one of two scenarios. In the first, STE is closely associated with deep convection. Actual cross-tropopause transport may occur either as penetrative convection which deposits air above the tropopause or as more gradual ascent in and above mesoscale convective systems; in the latter case the convective systems contributing to STE must reach altitudes of at least 14 to 15 km (for a 17 km tropopause). In the second, STE occurs over wider parts of the tropics, less directly associated with convective systems, but here water in the uppermost troposphere consists almost exclusively of enriched water from convective systems, most likely evaporated cloud ice. Again, this evaporation must occur at 14-15 km altitude or higher.

Further observations in the tropical lower stratosphere and upper troposphere are nec-

essary for discriminating between these possibilities. Isotopic data from the stratosphere alone may be sufficient to demonstrate whether the final dehydration of stratospheric air occurs in slow ascent rather than in convective penetration with admixture of evaporated ice, if a clear seasonal cycle in stratospheric δD_w is detectable. Upper tropospheric data are necessary to determine spatial scales of transport. We conclude that a high priority should be placed on obtaining further tropical measurements of HDO and H_2O at these altitudes, and that these observations should provide substantial additional insight into mechanisms of troposphere-stratosphere transport.

(published as: Moyer, E.J., F.W. Irion, Y.L. Yung, and M.R. Gunson, "ATMOS stratospheric deuterated water and implications for cross-tropopause transport", *Geophys. Rev. Lett.* **23**, 2385-2388, 1996.)

Chapter 3

Meridional transport by fine-scale filaments in the lowermost stratosphere from *in-situ* CO observations

3.1 Introduction

While the mean pattern of meridional air motion in the stratosphere has been known for half a century – rising air in the tropics, and descent at the poles – the last decade has seen a fundamental increase in our understanding of the small-scale characteristics of that transport. A variety of tracer observations and numerical simulations based on assimilated datasets suggest that much of meridional transport in the stratosphere occurs in the form of fast-moving filaments and streamers below the resolution of general circulation models. The importance of filaments was first noted in the context of the annual breakup of the polar vortices (e.g. 49), which seem to erode by spinning off filaments of polar air that move equatorward and eventually mix with their surroundings in the mid-latitudes. Similar tongues have been observed shedding off the subtropical transport barrier and

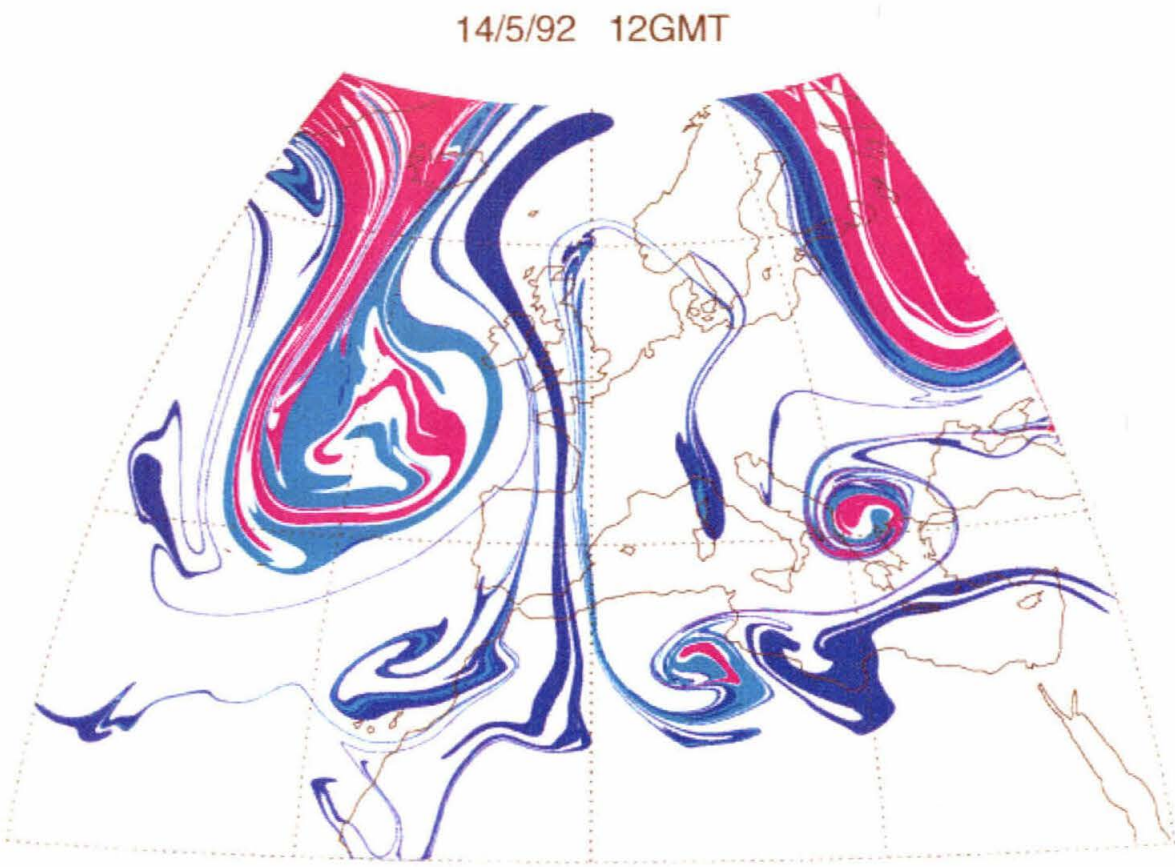

Figure 3.1: Contour advection calculations of filaments on a 320 K isentrope, from *Holton et al. 1995.*

moving poleward from the tropics (e.g. 39, 55, 70), and trajectory calculations support the idea that some portion of the mean equator-to-pole circulation of the Brewer-Dobson cell is accomplished by individual rapidly-moving planetary-scale streamers of air (figure 3.1).

Stratospheric filaments have been observed in a variety of satellite and *in-situ* tracer observations (e.g. 39, 71, 55, 70), but these data have not been sufficient to fully characterize their climatology or quantify the total mass flux they carry. Satellite data, with typical horizontal resolution in the hundreds of km, cannot see finer-scale features, and *in-situ* data lack broad spatial or temporal coverage. Observations have provided some insight into the extent, frequency, and seasonal variation of filaments, but much of our

understanding of stratospheric filaments derives from trajectory simulations that compute the evolution of tracer contours on an isentropic surface using inferred wind fields (e.g. 12, 74, 73).

These simulations allow broader inferences to be drawn about filamentation. In agreement with the view of wave-carried momentum as the driving force for the meridional circulation, observations of filament generation have long been associated with the breaking of planetary scale waves (e.g. 39). Long-term simulations support this association by showing that the seasonality of filament production corresponds well with the seasonal variation of wave-breaking activity (12, 73, 43). However, the deficiencies of both satellite and *in-situ* datasets mean that the broader conclusions of trajectory simulations have not been validated by observational data. And despite the substantial effort devoted to simulations in the last decade, there remain outstanding questions about the structure, distribution, seasonality, and driving force of tropical filamentation, especially in lower stratosphere. Below we review the body of observations and simulations made to date, and discuss those issues which are yet unresolved.

3.1.1 Previous observations

Satellite data

Satellite observations to date have detected filaments only in the middle stratosphere and at coarse resolution, but are invaluable for providing evidence of seasonal variation in filamentation. Satellite datasets in which broad filaments have been seen moving poleward out of the tropics include LIMS ozone (39), SAGE-II aerosol after the Pinatubo eruption (70), CLAES N_2O (55), MLS water vapor (38, 55), and CRISTA N_2O and HNO_3 (36). In all of these studies, filaments were observed during local late fall to early spring months, and several studies covered a sufficiently long period to map the seasonal variation in filamentation. *Leovy et al. 1985* analyzed northern hemisphere (NH) data from October 1978 to May 1979, and observed filaments only during November-March. In their 1996 paper, *Lahoz et al.* considered water vapor data in and around the Antarctic polar vortex

from April-November 1992 (the equivalent of NH October-May), and saw evidence of advection of mid- of low-latitudes air during July-October (equivalent of NH Jan.-April). In both these studies poleward-moving filaments are seen in the winter hemisphere, and are suppressed or absent during summer.

Satellite observations are less useful for studies of vertical and horizontal distribution of filaments. Although filaments have been seen moving as far as 80 degrees latitude, most satellite studies have not detected filamentation past 50 or 60 degrees, likely because their resolution precludes the detection of fine features. All filament detections have been in the region between 600 and 1100 K in potential temperature ($\approx$ 23-42 km altitude), in part because the observations are biased against detection of features at lower altitudes where the tracer species used have smaller gradients. *Leovy et al. 1985* do conclude, though, that altitudes below 650 K (27 km) comprise a region with less filamentary activity.

In-situ data

In-situ measurements from aircraft or balloons have provided evidence of finer scale features than those detectable by satellite, with filaments observed as narrow as 100 km in width (e.g. 6). The fine spatial resolution of *in-situ* data also aids in observation of filaments in the lower stratosphere where tracer gradients are generally small. The *in-situ* measurements are generally consistent with the seasonal pattern inferred from satellite data, with all observations occurring during local winter months, although *in-situ* observations have not been systematic and prolonged enough for statistical studies of filamentation. The main utility of *in-situ* filament observations to date has been to confirm the accuracy of numerical simulations of fine-scale filamentation.

Poleward-moving filaments have been detected from the ER-2 research aircraft in N_2O, ClO, and potential vorticity, and from aerosol lidar on the DC-8 at altitudes from 400-550 K θ (14-22 km) (e.g. 3, 74, 49). Top altitude for the ER-2 is $\approx$ 550 K, precluding any higher-altitude observations. No balloon observations of tropical filaments have been made. (Balloons have provided a few observations of filaments at higher altitudes, 700-800 K, but all cases were of polar or mid-latitudes air moving equatorward (e.g. 32).)

3.1.2 Numerical simulations

Most of the current understanding of filamentation processes has come from numerical simulations based on inferred wind fields in the stratosphere. Simulations have used both contour advection (CA), in which material contours are passively advected by the prevailing winds, and reverse domain filling (RDF), in which back-trajectories are calculated for a grid of particles and the potential vorticity of their earlier location plotted. Both techniques have produced good agreement with *in-situ* observations on specific dates (e.g. 74, 49). The trajectory simulations provide a wider picture of filamentation in the stratosphere, showing filaments spinning off the polar vortices as they erode, and streaming out from the tropics across the subtropical transport barrier.

Vortex association

Cases are seen in both observational data and numerical studies where filaments are simultaneously stripped from vortex and tropics, with the tropical air eventually reaching the polar jet. This association led to the suggestion that tropical air moves poleward in response to wave-induced disturbances in the polar vortex (70, 49, 74). However, more extensive studies on filamentation at a variety of altitudes and seasons conducted by *Chen et al. 1994* and *Waugh 1996* suggested that filament transport was not well-correlated with the presence of a polar vortex. Both studies show filament production in the NH beginning in fall before the vortex has fully formed, continuing in spring after the vortex has broken up. And in simulations of the 1992 SH winter *Waugh 1996* show filamentary transport from the tropics ceasing in October (equivalent of NH April) even though the Antarctic vortex persisted until November.

Seasonality

While the long-term simulations imply that filamentation does not require the interaction between planetary waves and a polar vortex to occur, the seasonal pattern that simulations produce does still support the idea that filamentation is associated with planetary-scale

wave breaking. In their 1996 study *Waugh* concluded that the onset of strong transport out of the tropics by filaments corresponded almost exactly to the turnaround in stratospheric zonal winds, rising sharply in the NH in late September when winds become westerly and Rossby waves can propagate into the stratosphere (11). They found that the period of strong filamentation continued until early May, when winds turn easterly again. In local summer the mass flux carried by filaments was much reduced, and individual filaments did not extend to high latitudes. Summer filaments also appeared thinner horizontally in the simulations, possibly explaining why they are not detected in satellite datasets (73).

Variations with altitude

The vertical extent of filamentation remains something of an outstanding question, with observations too sparse and most simulations performed only at discrete θ-levels, making individual filaments difficult to follow. Both observations and simulations do suggest that tropical filaments are far thinner than those spun off the polar vortices, and that there may be structural differences between tropical filaments at different altitudes. *Schoeberl and Newman 1995* and *Orsolini et al. 1995* model vortex filaments in the Arctic mid-winter using a much finer grid of θ levels and show entire sheets of high-potential-vorticity air peeling off the vortex in the middle and upper stratosphere. The simulations were run from 400-1300 K θ (14 to 60 km), and in some cases produced vortex filaments with continuous structure throughout that altitude range. Streamers of tropical air, on the other hand, appear never to form sheets spanning the entire stratosphere in the simulations. In the *Waugh 1996* study tropical filaments in the middle stratosphere maintained no connection to filaments in the lower stratosphere: the authors were unable to link any individual filaments across the less-active intermediate region.

Simulations and lower-stratospheric observations suggest that tropical filaments in the middle and lower stratosphere are structurally different, with middle stratospheric filaments much deeper than those at lower altitudes. *Schoeberl and Newman 1995* model middle stratospheric filaments over 300 K θ (15 km) in vertical extent, from 950-1250 K.

In the lower stratosphere, the maximum observed or modeled vertical extent of tropical filaments is about 100 K θ ($\approx$ 5 km). *Plumb et al. 1994*, for example, report aerosol lidar observations of tropical intrusions into the Arctic vortex with shallow vertical structure, from 400-500 K θ (14-19 km), and *Waugh et al. 1994* used ER-2 data to find tropical filaments at mid-latitudes in the same altitude range. The *Waugh 1996* simulation produced some filaments considerably thinner than this: many of the filaments on their 425 K surface could not be traced to the 500 K level less than 4 km above.

Despite the differences in filament structure, both the middle and lowermost stratosphere appeared in the *Chen et al. 1994* and *Waugh 1996* studies to be regions of strong filamentation, with the intermediate altitudes far less active. In each of these studies, CA calculations were run on three different θ-levels from the middle to the lowermost stratosphere: 1100, 600 and 400 K in *Chen et al.*, and 850, 500, and 425 K in *Waugh* Both studies showed a far greater volume of air transported at the middle- and lowermost-stratosphere levels, with comparatively little at the intermediate level. [1] This separation reinforces the suggestion that the middle and lowermost stratosphere represent two distinct regions with distinct filamentation processes. Indeed, what transport was found at the intermediate level in *Waugh 1996* appeared to be not a separate process but simply a by-product of filamentation in the lowermost stratosphere. The authors noted that while some filaments appeared only on their 425 K surface, any filament that appeared in the simulation at 500 K could in fact be traced to the 425 K surface. That is, transport at 500 K occurred only whenever lowermost stratosphere filaments became thick enough to extend to that level.

3.1.3 Discussion

Results from the simulations discussed above suggest that the lowermost stratosphere forms a distinct regime from the middle stratosphere, separated from the middle stratosphere by a relatively inert region. It remains an outstanding question whether that

[1] Because of the drop in density of air with altitude, however, the mass flux in the middle stratosphere is still less than that at 500 K.

distinction extends to the dynamical forcing of the two altitude regions. Although the *Waugh 1996* simulation found that poleward-moving filaments at all levels exhibited the same seasonal behavior, with a sharp increase in activity in late September, the differences between θ-levels led the authors to speculate that filaments in the lowermost stratosphere may be responding to tropospheric disturbances rather than wave breaking at higher altitudes. Rossby-wave breaking may not influence dynamics just above the tropopause; the lower stratosphere has far lower amplitude planetary waves than the middle stratosphere, and zonal winds in the lowermost stratosphere follow tropospheric rather than stratospheric patterns (43). The inferences from trajectory simulations have also not been validated by observational data in the lower stratosphere. Although CA and RDF simulations can be compared to middle stratospheric satellite data, and have been shown to reproduce individual profiles from *in-situ* measurements well, there has as yet been no systematic set of fine-scale lower stratospheric observations over several seasons to which the simulations could be compared. Both validation and determining the characteristics of lower stratospheric filamentation require an *in-situ* tracer dataset taken over several seasons, and with sufficient vertical range to clarify a connection between the lowermost stratosphere and the troposphere. We report here observations from the POLARIS aircraft campaign in April-September 1997, the first *in-situ* dataset which can serve this purpose.

3.2 POLARIS dataset

3.2.1 Mission description

The POLARIS (Photochemistry of Ozone Loss in the Arctic Region In Summer) mission consisted of a series of aircraft and balloon flights over a six-month period based primarily out of Fairbanks, Alaska, at 65 N latitude (48). A payload of twenty instruments obtained simultaneous *in-situ* measurements of a wide variety of tracers in the Arctic lower stratosphere: meteorological variables, aerosols, long- and shorter-lived transport tracers, and

reactive species. Although the primary goal of the mission was to study processes driving summertime ozone losses, the mission also provided a systematic view of transport processes in the high-latitudes lower stratosphere over several seasons. NASA's ER-2 aircraft made 25 flights into and out of Fairbanks in three separate deployments between April and September 1997, carrying a nearly identical instrument payload each time. [2] We report here *in-situ* measurements of CO and N_2O from the ALIAS (Aircraft Laser Infrared Absorption Spectrometer) instrument from the 21 flights on which the instrument was aboard the aircraft (see also 28, 27). The repeated flights allowed us to obtain a baseline characterization of the structure and seasonal variation of filamentation in the lower stratosphere over long period to compare to the results of trajectory simulations.

3.2.2 Transport tracers

CO and N_2O are a complementary pair of transport tracers: the combination of the two measurements allows us to determine the residence time of air in the lower stratosphere over a span from weeks to years. Air in most of the stratosphere is generally assumed to have entered at the tropical tropopause (at 380 K θ) and then moved upward and poleward. Species that undergo photochemical losses in the stratosphere will thus show gradients from tropics to pole, with stronger gradients for species with shorter lifetimes, until the limit that lifetime becomes so short that a species reaches photochemical steady state. For tracers with appropriate lifetimes, measurement of tracer concentration thus provides an estimate of the "age" since the air entered the stratosphere. This estimate is good to only first order, since photolysis rates and reactant concentrations generally vary throughout in the stratosphere, so that the age/loss relationship is a function of the trajectory that air has traveled. In the lower stratosphere, however, the bulk of mass flux is simple isentropic outflow from the tropics, and mean ages can be calculated with reasonable certainty, at least for the "overworld" region above 380 K θ. Below 380 K, in the "middleworld" region where the tropopause slants down toward the poles,

[2] Deployment dates were April 24 - May 13, June 26 - July 10, and September 8 - 21.

isentropes cross the tropopause, and isentropic transport pulls in air not from the tropical stratosphere but from the mid- or high-latitudes upper troposphere. Boundary conditions are generally less well known here than at the tropical tropopause, and can vary with latitude. However, tracer measurements in the middleworld can still provide good age estimates for species that are well-mixed in the troposphere, and generally provide at least a qualitative diagnostic of recently-tropospheric air.

CO is a short-lived tracer of tropospheric origin with $\tau_{CO} \approx 3$ months in the stratosphere, and therefore a strong gradient from tropics to pole. (See Appendix 4.) This makes it ideal for diagnosing young air in the lowermost stratosphere ($350\ \mathrm{K} < \theta < 450$). At 380 K, by the time air in the lowermost stratospheric reaches the latitude of Fairbanks, its CO mixing ratio has typically fallen to nearly half of its tropical value ($\approx$ 25 ppb as opposed to $>$ 40 ppb at the tropical tropopause). Filaments of recent tropical origin, with minimal photochemical losses, are therefore clearly identifiable in CO measurements. CO provides a greater sensitivity to young air at near-tropopause altitudes than any other tracer measured by current or past ER-2 payloads.

CO can provide no information about the age of air at higher altitudes, where mean air age is older and [CO] approaches its photochemical steady-state value. [3] Above 450 K θ the longer-lived N_2O becomes the more useful tracer. With $\tau_{N_2O} \approx 40$ years in the lower stratosphere, [4] a far weaker meridional gradient in the lowermost stratosphere, but by 450K the difference between tropical and Fairbanks background N_2O profiles is 15-25%, sufficient for detection of tropical air. N_2O is also an ideal tracer for diagnosing outflow of photochemically older air from the polar vortex, since vortex mixing ratios of N_2O are severely depressed, showing losses of $>$ 75% from the Fairbanks background.

Simultaneous measurements of CO and N_2O during POLARIS thus allow identification of both tropical and vortex air in the entire range from tropopause to ER-2 cruise altitude (see figure 3.5). Previous studies of filamentation have used other *in-situ* ER-2 data to

[3] $\approx$ 12 ppb from ER-2 measurements

[4] The photochemical lifetime of N_2O is a strong function of altitude, since N_2O is lost predominantly by photodissociation.

validate trajectory calculations (e.g. 74), but without CO validations were not extended below about 420K into the lowermost stratosphere. The POLARIS configuration provides us with an unprecedented view of transport processes throughout the lower stratosphere.

3.2.3 ALIAS instrument

ALIAS is a four-channel tunable diode laser (TDL) scanning absorption spectrometer that measures gas concentrations in the upper troposphere and stratosphere from the ER-2 research aircraft (76). In its POLARIS configuration, simultaneous measurements were obtained of CO, CH_4, N_2O and HCl. CO and N_2O are measured on a single channel, at 2190 cm^{-1} (4.6 μm), with absorption spectra taken at a 10 Hz rate and summed to produce 0.3 Hz reported data. The horizontal resolution of individual data points is then < 200 meters. The pressure-broadening threshold of the target absorption lines is $\approx$ 400 mb; in θ coordinates data is obtained from typically 310 K (7.5 km) to ER-2 cruise altitude at 500-530 K (19-20 km). As the ER-2 climbs to cruise altitude in about 45 minutes (and descends in 30), this yields $\approx$ 700 (500) data points per ascent (descent) profile. Measurement precision is on the order of 0.7 ppb and absolute accuracy 5%, although flight-to-flight measurements compare more closely. ALIAS has flown on numerous ER-2 missions, and ALIAS CO and N_2O data from the 1995-1996 tropical STRAT mission are used here as well for comparison to the high-latitudes mixing ratios observed during POLARIS.

3.2.4 Flight patterns

The POLARIS mission is unique among *in-situ* datasets for its long-term, repeated coverage of the same airspace. To take advantage of that characteristic, the data used in the bulk of this analysis are restricted to a limited region around Fairbanks. The flight patterns flown by the ER-2 during POLARIS ranged from long survey flights to photochemistry flights in which the plane made repeated E-W transects at cruise altitude, to "stack flights" where the plane ascended in a stairstep pattern sampling different θ-

altitudes. Of that data we use ascents and descents out of Fairbanks, or, for flights in which the aircraft made repeated passes over the airfield, data restricted to a limited footprint. Using the full dataset would bias filament detection to ER-2 cruise altitude (500-540 K θ), and would incorporate dives in randomly distributed locations. All Fairbanks takeoffs and landings were made from the same location, the Ft. Wainwright Army base. Since the ER-2 climbs rapidly, the median projection of an ascent or descent is 315 km, of the same order as the typical horizontal extent of fine filaments reported in simulations. In those flights with an atypically slow ascent (5 of 21) we restrict the data to a 500 km radius around Fairbanks.

3.2.5 Meteorology

It should be noted that although climatological conditions were normal during the summer and fall POLARIS deployments, the spring deployment was highly atypical. 1997 saw the latest breakup of the Arctic polar vortex in 42 years of recorded radiosonde observations (75). While mean breakup date is the end of March, in 1997 the vortex did not break up until at least the end of April, and by some criteria the beginning of May. The ER-2 therefore sampled polar conditions that would typically have occurred a month earlier. Observations of vortex air during POLARIS should be interpreted in this light. Temperatures in vortex were also record lows in 1997, although it is not clear whether this would affect transport from the tropics. The winter of 1997-8 was comparatively normal, with the vortex forming again as usual in mid-October 1997.

Mean tropopause height above Fairbanks during POLARIS was $\approx$ 320 K (8.8 km). Tropopause identification was made using data from the Microwave Temperature Profiler instrument on the ER-2 payload in combination with local temperature and pressure measurements made by the ER-2's MMS meteorological system; estimated error in tropopause altitude for individual flights is 100 m.

3.3 Observed filamentation

3.3.1 Overview

During the six months of the POLARIS campaign, the ER-2 saw in the lower stratosphere above Fairbanks repeated incursions of air that was chemically indistinguishable from tropical air. The tropical signature in these incursions was consistent in all measured transport tracers on the ER-2, among them CO, N_2O H_2O, CO_2, CH_4, and CFC-11. Of these CO provided the most sensitive diagnostic of young air in the lowermost stratosphere. Background CO profiles above Fairbanks are depleted in CO by $\approx$ 50% from tropical mixing ratios, as would be expected for air that entered the stratosphere several months previous. In many flights, however, the ER-2 passed through air with CO mixing ratios characteristic of the tropics (or, below 380 K, the low-latitudes upper troposphere). Bulges of high-CO, presumably young air are evident in many of the CO profiles measured by ALIAS during POLARIS, shown in figures 3.2,3.3,and 3.4. Plotted in the same figures for comparison are the seasonal median CO profiles obtained in the deep tropics by the same instrument during the 1996 STRAT campaign. We interpret these features as filaments or streamers of air that have moved isentropically from lower latitudes to 65N rapidly enough to experience no measurable photochemical loss of CO.

3.3.2 Seasonality

The observed filamentation is strongly seasonal, present on more than half the days in the spring and fall deployments, but entirely absent in summer. The difference between the highly variable spring and fall and the near-uniformity of summer profiles is striking. This seasonal pattern is similar to the behavior noted in the long-term trajectory studies of *Waugh 1996* and *Chen et al. 1994*, but while those studies showed only a reduction in filamentation during summer months, the POLARIS data show a virtual cessation of activity. The apparent cessation may be an artifact of the fact that we sample only at 65N. If summer filaments are not only sparser but also slower, they may not reach Fairbanks

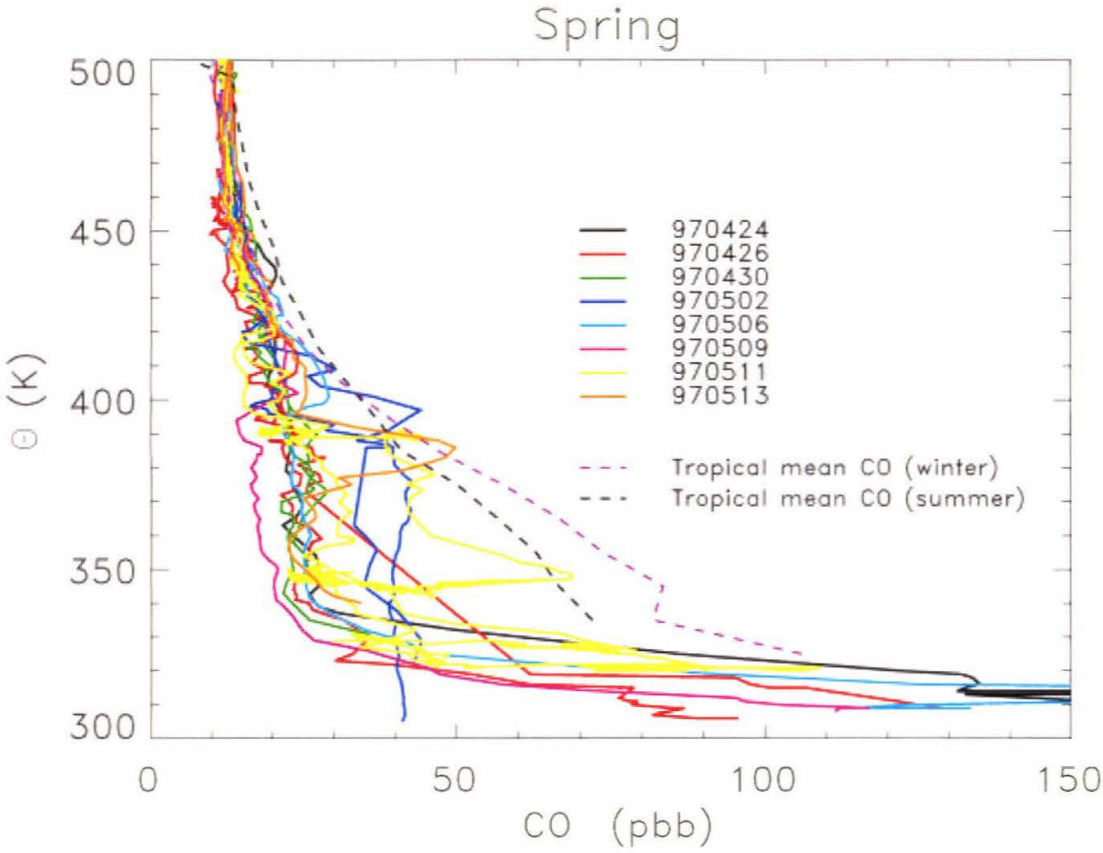

Figure 3.2: CO profiles over Fairbanks obtained during the spring deployment of the POLARIS campaign. The colored lines represent Fairbanks data on individual flight dates between April 24 and May 13, 1997; the dashed lines are tropical mean profiles obtained during the 1996 STRAT campaign. The mean background Fairbanks profile show marked loss of CO over the tropical mixing ratios (to $\approx$ 30 ppb between 350-400 K θ), but many profiles show narrow regions of enhanced CO with no measurable loss. These are interpreted as filaments of "young" air recently arrived from the tropics. The low-CO values on 970509 are real, and reflect mixture of very old air from the decaying polar vortex. The local tropopause sits at $\approx$ 330 K θ (11 km); CO values rise sharply in the troposphere below.

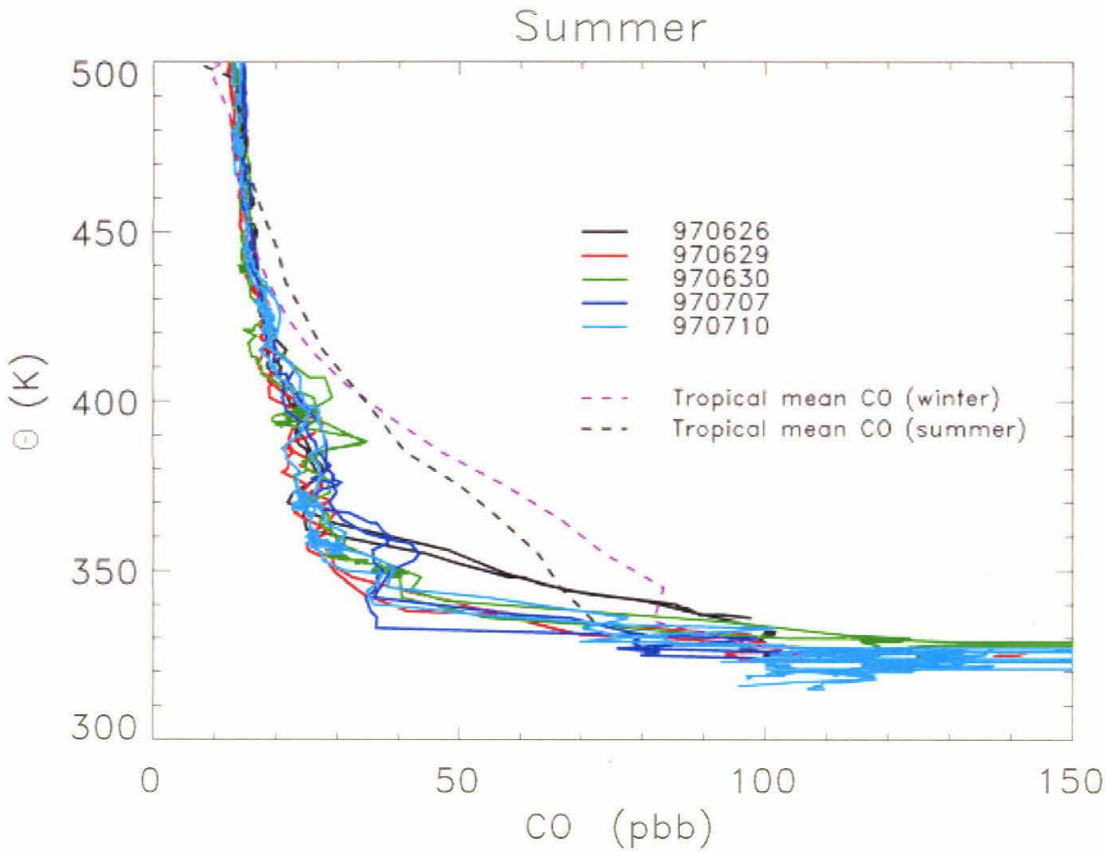

Figure 3.3: Fairbanks summer CO profiles. Filamentary activity in the lower stratosphere is now almost nonexistent. A slight enhancement in CO occurs on 970630, but even that remains below tropical values. The increase in CO over spring profiles below 355 K θ is due to increased mixing of tropospheric air into the middleworld stratosphere; that air may be local in origin. The summer increase in middleworld mixing is a well-established phenomenon (e.g. 56).

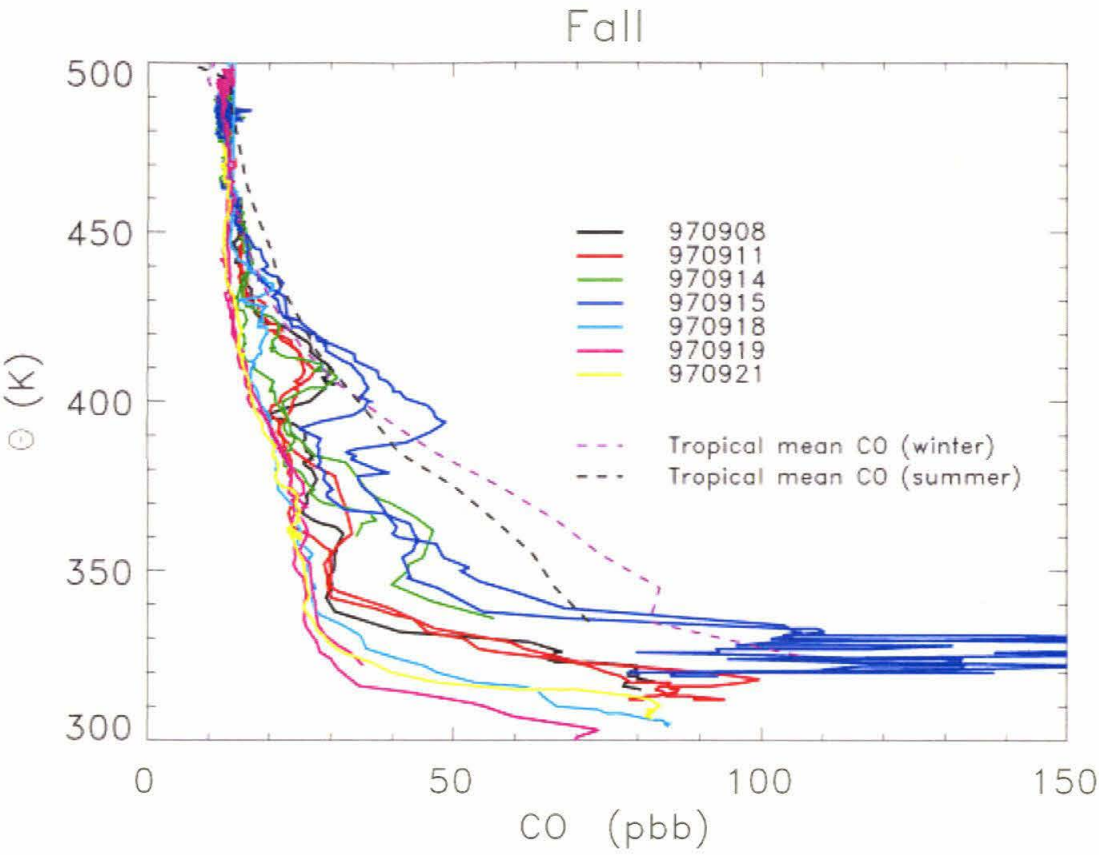

Figure 3.4: Fairbanks fall CO profiles. Filamentary activity around the 380 K θ level is again strong, resembling the spring profiles. The CO enhancement observed between 380-410 K θ on Sept. 14th and 15th represents the same persistent filament; the aircraft trajectory struck the core of the filament only on the 15th. This filament is associated with advection from the overworld all the way down to the local tropopause. On other days, mixing of tropospheric air into the lowest middleworld stratosphere is reduced from its summer peak.

before mixing irreversibly with ambient air. One of the summer flights, 970630, does show some traces of enhanced-CO air, in the 390-410 K region, but the CO mixing ratios are well below tropical. If this enhancement represents the remnants of a tropical filament, then transport times must have been slow enough to allow either dilution by mixing or much greater photochemical losses than in spring or fall.

3.3.3 Vertical extent and distribution

Filamentary activity in these data is also a strong function of altitude. We find that filaments of young air are strongly concentrated around 380-420 K, at and just above the level of the tropical tropopause, and often are seen only in this restricted altitude region. Since wind shear often produces slanting filaments, the one-dimensional slice through an individual filament that the ER-2 provides can be misleading, and the filament may actually be deeper than the 20-30 K θ range transected by the ER-2. Nevertheless, it is possible to draw inferences about altitude distribution of filaments from the complete sample of POLARIS observations. The full dataset make it clear that tropical filamentation in the lowermost stratosphere is "capped" sharply at the 420 K level. Whenever deeper filaments are observed, they extend downwards from the 380-420 K region all the way to the local tropopause, and possibly below it (e.g. 970511 in figure 3.2), but never upwards into the overworld.

Day-by-day comparisons with N_2O mixing ratios, which provide better age discrimination at higher altitudes, show that the apparent cap is not simply an artifact of the falloff in CO with altitude. Figure 3.5 shows N_2O and CO on a representative ascent and descent during the spring deployment (970513), referenced to the median Fairbanks profiles and compared with median tropical profiles. This type of figure clearly shows that the combination of N_2O and CO measurements provides sensitivity to young air throughout the entire ER-2 altitude range. On this day, tropical-valued air is clearly apparent in both CO and N_2O at 380 K θ, though the enhancement over background is a factor of 2 for CO and only 10% for N_2O. The N_2O measurements show no trace of young air

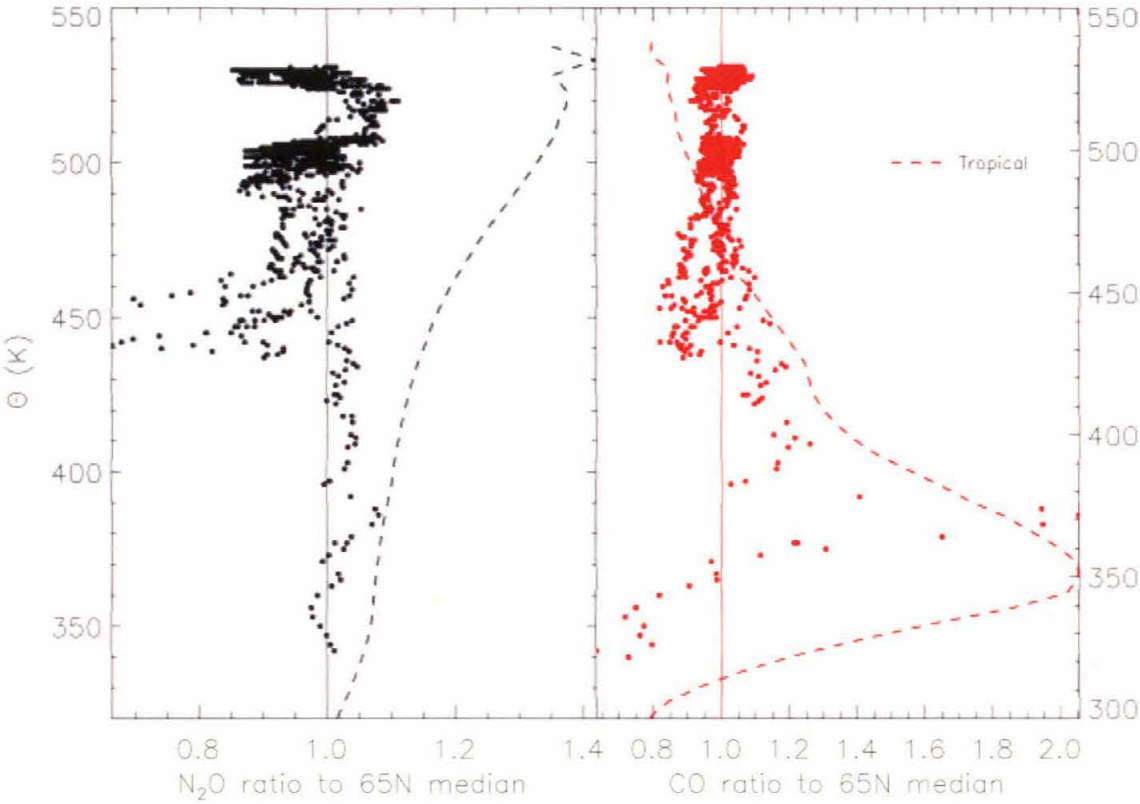

Figure 3.5: CO and N_2O over Fairbanks on 970513. The dots are flight data, referenced to the Fairbanks median spring profile. The dashed line represents the median tropical profile, from STRAT data, again referenced to the median Fairbanks profiles. The dashed line thus maps out the altitudes where each tracer can discriminate between tropical and mean Fairbanks air. CO is most sensitive as an indicator of young air at 350 K and is useful up to $\approx$ 420 K; N_2O is insensitive in the lowermost stratosphere but becomes a useful indicator above 420 K. Note here the incursion of tropical-valued air at 380 K, apparent in both CO and N_2O and the filament of old (vortex shed) air apparent only in N_2O at 450 K. Because the median CO profile over Fairbanks is close to photochemical steady state, CO is a poor indicator of old air.

at higher altitudes. Inspection all other flight data over Fairbanks shows that this is a universal feature. The dataset contains no observations of young air above 420 K.

3.3.4 Vortex filaments

Although the focus of this study is the tropical filaments which carry some or all of the meridional circulation in the lower stratosphere, the late breakup of the Arctic vortex in 1997 allowed us to also observe filaments shedding off the polar vortex throughout the spring and even summer deployments. The N_2O in figure 3.5, which shows no CO-enhanced young air above 420 K, does show a layer of CO-*depleted* air at 450 K; the same feature is visible weakly in CO. Similar intrusions of tracer-depleted, chemically "old" air were visible on many days during the spring and summer deployments and almost certainly represent remnants of the polar vortex. Unlike tropical filaments, the vortex remnants were distributed throughout the lower stratosphere, and were in fact more predominant near ER-2 cruise altitude than in the lowermost stratosphere. A deep slab of CO-depleted vortex air was apparent in the lowermost stratosphere on 970509, from 330-400 K, and a shallower intrusion at 400-420 K on the 970511 stack flight, just above a tropical filament (figure 3.2). On 970430, vortex air with N_2O depleted to < 190 ppb was evident at 500 K. Surprisingly, the ER-2 continued to encounter persistent vortex remnants over Fairbanks throughout the summer. All the vortex filaments observed in summer lay close to ER-2 cruise altitude, at 500-540 K, so it was not possible to determine their vertical extent. N_2O mixing ratios in these filaments reached as low as < 50 ppb, indicating undiluted air from the vortex core that had yet to mix with its surroundings more than two months after vortex breakup.

3.3.5 Higher-latitude data

The subset of ER-2 data discussed above was confined to the airspace above Fairbanks so that no sampling bias would be introduced. For the purpose of examining the robustness of the 420 K cap observed on tropical filaments, however, we expand the dataset in

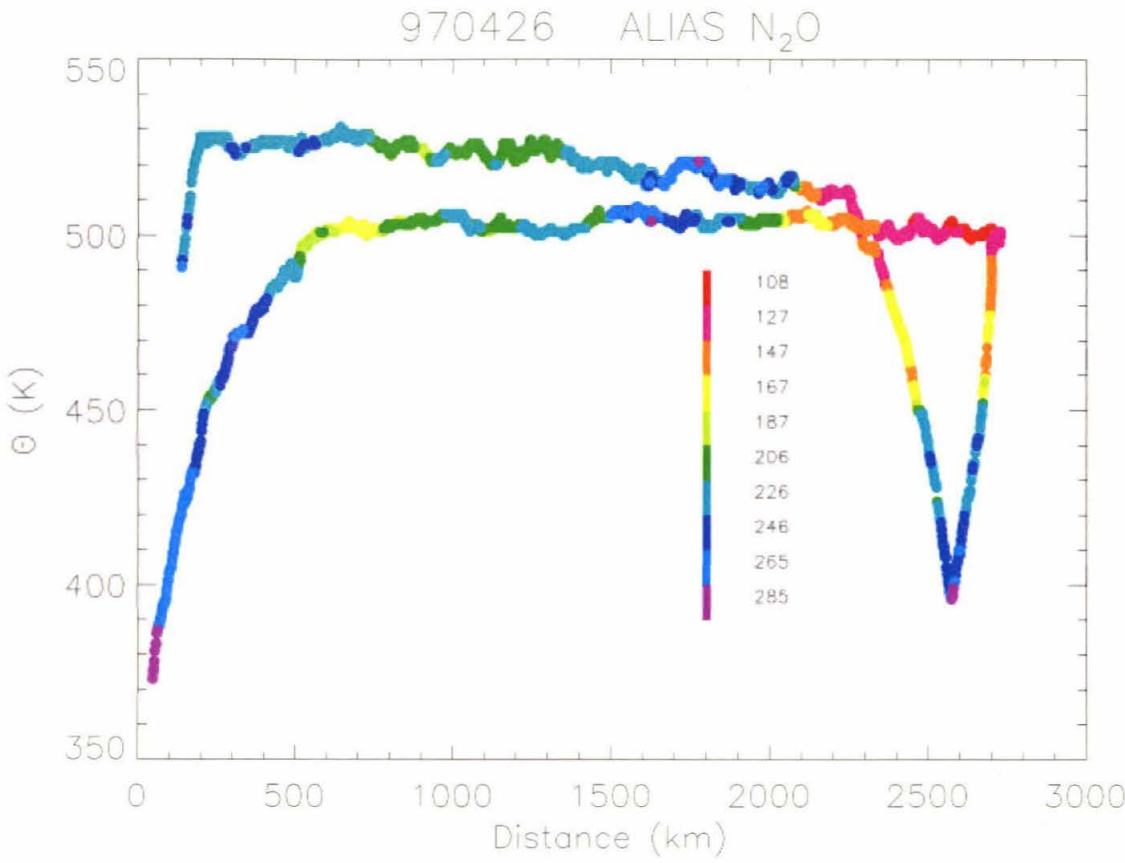

Figure 3.6: N_2O on the polar flight of 970426. The aircraft dive was made at the pole itself. On the approach to the pole, between 1500-2000 km from the airfield, the ER-2 passed through a region of air with enhanced N_2O mixing ratios; N_2O in part of this region reached tropical values. This young air lay well within the still-existant polar vortex.

this section to include all Arctic latitudes (> 50N). This expansion adds data almost exclusively in the 500-540 K region where the ER-2 cruises. In all 21 high-latitudes POLARIS flights we find only one example of young air at altitudes higher than 420 K, and that example comes from a flight to the north pole on 970426, just before vortex breakup. Well inside the polar vortex, at 79-82 N latitude, the ER-2 passed through a 150 km stretch of air with near-tropical N_2O values (figure 3.6), and passed through it again on the return from the pole. The filament appears to be an intrusion into the vortex drawn polewards during the process of vortex breakup, much as described by *Plumb et al. 1994*

in their study of the 1992 Arctic vortex. The lone example of a higher-altitude tropical filament during POLARIS then appears to be driven by very different processes than the recurring low-altitude filamentation that is capped at 420 K. The dominant type of filamentation in the POLARIS dataset is this low-altitude tropical transport, and for the remainder of this chapter, the term "filaments" will be used to refer to this phenomenon alone.

3.3.6 Filament and background profile ages

If the initial mixing ratio of CO entering the stratosphere across the 380 K θ surface (the height of the tropical tropopause) is known, CO can be used as a photochemical clock to determine the age of air in the observed filaments. However, although CO is the most sensitive marker for young air in the lowermost stratosphere, uncertainties in this initial mixing ratio make it not ideal for providing a quantitative age estimate. The inhomogeneity of CO in the upper troposphere and the limited set of *in-situ* tropical measurements introduces uncertainty in the inferred age. We use estimated initial values for CO here to place a range on filament ages. The lower limit for filament age is clearly 0 days, since filament mixing ratios of CO and N_2O are in some cases greater than values measured in the tropics at corresponding θ levels. We derive an approximate upper limit for the transport time from tropics to Fairbanks latitudes from using estimated CO initial mixing ratios of 50 ± 5 ppb. We model photochemical loss and production of CO during its transport polewards (See Appendix 4 for details) using measured OH and modeled Cl and O^1D from the STRAT and POLARIS ER-2 campaigns over the full equator-pole latitude range to obtain an upper limit of $\approx$ one week on the age of the strongest observed filaments.

These ages are verified by using measured mixing ratios of CO2, which provide a more quantitative age for air that is identifiably recent in origin (again, see Appendix 4). The mixing ratios of simultaneously measured water vapor also confirm the young age of air in filaments. This combination of ER-2 tracers provides a consistent view of an age for

POLARIS filaments on the order of days.

Air ages derived from the background CO profiles, which show significant photochemical loss, yield a value for mean age of approximately three months. This age does not vary seasonally: slight shifts between deployments in CO mixing ratios at 475 K and above are due to seasonal changes in the value of photochemical steady state, not to transport processes. The background CO profiles from 380 to 475 K are remarkably constant in all seasons.

3.4 Back-trajectory calculations

3.4.1 RDF calculations

To relate the small slice of air the ER-2 observes above Fairbanks to a wider picture of atmospheric motions, trajectory simulations were run for each flight day. All simulations use the remote domain filling (RDF) technique described in section 3.1.2. A grid of points is established and then advected backwards over a 10-day period according to the prevailing winds in an assimilated dataset, establishing the previous position of that air parcel. The value of that 10-day-previous potential vorticity (PV) is then plotted on the original grid. PV is used rather than latitude because it better discriminates between air on either side of the subtropical mixing barrier; the apparent barrier can be irregular with latitude. The resulting plots show atmospheric structure at a resolution far below the gridscale of the original data. All simulations were carried out by Paul Newman of the Goddard Space Flight Center. For each flight day, trajectory calculations were run at four θ levels throughout the lower stratosphere - 350, 400, 450, and 500 K - over a large portion of the northern hemisphere. Curtain plots were also generated for a few specific flight days, covering only the area of the flight path but with a much finer grid of θ levels. The GSFC/Data Assimilation Office (DAO) winds were used for the four-level plots, and the NCEP/NCAR reanalyses for the curtain plots. All simulations were run by an automated script with no possibility of adjustment to or bias from the observed

CO patterns.

3.4.2 Comparison with observations

The POLARIS dataset provides a unique opportunity for validating trajectory simulations. Although *Waugh 1996* noted that the positions of simulated filaments differ strongly according to which set of assimilated winds was used in the calculations, they had no observational data with which to compare their simulation results. Here we find that both the DAO and NMC winds reproduce the observed filamentation events remarkably well, not only replicating the general trends but capturing details seen on individual flights. The simulations support the inference from ER-2 data that filamentation in the lowermost stratosphere is capped at 420 K, but also suggest that some of the observed filaments are deeper than is apparent in the ER-2 transects, reaching down through the middleworld to the local tropopause.

Seasonality in simulations

The RDF results show the same seasonal trend as the observed filaments, with activity strong in the spring and fall deployments and absent in summer. Figures 3.7,3.8, and 3.9 show individual days from spring, summer, and fall deployments (970511, 970630, and 970915), with the flight track superimposed. These are not completely representative; the spring and fall days shown are those with the strongest filamentation evident in the CO data. Those features are well-reproduced in these simulations. Both spring and fall show noticeable gradients in PV at the lowest θ levels, and individual filaments of low-latitudes air moving through them in the 10-day timescale of the calculations. Although the PV gradients at 350 and 400 K θ on 970511 likely reflect the residue of the polar vortex, which broke up several weeks previously, on 970915 the vortex was still a month away from forming. The increasing PV gradients in September instead reflect the tropospheric subtropical jet, which shifts north and strengthens in the fall (figure 3.10). The summer simulation, by contrast, is nearly featureless at all levels. If filamentation is occurring at all

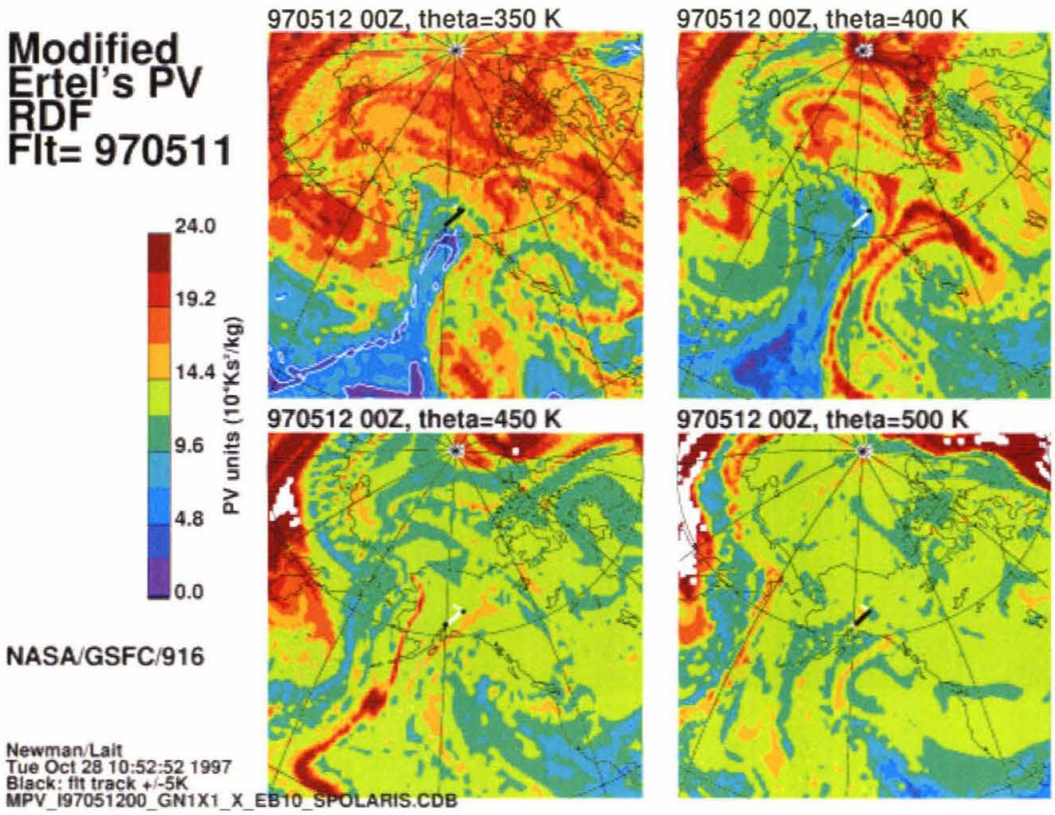

Figure 3.7: Remote domain-filling trajectory calculations for 970511, when the ER-2 made repeated passes through a well-defined filament of young air. The four panels show calculations at four θ-levels; filamentary activity appears in the 350 and 400 K levels but is absent at higher altitudes. The blue fields represent young air and the red fields the remnants of the decaying polar vortex; note that the two are correlated, especially on the 400 K surface. The ER-2 flight track is shown in white and black, with the black segment representing that part of the flight path that intersects the corresponding θ level. On the 400 K level, the flight path crosses from young air into much older vortex air. This feature is well reproduced in the flight data.

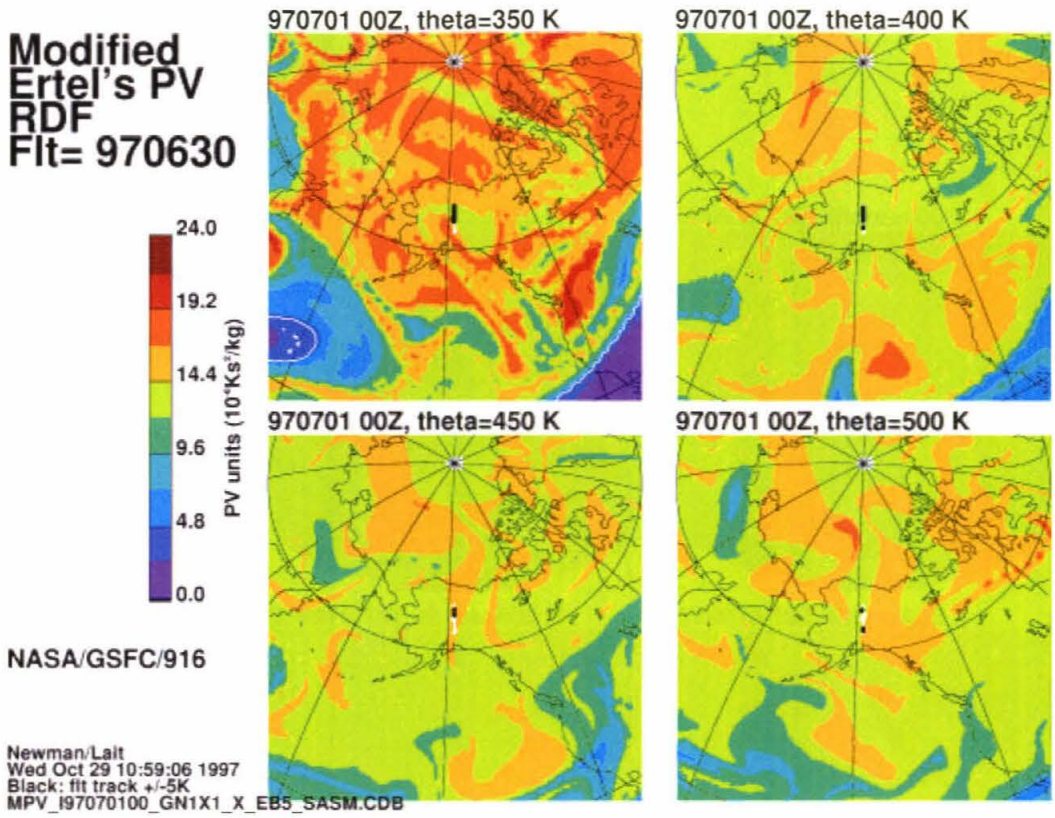

Figure 3.8: RDF calculations on 970630, when the ER-2 made its second POLARIS stack flight. The absence of filamentary activity and of strong PV gradients is characterisitic of all the summer flights.

in summer, it is slow enough that it cannot be captured by a 10-day back trajectory. Note that this does not imply that filaments must have mixed with surrounding air, but simply that the simulation itself cannot reproduce motions that take place on longer timescales. No summer simulation reproduced the vortex filaments observed at 500 K, for example, because those features had formed more than ten days previously. The featurelessness of the summer simulations does imply, though, that the lack of observations of tropical air over Fairbanks was not simply the result of filament motions stopping at lower latitudes. If filamentation is occurring in the lower stratosphere in summer, it must be significantly slower than in other seasons.

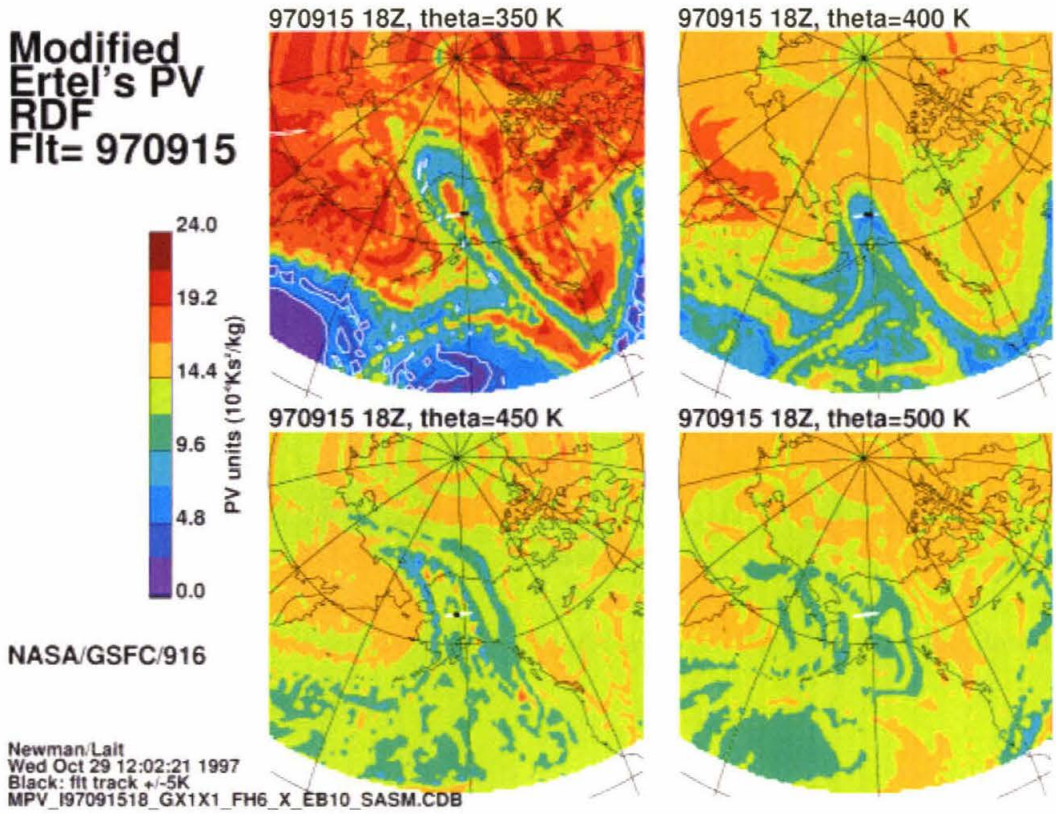

Figure 3.9: RDF calculations on 970915, when the ER-2 flew through the core of a well-defined filament of young air. The formation of strong PV gradients on the lower θ levels is associated with the poleward movement of the tropospheric subtropical jet and is seen throughout the fall deployment. The polar vortex has not yet formed at this time, and there is no increase in PV gradient at higher θ levels. Note the slanting front of the filament, which extends further poleward at 350 K than at 400 K.

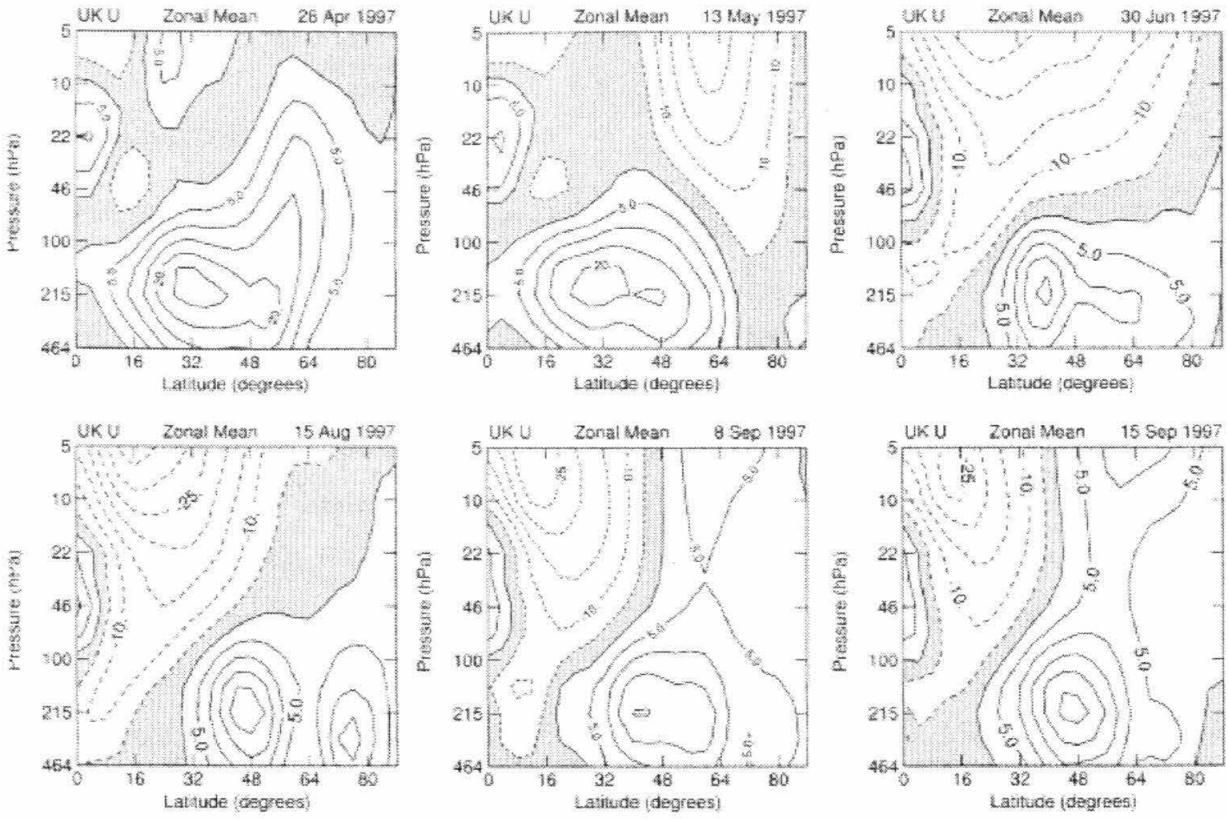

Figure 3.10: Zonal winds from spring-fall. Winds are from the UKMO assimilated dataset (*courtesy of Gloria Manney*).

Vertical extent

The trajectory simulations confirm the 420 K cap to tropical filamentation in the lower stratosphere. In figure 3.9, for example, the structure apparent at 350 and 400 K is absent by 450 K. This figure also illustrates the underestimation of filament depth that flight tracks can produce. In the ER-2 data, this filament appeared as a narrow layer between 385 and 420 K, with CO values decreasing sharply below 385 K (figure 3.4). The RDF plots show a a deep poleward-slanting filament extending down to at least 350 K, with the ER-2 flight path intersecting only a narrow region of it. (The flight track is shown in white, with that part which intersects each θ level highlighted in black). The 420 K cap holds for all simulated flight days, in agreement with the ER-2 CO and N_2O observations: no simulation produces tropical filaments on the 450 or 500 K levels except for the 970426

vortex intrusion, even in those areas not sampled by the ER-2.

Stack flight correspondence

The spring stack flight on 970511 provided the best opportunity for testing the positional accuracy of the trajectory simulations. The aircraft flew six different constant altitude legs from the tropopause to ER-2 cruise altitude, covering a wider range of airspace above Fairbanks than on a simple ascent and descent. 970511 represented the only stack flight made from Fairbanks during the active spring or fall period; the one summer stack flight obviously crosses no features that could be correlated with the simulations. During the 970511 flight, however, the aircraft repeatedly crossed back and forth between a filament of tracer-enhanced tropical air on one end of the stacks and a region of tracer-depleted air at the other. The resulting spread in CO values on each stack is apparent in figure 3.11. Figure 3.12 shows the same CO data in 2-dimensional space. Midway through the 350 K flight leg the aircraft passed into a region of young, high-CO air, continued in it up to 390 K, and then passed out of it midway through the 390 K leg. Those features are reproduced in the simulation of figure 3.13. Simulation and data also agree in the patch of CO-depleted old air traversed on the ascent to the 430 K leg.

The positional accuracy of the filament in the simulation can in fact be determined directly by the flight track alone in figure 3.13, without reference to the CO data. Because the aircraft flew at constant pressure-levels, but temperatures within the filament were four degrees colder than the surrounding air, each crossing of the filament boundary appears as a sharp drop in θ. Comparison of those jumps with the simulation contours suggests that the simulation mispositions the filament edges by about a hundred kilometers on both the 350 and 390 K legs. The simulation is less accurate at lower θ levels, showing the filament extending no further than 345 K while the data clearly show that the aircraft flew in tropical air for much of the lowest two stacks as well, down to 320 K. Although the color scale of figure 3.12 resolves the lower stacks poorly, the spread in CO on these levels is apparent in figure 3.2. (These two stacks are not shown in figure 3.13.) In general, however, the correspondence between simulation and data is surprisingly good,

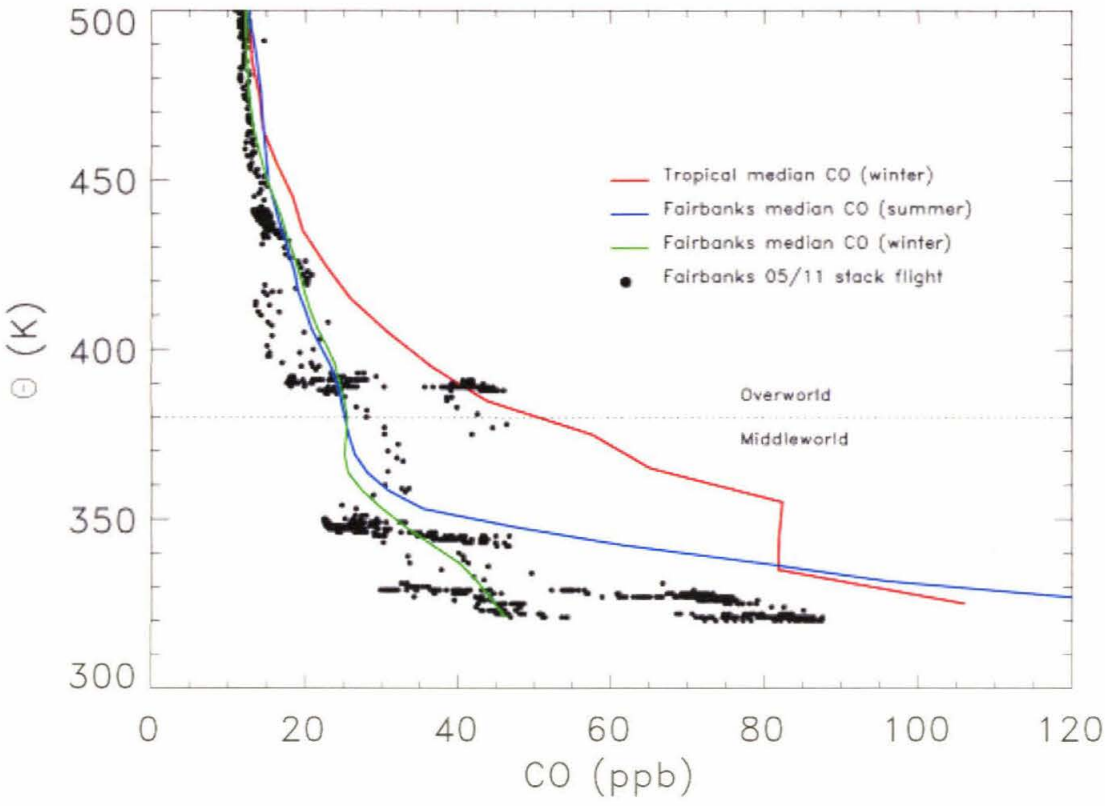

Figure 3.11: 970511 stack flight CO compared to tropical and Fairbanks median profiles. The clusters of points at the 325, 350, 390, 440, and 490 K θ levels represent the legs of the stack flight. On the 325, 350, and 390 K legs the aircraft sampled a large range of CO mixing ratios, from below the median Fairbanks profile to at or above the tropical value. We interpret this data to mean that the flight legs crossed the edge of a filament of young air, and sampled also vortex air that was pulled alongside the filament, as often happens in filamentation events. Figure 3.12 confirms this interpretation.

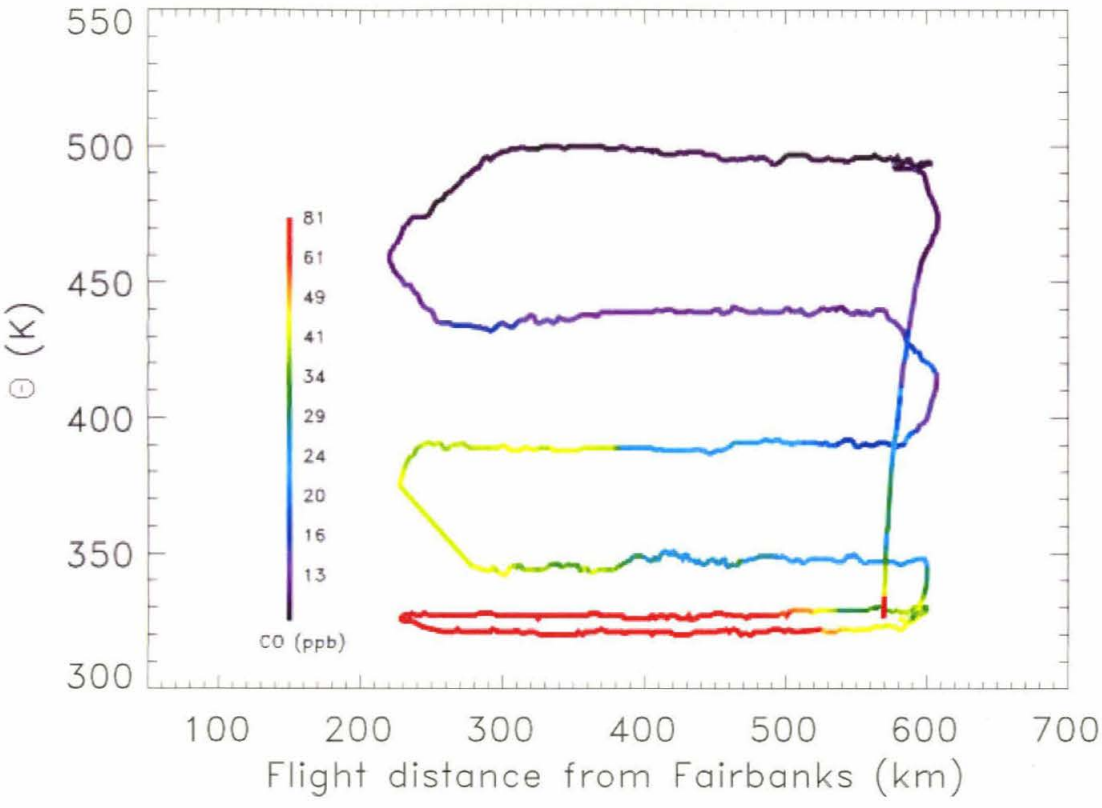

Figure 3.12: CO on the 970511 stack flight CO, in a 2D view. The 325, 350, and 390 K legs show a consistent gradient in CO, with high values over Fairbanks and sub-normal values at the end of the flight track. The anomalous values on each leg are clearly correlated.

especially given that *Waugh 1996* reported that the positions of filaments derived from different datasets of inferred winds can differ by many hundreds of kilometers.

3.5 Discussion

The POLARIS campaign provided the first opportunity to look systematically at rapid transport events in the lowermost stratosphere. Both observations and trajectory simulations presented here suggest that the lowermost stratosphere is a region of intense filamentary activity, with individual filaments extending from 420 K down to near-tropopause

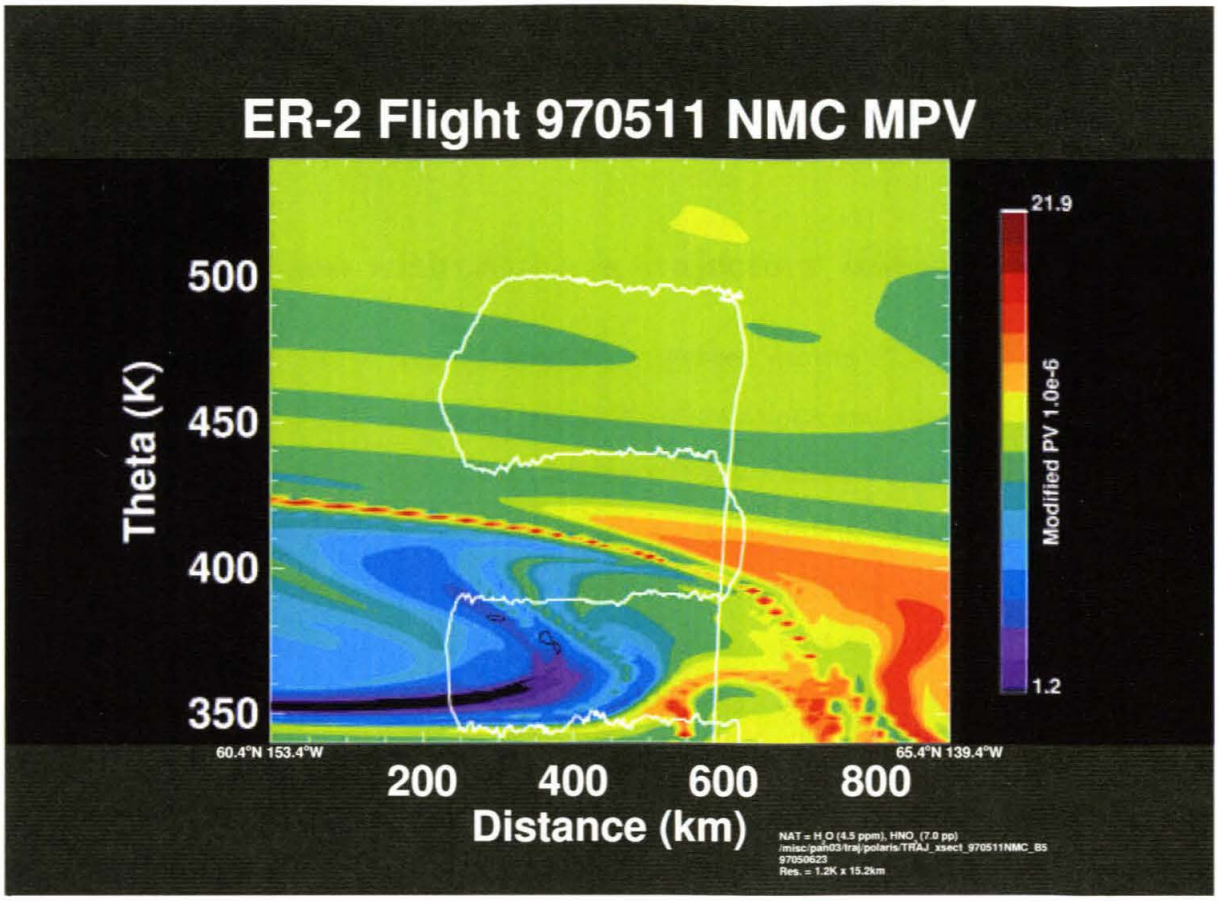

Figure 3.13: RDF calculations of the stack flight of 970511. The flight track is shown in white; the 10-day-previous PV in color. The color scale is inverted from that of figure 3.12: blue now represents low PV, or tropical air, and red represents high-PV, polar air. The simulation here corresponds almost exactly to the *in-situ* data, with the lowest three flight legs passing between young air close to Fairbanks and old air at the end of the stack legs. The actual filament edge can be seen clearly in the flight track itself. The ER-2 flew each stack at a constant pressure level; any abrupt change in temperature thus produces a sharp change in θ. The filament temperature was measured at 4° cooler than the surrounding air. With the flight track plotted in θ coordinates the filament edges are readily apparent at $\approx$ 470 km from Fairbanks. Comparison with the edges of the simulated filament shows that the RDF calculations place the filament within 50 km of its observed location.

levels but activity ceasing sharply above 420 K. The POLARIS dataset also represents the first long-term set of *in-situ* observations that can be use to validate the results of long-term trajectory studies.

3.5.1 Comparison with previous trajectory simulations

The altitude distribution of tropical filaments observed during POLARIS is very different from that of previously published trajectory simulations and tracer observations. In part this is because neither studies nor observations have tended to address the very lowermost stratosphere, where we see filamentation concentrated. Tracers other than CO are relatively insensitive to transport at these altitudes, and the upper altitude limit of POLARIS lower stratospheric filaments corresponds to the lowest levels that trajectory studies have considered. However, there is sufficient overlap between the POLARIS tracer dataset and published simulations to note some discrepancies. In particular, we observed no activity whatsoever in the 400-500 K region where both simulations and observations have reported considerable filamentation (e.g. 73, 12, 49), except in the context of vortex breakup.

It is possible that this discrepancy is due in part to the location and timing of POLARIS observations. Most reported *in-situ* observations of tropical filaments at latitudes as high as Fairbanks have been made in mid-winter, when the vortex is strong, the one season we do not sample (74, 49, 3). Transport in general should be more vigorous in winter, and it is possible that filaments in the 400-500 K region are fast enough to reach high latitudes only in winter, and in summer tend to stop or mix with surrounding air before reaching 65 N. (Although it is certainly not the case that diffusive mixing is enhanced at those altitudes, since we see undiluted polar vortex air persisting until July.) It is possible that filamentation in the 400-500 K region is strongly enhanced by vortex activity, much as suggested by *Waugh et al. 1994*, and can be observed at latitudes as far polewards as Fairbanks only when the vortex is present. Filamentation in the lowermost stratosphere observed during POLARIS, by contrast, seems to have little correlation with

vortex strength, appearing as vigorous or more so in September as in April when the vortex is present. These data then suggest that the lowermost stratosphere is at least a region of faster tropical filamentation, and at most represents a separate and distinct transport regime from the remainder of the lower stratosphere.

3.5.2 Dynamical forcing

The POLARIS observations of filamentation agree in a general sense with the seasonal pattern reported by the CA studies, with filamentation strong in fall and spring and sharply reduced in summer (73, 12), but our observed period of strong filamentation is slightly longer than that of the trajectory studies. While *Waugh 1996* report the onset of strong filamentation in late September, we see well-established tropical filamentation already on the first flight of the fall deployment, on September 8. This difference is significant for determining the driving forces of transport in the lowermost stratosphere. Most previous filamentation studies have invoked Rossby wave breaking in the middle stratosphere as the driver of tropical filamentation, and have tied filament seasonality to the annual reversal in the direction of the stratospheric zonal wind. These data suggest that filamentation in the lowermost stratosphere may be driven by processes at tropospheric altitudes instead, such as the strengthening and poleward shift of the tropospheric subtropical jet. Figure 3.10 shows the mean zonal wind in the upper troposphere and stratosphere from May through September. At 530 K (50 hPa), the dominant change from summer to fall is in fact the zonal wind turnaround, and the turnaround at midlatitudes does not occur until late September. At 420 K (110 hPa), winds are westerly in all seasons, and the dominant change between summer and fall is the shift in the tropospheric jet, which is occurring already in early September, and produces the sharp PV gradients apparent in figure 3.9. In this view the lowermost stratosphere represents a transition region, part of the stratosphere but driven by local tropospheric processes. [5]

These data also demonstrate that the boundary of that transition region is not the

[5] Although Rossby waves originate in the troposphere, we term Rossby wave breaking in the middle stratosphere to be a "stratospheric process".

classical 380 K boundary between the overworld and middleworld. The middleworld is generally understood to be a dynamically active region, experiencing episodes of strong mixing with tropospheric air. Measurements of tracers such as water vapor produce the appearance of a sharp boundary at 380 K, with variability confined to the middleworld beneath. The CO data presented here demonstrate that this distinction is an artifact of tracer distributions, and not a reflection of a meaningful dynamical boundary. For tracers such as water vapor, with a strong gradient between troposphere and stratosphere but a minimal one between tropics and pole in the stratosphere proper, any tropospheric air drawn into the middleworld produces a strong signature, but tropical air drawn polewards above 380 K is barely noticeable. With CO, the gradients are of roughly equal magnitude, and activity can clearly be seen to extend into the overworld, with the real dynamical boundary at 420 K. The region between 380 and 420 K is chemically purely stratospheric, but moves in concert with the middleworld, and may respond to forcing from the upper troposphere.

Chapter 4

Filament age estimates from CO, CO_2, and H_2O

4.1 Introduction

Carbon monoxide is a short-lived gas with largely tropospheric sources. It is produced both by incomplete combustion (either industrial or biomass burning) and by the oxidation of methane and other hydrocarbons. Its primary sink is reaction with OH, and the majority of tropospheric CO production is destroyed before it can reach the stratosphere. Since CO sources are concentrated at surface level, tropospheric CO mixing ratios decline with altitude. Upper tropospheric observations show that that decline is more than a factor of 2, to approximately 50 ppb near the tropopause, from which point CO is injected into the stratosphere. Because this upper tropospheric mixing ratio is still well above the stratospheric photochemical steady state, the stratosphere acts as a net sink for CO, with loss by reaction with stratospheric OH outweighing local production by methane oxidation. The mixing ratio of CO in stratospheric air thus declines with the "age" of that air (its residence time in the stratosphere).

The lifetime of CO in lowermost stratosphere is of the order of 90 days during summer, rising slightly in the winter (and becoming essentially infinite in those regions experiencing

permanent darkness). This section presents a simple chemical model that uses that decline as a "photochemical clock" to provide an estimate of the age of relatively young air parcels in the lowermost stratosphere. Similar calculations have been performed by Herman et al. (1999) and Weinstock et al. (2000), among others. High concentrations of CO in the filaments observed over Alaska during the POLARIS clearly imply air that is photochemically extremely young. Admixture of CO-rich tropospheric air into filaments is ruled out as an explanation by simultaneous measurements of water vapor; filaments above the traditional middleworld/overworld boundary at 380 K show purely stratospheric water vapor mixing ratios. Since CO mixing ratios observed in the cores of some filaments are actually greater than the initial conditions we infer from tropical measurements, we can state immediately that meridional transport from tropics to high latitudes by the observed filaments has a minimum timescale of zero days. The photochemical model allows us to determine the sensitivity of that estimate, and to set a reasonable upper bound for the timescale. Photochemical age estimates are confirmed by comparison with simultaneous observations of CO_2, whose seasonal variation provides an independent measure of air age and transport times.

4.2 Chemical loss model

We use a simple 1-D photochemical model incorporating the dominant sources and sinks for stratospheric CO to convert measured CO concentrations in the cores of the filaments to photochemical ages. Air parcels are assumed to move isentropically from the tropics, with their initial CO values those of the median tropical value for the appropriate θ-level. CO production and loss are then calculated in discrete time steps as the parcel is advected polewards. Reactant concentrations are assumed based on existing aircraft datasets and pseudo-steady-state model simulations.

4.2.1 Stratospheric CO reactions

The overwhelmingly dominant sink for carbon monoxide in the stratosphere is reaction with OH. Production of CO occurs via the destruction of CH_4 by any of OH, Cl, or O(1D), with OH the primary reactant in the lower stratosphere. The photochemical loss model here uses these reactions, with reaction rates taken from the JPL 1997 compilation (15).

4.2.2 Reactant concentrations

Concentrations of the radical species comprising the CO source and sinks (OH, Cl, and O(1D)) were simulated using *in-situ* measurements from a variety of instruments flown on the ER-2 during the STRAT (1995-6) and POLARIS (1997) aircraft campaigns, and using photochemical model results based on tracer values measured from the ER-2. OH was measured by the Harvard HO_x instrument, by UV laser-induced fluorescence (78). Calculated concentrations of diurnal average Cl and O(1D) were obtained from photochemical steady state model simulations constrained by *in-situ* measurements of O_3, Cl_y, NO_y, H_2O, CH_4, aerosol surface area and other tracers that were provided by the JPL theory team (R. J. Salawitch, PI) (as described in Flocke et al. 1999). Reactant concentrations were then fit to surfaces as a function of θ and solar zenith angle (SZA). (There is little latitudinal difference that is not a simple function of SZA). For O(1D) and Cl, concentrations at the altitude range of the filaments seen during POLARIS are so small that their contribution to CO production is negligible. For use in the model, [OH] values were converted to diurnal average OH as a function of θ, latitude, and calendar day. Pressure and temperature as a function of latitude along the θ-surface are derived from ER-2 data; seasonal variations in those quantities are not significant to model results.

Unlike the radicals, methane in the young filaments cannot be simulated by mean background concentrations. The relatively long lifetime of methane means that the the young filaments are atypical of their environment, and their methane mixing ratios should remain unchanged from tropical entering values. Actual methane concentrations observed in filaments over Fairbanks are in fact essentially identical to those observed in the tropics

during STRAT, at $\approx$ 1.7 ppm in the filament cores. (Methane values in both POLARIS filaments and STRAT tropical flights are taken from the ACATS gas chromatograph instrument (19).) The model here uses a constant value of 1.7 ppm for methane mixing ratio throughout the filaments' evolution. Slight seasonal variations in methane concentration or in pressure and temperature are insignificant to model results; seasonal variation in CO photochemical loss is produced entirely by seasonal variation in OH concentrations produced by variation in insolation.

4.3 CO tropical boundary condition

The boundary condition for CO entering the stratosphere in the tropics is somewhat uncertain, both because of inhomogeneity in upper tropospheric CO and because the seasonal variation in upper tropospheric/lower stratospheric CO is not well constrained. The six ER-2 tropical flights on which CO was measured cover only a restricted region and capture only part of the expected seasonal cycle, missing the late spring when entering CO might be expected to peak. We use here a value of 50 $\pm$ 5 ppb for the initial CO in individual filaments, which represents a reasonable probability range for CO entering the stratosphere.

4.3.1 Uncertainties due to spatial variation

Because CO is a byproduct of biomass burning, CO concentrations in the uppermost tropical troposphere are expected to be both time-variable and spatially inhomogeneous (Jacob, D. and Logan, J., *pers. comm.*). It is not possible to define a single boundary condition for CO entering the stratosphere. 3-D model simulations (Jacob, D. and Logan, J., *pers. comm.*) suggest that in months when biomass burning is significant, parts of the tropical lower stratosphere may have CO enhanced by a factor of 2. The areas of strong enhancement are relatively small, with the modeled standard deviation of tropical upper tropospheric CO in any given month typically $\sigma < 3$ppb ($\approx 6\%$). Existing *in-situ* aircraft data are not useful for validating model CO distributions, as all ER-2 flights

into the tropics during the STRAT and POLARIS campaigns cover only a narrow swath of longitude. All data were taken on direct southern flights out of Hawaii with dives at tropical latitudes; the total longitudinal range covered by the profiles is restricted to ± 5 degrees. The annual mean mixing ratio for CO entering the stratosphere, [1] measured on these flights is 50 ppb, with a reproducible annual variation of at least 5 ppb. Measurements were made by the ALIAS instrument, the same instrument whose CO data is used in the remainder of this work. These measurements may not be representative of the boundary condition for the filaments observed over Alaska, however. Filaments drawn from locations other than the clean Pacific might have larger initial CO mixing ratios. Both CO and N_2O mixing ratios observed in the POLARIS filaments in fact often exceed the maximum values observed by ER-2 flights at the same θ level in the tropics.

4.3.2 Uncertainties due to seasonal cycle

In addition to uncertainties due to longitudinal variation, the seasonal variation of the CO boundary condition is only weakly constrained. The timing of the tropical observations means that the seasonal cycle of the CO boundary condition even in the Pacific region sampled by the ER-2 cannot be fully determined.

As with other biogenic gases (N_2O, CO_2), carbon monoxide measured at surface stations shows a clear seasonal cycle, stronger in the northern hemisphere, and with opposite phase in the N. and S. hemispheres (e.g. 79). The mixing ratios of N_2O and CO_2 entering the stratosphere reflect the seasonality measured at the surface; stratospheric CO would be expected to follow the same fundamental pattern as well. Stratospheric CO_2 measured from the ER-2 shows a seasonal cycle that is consistent with the integrated CO_2 mixing ratio over the entire tropics, although with a two-month lag (8, 4). (Because the N. hemisphere seasonal cycle is stronger, the integrated tropical mixing ratio has a signal with

[1] "Entering the stratosphere" is defined as crossing the 380 K θ-surface. To account for the varying height of the tropical tropopause and effects of in-mixing of midlatitudes air, the entering CO value was determined by taking mixing ratios of CO at the local tropopause for all tropical flights (with tropics defined as ±15° latitude) and regressing these against θ to determine a value for 380 K θ.

the phase of the N. hemisphere cycle.) Applying the same principles to CO would yield a stratospheric boundary condition with a seasonal variation similar in amplitude to that seen at the ground in the tropics, $\approx 20\%$, and lagged in phase by two months. The case of CO is more complicated than that of CO_2 because CO has more spatially variable sources and sinks, as well as *in-situ* production in the troposphere. The spatial variability in CO sources means that the surface sampling network may not be sufficient to characterize air entering the stratosphere. Extrapolating from surface measurements to stratospheric values may also be problematic if seasonal variations in tropospheric dynamics produce differing CO losses for air reaching the stratosphere. In the absence of complications, however, the seasonal peak in CO mixing ratios would fall in May-June, at the same time when filaments were observed over Fairbanks during the first POLARIS deployment.

The tropical ER-2 CO data [2] consists of only six tropical flights during 1995-1997 (951105, 960213, 960801, 960808, 961211, and 970923) that sample only parts of this seasonal variation, missing the presumed spring maximum. The profiles obtained show CO declining with altitude in the lowermost stratosphere, with a fairly tight distribution of CO mixing ratios, although with a small (5 ppb, or $\approx 10\%$) but distinct and statistically significant seasonal variation. Median CO mixing ratios just above tropopause level (390 K) are 41 pbb during summer/fall flights (August, September) and 46 ppb in winter (November, December, February). The seasonal median profiles observed by ALIAS in the tropics show mixing ratios declining smoothly with altitude throughout the near-tropopause region (by about 0.6 ppb/°K), but maintaining the 5 ppb seasonal offset. The presumed spring maximum in stratospheric CO, which is not captured by any ER-2 flight, would lie above the observed winter CO values.

Robustness of tropical observations

The tropical CO measurements used to infer initial concentrations are consistent over the three years of observations (1995, 1996, and 1997), and the evident seasonal differences are clearly statistically significant. The 1-σ scatter about the median profiles is ≈ 0.8 ppb

[2] Tropics are defined here as $\pm$ 15 degrees latitude.

(2%) in summer and 1.6 ppb (4%) in winter, considerably less than the 5 ppb seasonal difference. The difference exceeds the stated accuracy of the instrument (5%, or 2.5 ppb) and is almost certainly not due to instrumental drift, since it is consistent between flights in successive years. It also is not the result of seasonal differences in in-mixing of tropospheric air. Comparison with simultaneously measured N_2O profiles, and with NO_y/O_3 correlations that serve as a marker for tropical air, show that only two tropical flights show some evidence of midlatitudes air at altitudes below 400 K θ, 960213 and 960808. For the 960213 flight, when tropical CO appears high, in-mixing of midlatitudes air would reduce rather than amplify the apparent seasonal cycle. In-mixing on 960808 could potentially produce seasonal bias, but CO mixing ratios measured on this day are not markedly different from the other summer flights. The restricted region over which data was taken means that the apparent seasonal difference is also not an artifact of longitudinal variation in CO mixing ratios. Finally, the fact that seasonal differences persist to the 380 K θ surface mean that apparent seasonality is not due to variation in ascent rates in the lower stratosphere.

4.4 Interpretation of Fairbanks data

4.4.1 Model age calculation

To calculate the evolution of CO concentrations in filaments moving poleward, we assume that air parcels move with constant velocity from equator to Fairbanks latitude, arriving on the date of the filament observation. The calculation was repeated for a variety of meridional velocities, with photochemical losses computed at each discrete timestep according to the local reactant concentrations.

It should be noted that this method produces an upper limit for parcel age. In reality, air observed in filaments over Fairbanks has likely spent the largest portion of its stratospheric life in the subtropics, hedged in by the subtropical transport boundary and experiencing relatively high rates of photochemical loss, before being ejected as a filament

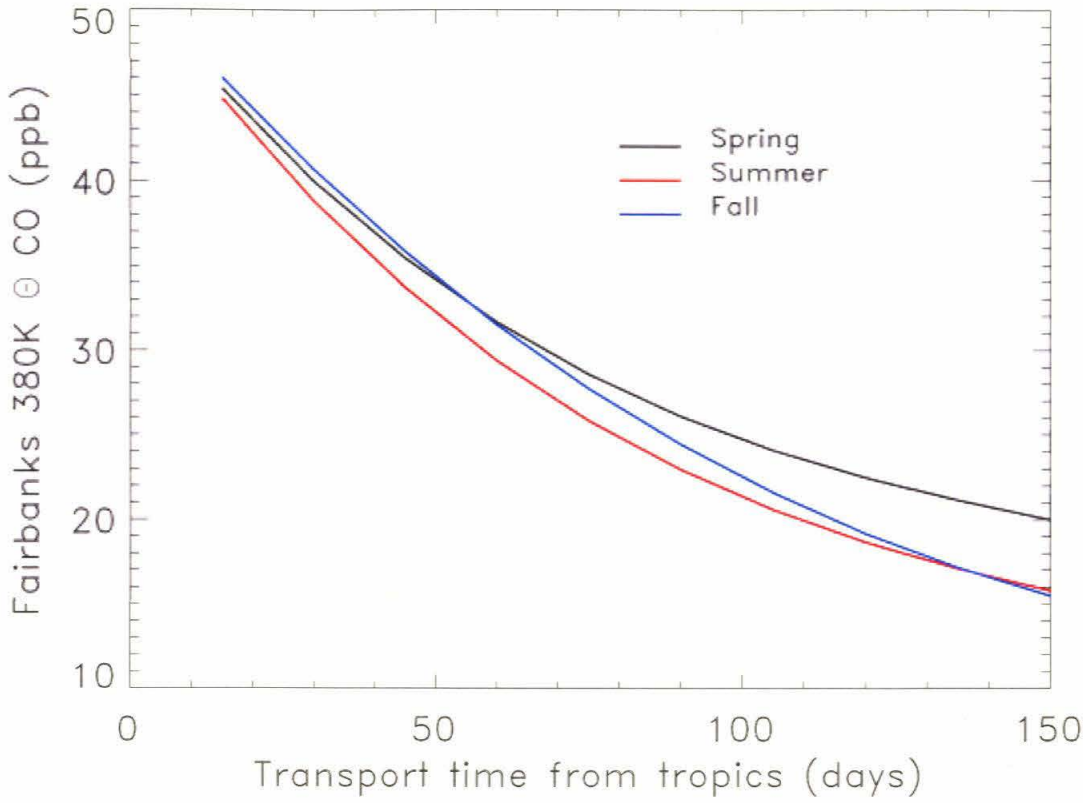

Figure 4.1: Calculated photochemical evolution of filament CO, for the base case assumption of a 50 ppb CO tropical boundary condition at 380 K. The timescale on this plot includes the ascent to 390 K, by which time CO mixing ratio has fallen to 44 ppb, already less than the observed CO mixing ratios in filament cores at 390 K of 46-52 ppb. There are no substantial difference in loss rates between the spring and fall trajectories. Filament ages implied by these loss rates are less than a week, with the largest source of uncertainty the boundary condition for CO.

to make a rapid transit to high latitudes. The assumption that air moves poleward with constant velocity, experiencing lower photochemical loss rates, produces a slight overestimate of filament age. The assumption that filament cores are unmixed tropical air also produces an upper boundary on age; any in-mixing of surrounding older air would increase the estimated filament age.

Age calculations were run for the two strongest filamentation events observed during POLARIS, on 970511 and 970915. The filament cores on both days (at 378 and 390 K, respectively) held CO mixing ratios above tropical median values for the appropriate season, and on 970915, which should be close to the seasonal minimum, filament core mixing ratios exceeded *any* tropical measurements at the same θ-level. Age calculations were therefore run with two initial conditions for CO at the tropical tropause: the median tropical value (50 ppb) and an estimated maximum value of 55 ppb. The +5 ppb error is equivalent to the 2σ variability of the aircraft data plus the instrumental uncertainty. This error estimate should be sufficient to capture uncertainty due to the sampling bias of the aircraft observations; the 2σ variability of tropical upper tropospheric CO in the 3-D photochemical model is only +5 ppb. However, we cannot rule out the possibility that the model does not adequately represent the seasonal cycle of upper tropospheric CO, and spring CO values may be still higher.

Figure 4.1 shows the modeled evolution of air parcels with these initial values for both spring and fall. To simulate the CO expected in filaments at 390 K, air was assumed to first ascend vertically from the tropopause to 390 K and from there move poleward from the tropics along the 390 K θ surface. During its poleward motion the air experiences an average CO loss rate of 1.1-1.3% / day; this loss rate is relatively constant with season and with initial CO boundary condition value. These rates of CO loss imply a near-zero age for the air in filament cores. Even the maximum tropopause boundary condition of 55 ppb CO (48 ppb at 390 K, as compared to filament cores of 46-52 ppb) allows filament cores to have experienced at most 4% loss of CO during poleward motion. The maximum filament ages inferred by this method are then on the order of days.

4.5 CO_2 age confirmation

To reduce the uncertainty in the photochemical age derived from CO measurements can be reduced by comparing that result with the age derived from simultaneous measurements of CO_2 in filament cores. CO_2 is essentially inert in the stratosphere; variations in its

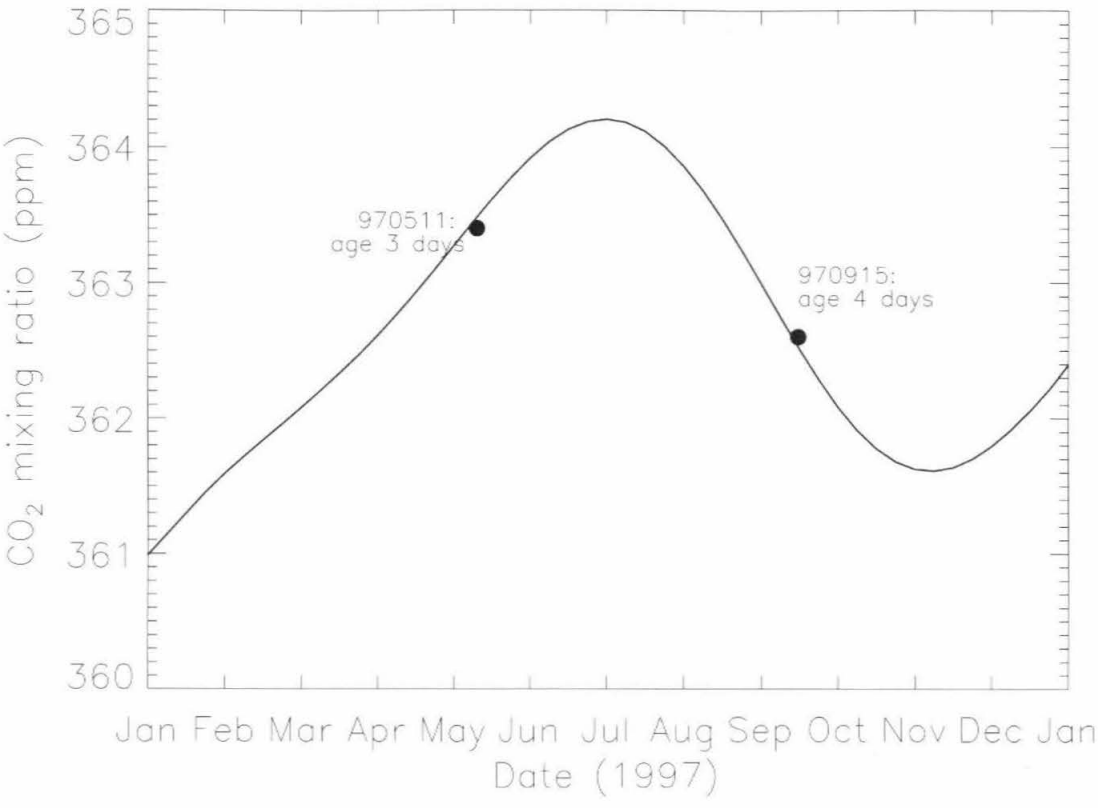

Figure 4.2: Ages of air in filament cores estimated from *in-situ* CO_2 measurements. CO_2 values in filament cores are overplotted on the boundary condition for CO_2 entering the stratosphere in 1997 inferred by Andrews and co-workers. The boundary condition was constructed using a combination of aircraft measurements of stratospheric CO_2 and surface measurements taken at the CMDL monitoring sites; Andrews et al. (1999) describe the procedure in detail. CO_2 data alone is sufficient for this age determination because the filaments are extremely young. Age determination in older air would be made by comparing CO_2 and N_2O values; in these filaments, N_2O is essentially unchanged.

mixing ratio reflect only the well-known secular increase in CO_2 and its seasonal variation. The boundary condition for carbon dioxide in air entering the stratosphere is relatively well understood; Andrews and co-workers have inferred the entering tropical values from a combination of stratospheric aircraft data and surface measurements by the CMDL

(Climate Monitoring and Diagnostics Laboratory) network of monitoring stations (4). The combination of seasonal cycle and secular increase mean that measurements of CO_2 alone do not yield a unique age value for air that is months to a year old. For extremely young air, however, CO_2 content provides the most robust age estimate of all measured stratospheric tracers.

Although CO_2 is a much less sensitive age indicator than CO, i.e. shows a far smaller fractional change for a given variation in age, the instrumentation used to detect CO_2 is correspondingly more precise. The amplitude of the CO_2 seasonal cycle is less than 1% of the mean CO_2 mixing ratio, but the Harvard non-dispersive infrared CO_2 instrument (e.g. 4), which flew on the ER-2 as part of the POLARIS and STRAT payloads, produces measurements estimated to be accurate to 0.1 ppm (with 0.03 ppm precision), 3% of that cycle (Daube, B. *pers. comm.*). The ratio of instrumental uncertainty to expected tracer evolution over three months is then on the order of 10% for both CO and CO_2 measurements, and the CO_2 initial condition is better understood. If each filament core represents an isolated airmass unmixed with surrounding air, the resulting ages inferred from their CO_2 content are 3 $\pm$5 days for the 970511 filament and 4 $\pm$3 days for 970915, with the uncertainty reflecting the propagation of instrument error (Figure 4.2). The CO_2 measurements provide the most accurate age estimate, and confirm that the observed filaments are extremely young, with transport times from the tropics of less than a week.

4.6 H_2O age confirmation

The very young filament ages are also supported by the water vapor mixing ratios in the filaments, which carry with them from the tropics snapshots of the seasonal variation in entering stratospheric water vapor. It is difficult to construct a quantitative age determination from water vapor data alone, because the boundary condition of entering stratospheric water vapor is less well-understood than that for CO_2. As in the CO case, potential inhomogeneity in tropical UT/LS water vapor introduces additional uncertainty in this estimate. Nevertheless, the water vapor mixing ratios observed in the filaments

are clearly consistent with young air ages, and provide confirmation of the age estimates derived from the other tracers.

Water vapor entering the stratosphere shows an annual variation of approximately 3-6 ppm, with a maximum in N. hemisphere summer and minimum in winter; this oscillation is propagated upward as air ascends to create a "tape recorder" signal (45). The Fairbanks filaments echo the tropical boundary condition variation, with water vapor mixing ratios changing from < 3 ppm in May to > 6 ppm in September, as wet as the wettest part of the tropical profiles observed during STRAT. Figure 4.3 shows the 970915 Fairbanks water vapor profile overlaid on the STRAT tropical measurements. The aircraft crossed through young filament air at 390-410 K θ; H_2O in this section of the profile closely matches the STRAT November values. The August STRAT profile, by contrast, has a maximum nearly a ppm smaller, and located at the 380 K tropical tropopause, implying that the seasonal maximum in water vapor entering the stratosphere has not yet occurred. The ascent rate inferred from the profiles yields a time of early September for the seasonal maximum to reach 400 K, and therefore an upper limit of $\approx$ a week for that maximum to be advected from the tropics to Fairbanks latitudes (7, 45).

One means of compensating for the sparseness of ER-2 tropical observations and the uncertainty in the initial boundary condition is to derive a predicted boundary condition for water vapor in entering tropical air. Although the exact mechanism that dehydrates air entering the stratosphere remains controversial, stratospheric water vapor mixing ratios do seem to follow roughly the saturation values determined by tropical tropopause temperatures. Tropical radiosonde data can then be used to infer a seasonal cycle in entering water vapor. Figure 4.4 shows this inferred cycle and the corresponding water vapor observed in the 970511 and 970915 filament cores. This comparison provides an age estimate in the same manner as does comparison with the CO_2 seasonal cycle. The boundary condition remains uncertain to some degree, as is shown clearly for the May filament, which is wetter than the tropical values have been since mid-February. The September filament matches inferred tropical values closely; if filament moisture content is determined by mean tropical saturation, this correspondence yields an upper age limit

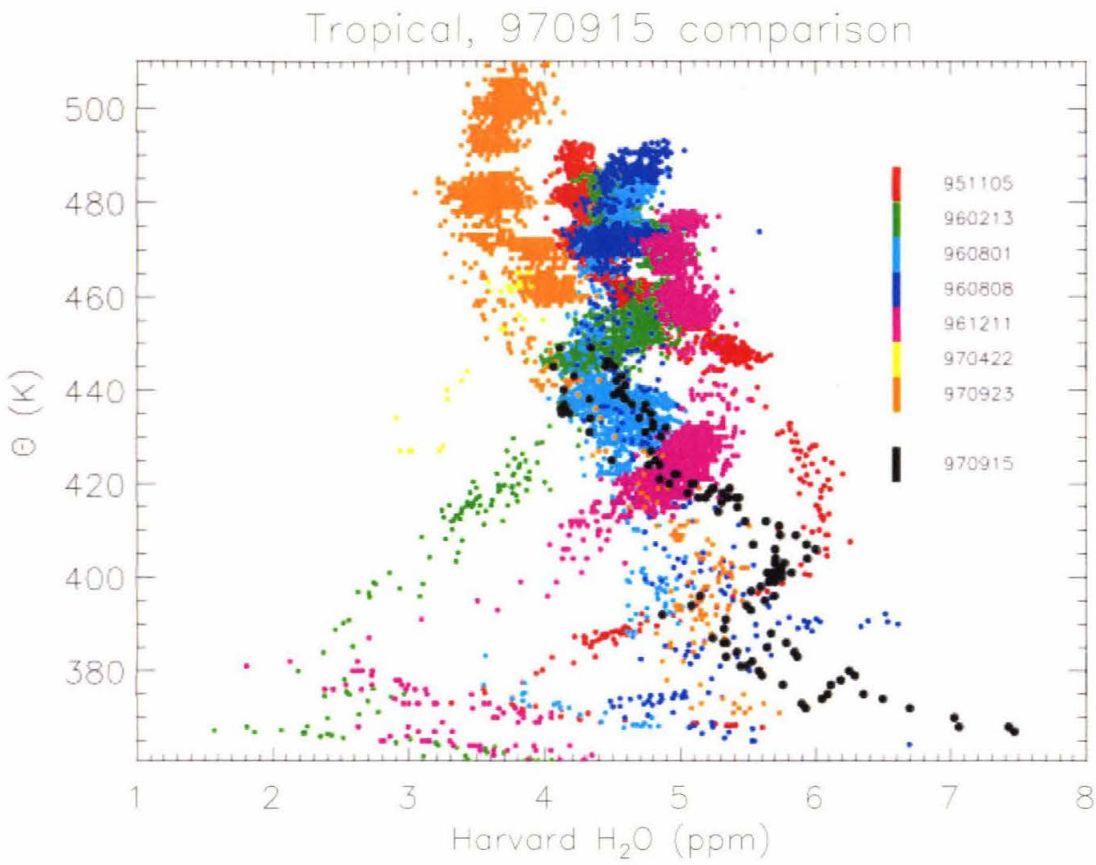

Figure 4.3: Water vapor measurements in the tropics compared to water vapor in the 970915 POLARIS filament. All data were taken by the Harvard Lyman-α instrument. The tropical data are the complete set of profiles obtained in the tropical lower stratosphere, with measurements in late autumn-winter (November, December, February), early spring (April), and summer (August, September) in three successive years (1995-1997) during the STRAT and POLARIS missions. The sinusoidal variation with altitude of χ_{H_2O} is the seasonal cycle in water vapor mixing ratios propagating upwards as air ascends. In the winter profiles, χ_{H_2O} is near minimum at the tropopause (380 K); in mid-summer it is near maximum at the tropopause, with the minimum now advected 100 K upwards. Mixing reduces the amplitude of variation at higher altitudes. The 970915 Fairbanks profile which crosses a filament is plotted in black; the aircraft passed through filament air between 390-410 K θ. Water vapor values in the filament core match those of the late autumn STRAT data, and would be out of phase with profiles from earlier months. Note that the shape of the 970915 profile is determined simply by the location of the filament and its relatively older surrounding air. The falloff above and below the filament core represents the transition between young and old air, not a time-varying "tape recorder"

on the order of a week. This age determination, like that made with CO values, is less robust than that derived from CO_2. The initial H_2O boundary condition is uncertain by perhaps 20% out of a total signal of $\approx$ 100% seasonal variation (and $\approx$ 50% gradient tropics-high latitudes). Nevertheless, the agreement of several independent means of estimating filament age lends support to the young ages derived.

4.7 Discussion

Age estimates by the CO photochemical clock and the CO_2 seasonal cycle yield ages of between 0 - 1 week for the filaments observed over Alaska, an estimate consistent with the H_2O seasonal cycle. The agreement of these independent methods of estimation strongly supports extremely young ages for the filaments. The combination of methods also allows us to eliminates some physical scenarios that might produce error in age calculations.

The two primary possible sources of error are 1) dilution of filament cores by background air and 2) uncertainty in initial CO or CO_2 values. Initial-value uncertainty is possible for both species, even if the mean CO_2 boundary condition is assumed to be perfectly known. If filamentation is associated with processes bringing atypical air to the stratosphere, e.g. convective activity which propels air from surface to stratosphere without the usual 2-month apparent delay, then initial values for both CO and CO_2 would be much higher than the mean, and estimated filament ages would be erroneously young. Dilution by older background air has the opposite effect, producing older apparent ages for both species. We regard it as enormously improbable that the apparent youth of the POLARIS filaments could be produced purely by anomalous initial values, since the CO_2 data show that the increased residence time in the stratosphere would have to exactly match the decrease in residence time in the troposphere. The combination of CO and CO_2 data also tend to rule out combinations of dilution and initial value problems as the source of the young ages. The same argument against excessive coincidence again applies, but in addition the correspondence of CO and CO_2 ages argues against any signficant amount of dilution of the filament cores. The variation in CO_2 over a few-month period

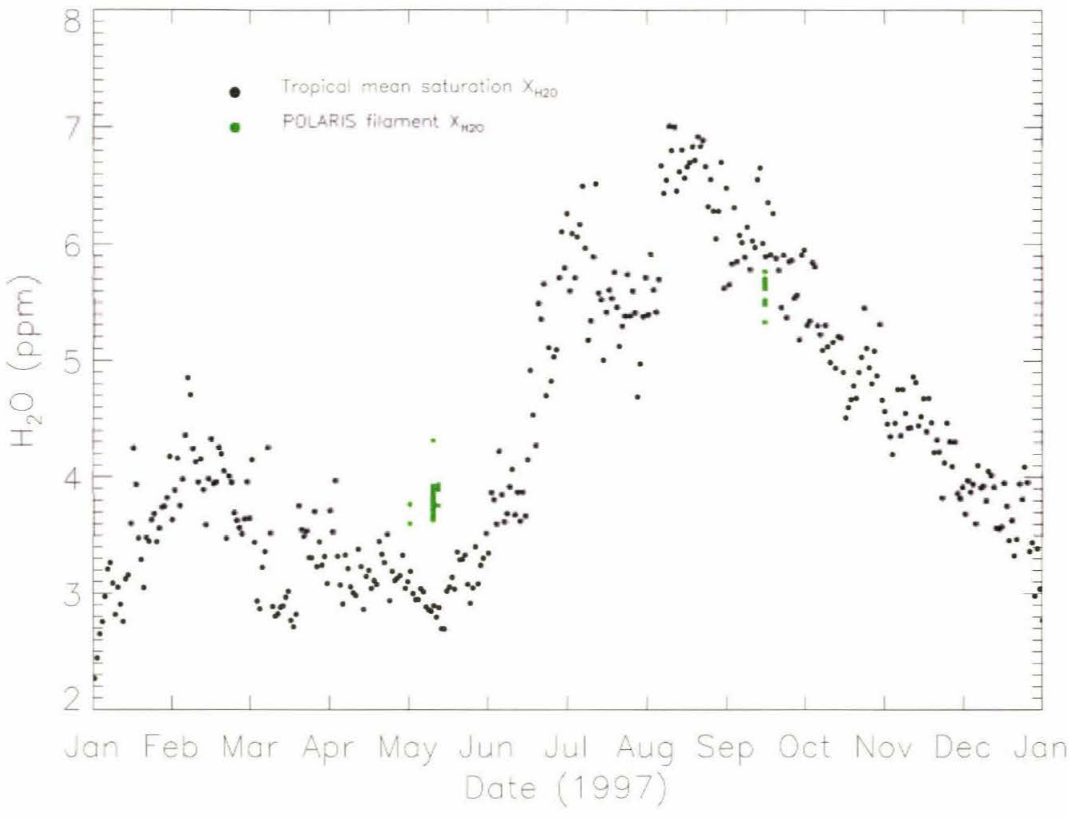

Figure 4.4: Water vapor content in the 970511 and 970915 POLARIS filaments compared to minimum saturation mixing ratios in the tropics derived from daily WTO radiosonde data. Filament mixing ratios are shown in green; the data here are all points between 380 and 410 K θ with CO > 40ppb during the ER-2 transit through the filaments. The tropical seasonal cycle was derived by defining a grid of 4 by 5 ° over the tropics (±10° latitude) and assigning each gridpoint a daily value equal to the weighted average of $\chi_{H_2O\ min.}$ over all sonde profiles contained in the grid square. (Weighting is exponential with distance from the grid center). The points displayed here are the daily means of all tropical gridpoints. The resulting values are relatively insensitive to the gridding scheme (77). Although individual stratospheric air parcels may deviate from these mixing ratios, the seasonal cycle produced reproduces fairly well the observed seasonal cycle of stratospheric water vapor.

is approximately linear (both filament observations are conveniently located on the near-linear portions of the seasonal cycle), and decline in CO is exponential. Any substantial mixing of older environmental air would produce different ages by the two methods. Taken together, these data form a strong confirmation of extremely rapid isentropic transport in the observed filaments, with the initial filament air being roughly representative of the tropics.

Finally, if we have confidence in the CO_2 ages, these can be used to constrain the amplitude of the seasonal cycle of CO entering the stratosphere. If we consider the spring filament to be undilute and less than a week old, as the CO_2 mixing ratio suggests it is, then it samples tropical spring stratospheric CO of 46 ppb at 378-388 K, no higher than the winter values observed during ER-2 flights in the central Pacific tropics. Although the origin of the filament air is not known, this CO value can reasonably be interpreted as an upper bound for CO in the central Pacific; locations outside the clean Pacific generally have higher CO mixing ratios. Stratospheric CO seasonal variation in the central Pacific region appears then to be no more than ≈ 5 ppb (10%), with no large spring maximum that is missed by aircraft sampling. Despite their the high-latitudes location, the POLARIS flights provide the first spring observations of tropical air to add to the record of seasonal variation in the lower tropical stratosphere.

Chapter 5

WISP Instrument

5.1 Introduction

The tiny amounts of water vapor in the upper troposphere and lower stratosphere have enormous leverage on climate, affecting both radiative balance and atmospheric chemistry. Unfortunately, water vapor is also the most variable atmospheric component, and we have little understanding of the processes that control water vapor concentrations at these altitudes. This incomplete understanding is the single largest source of uncertainty in climate predictions (24). Determining the factors which control the distribution of water vapor in the atmosphere is of critical importance to climate studies.

The most useful tracer for this purpose is the vapor's isotopic composition: the concentrations of HDO and $H_2{}^{18}O$ molecules relative to $H_2{}^{16}O$ (46). All processes involving condensation, evaporation, or other phase changes leave an isotopic signal in the residual water vapor, because in thermodynamic equilibrium, the heavier isotopomers partition preferentially into t he condensed phase. In this way vapor isotopic composition carries a record of its entire convective history. Horizontal advection of undersaturated air, on the other hand, cannot alter isotopic composition, so away from convective regions isotopic composition acts as a conservative tracer, and can be used to diagnose mixing of air masses. Because different scenarios for bringing water vapor to the stratosphere

and upper troposphere involve differences in condensation, evaporation, and mixing, they produce distinct isotopic signatures. These signatures are not subtle: the fractionation of deuterated water is so strong (α [1] of 1.4 near the tropopause), and the overall loss of water so great (water vapor mixing ratios fall by a factor of 10^4 from surface to stratosphere) that the expected variations in isotopic composition are at the tens of percent level rather than the few per mil of most isotope geochemistry (46).[2] Figure 5.1 shows the differences in expected isotopic profile for two scenarios of transport of air into the stratosphere.

Despite their potential utility, few measurements of vapor isotopic composition in the lower stratosphere exist, and none in the uppermost troposphere, the altitudes of greatest scientific interest. The measurement is difficult because of the scarcity of the isotopomers: the most useful tracer, HDO, has sub-ppb mixing ratios in these regions. Remote sensing has provided some stratospheric measurements, by far-infrared emission spectroscopy (10, 16, 34). or mid-infrared solar occultation absorption spectroscopy (58, 46), but these techniques tend to lose sensitivity just above the tropopause, and their horizontal resolution is on the order of several hundred kilometers. Measurements by sample collection over a cryogen and subsequent laboratory mass spectroscopy have been made up to the middle troposphere (69, 18), but this approach is problematic in the dry upper troposphere and above, because incomplete collection produces strong fractionation artifacts. Obtaining isotopic measurements in the scientifically critical upper troposphere/lower stratosphere region requires a new approach.

Techniques currently used for *in situ* atmospheric water vapor measurements n these regions – Lyman-α photofragment fluorescence and frost-point techniques – cannot discriminate between isotopomers. Meanwhile, the mass spectrometric techniques that are standard for measurement of water vapor isotopic composition in the laboratory are extremely difficult to implement in an autonomously running flight instrument. The dryness

[1] α is the fractionation factor between vapor and condensate, i.e. $R_c = \alpha R_v$, where R is the ratio of heavy to light isotopomers.

[2] Isotopic composition is typically given in δ notation in per mil units, as the per mil difference in isotopic ratio between the sample and a measurement standard: $\delta = 1000(R_{sample}/R_{standard} - 1)$. For water vapor the usual standard is mean ocean water.

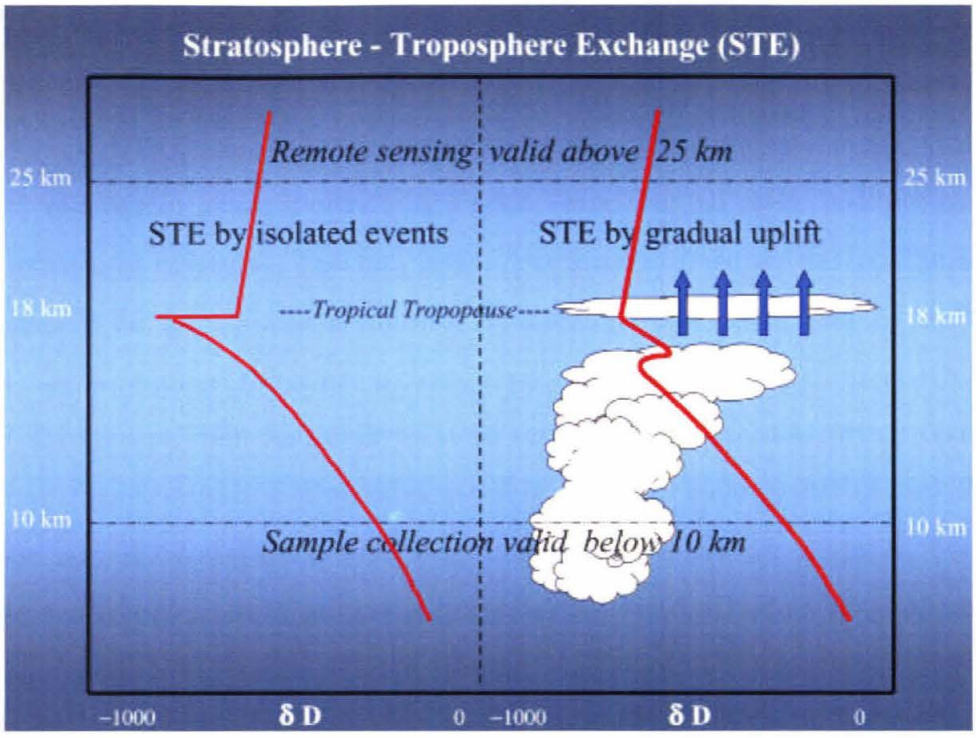

Figure 5.1: Examples of δD profiles for differing scenarios of troposphere-stratosphere exchange. R. profile: transport into the stratosphere occurs by gradual ascent over the uppermost few km of the troposphere, with dehydration occurring in thin cirrus Water vapor isotopic composition must follow a Rayleigh distillation decline with altitude over these few km, and is continuous across the tropopause throughout the region of ascent. Strong enhancement of vapor must have occurred at the base of this ascent region, most likely through evaporation of detraining cloud ice, to match known stratospheric δD. L. profile: STE occurs in by cumulus towers, and enhancement of stratospheric δD can occur above the tropopause. The cartoon here shows a possible profile in tropical regions where penetrative cumulus convection is not occurring. Tropospheric and stratospheric δD show a sharp discontinuity at the tropopause, with tropospheric δD following Rayleigh distillation up to the tropopause, and the stratosphere enhanced in deuterium by evaporation of ice elsewhere. In the actual atmosphere, isotopic profiles will likely be affected by cloud detrainment and mixing at a variety of levels and isotopic profiles may be more complicated. The dashed lines represent the limiting altitudes of current measurement techniques for δD: none provides measurements in the region where profiles would differ.

of stratospheric air (< 5 ppm), the enormous dynamic range of water vapor concentration from surface to stratosphere (four orders of magnitude), the mass equivalence between $H_2{}^{17}O$ and HDO, non-reproducible fractionation during ionization, and the inherent "stickiness" of a highly polar molecule like water vapor air all make in-flight mass spectrometry extremely difficult. The last issue, "stickiness", means that contamination is a major concern for any *in-situ* method of measuring water vapor and its isotopomers. Enormous care is required to ensure a clean measurement in any instrument which draws sample air through an inlet and exposes it to surfaces on which adsorption could occur. The problem of contamination eliminates not only potential techniques but also platforms: water vapor cannot be measured from large research balloons, for example, because the air sampled is contaminated by outgassing of water vapor adsorbed on the balloon surface, even during descent. The most reliable approach is therefore a completely passive technique in which the air sampled is completely undisturbed. Tunable diode laser absorption spectroscopy (TDLAS) represents just such a technique. At the time this work was begun there existed no TDLAS instrument which could adequately measure water vapor isotopes. For this purpose an instrument must be aircraft- rather than balloon-mounted, with a long enough pathlength to provide the sensitivity needed for measuring scarce HDO, and designed to minimize both potential contamination by surface adsorption and systematic error that would affect the measured isotopic ratio. This chapter describes a new TDLAS-based instrument designed to provide *in-situ* measurements of water vapor isotopic composition in the upper troposphere/lower stratosphere region.

5.2 Instrument description

The Water Isotope SPectrometer (WISP) is a 3-channel open-path tunable diode laser absorption spectrometer designed for in-situ measurement of water vapor and its isotopic composition from aircraft platforms (Figures 5.2 and 5.3). The instrument uses well-established TDLAS techniques to make simultaneous measurements of H_2O , HDO, $H_2{}^{17}O$, and $H_2{}^{18}O$ as well as CH_4. (See for example (66, 21, 50, 76, 41, 67)). Laser light is in-

Figure 5.2: The WISP instrument, mounted beneath the wing of the WB57 aircraft. The dewar containing the lasers and the optical head (black) are enclosed within a fairing during flight; the open-path cell extends into the free air. This photograph was taken during integration, before installation of cell mirrors, cabling, and insulation

jected into a multipass optical cell (94 passes in a 1 m. cell) mounted in the free air below the aircraft wing and is tuned over individual molecular absorption lines. The resulting absorption spectra provide a measurement of gas concentration between the mirrors. Redundant measurements on the three channels are used for cross-calibration to ensure accuracies on the few percent level for the isotope ratios. Measurements are made with two mid-infrared nitrogen-cooled lead-salt lasers (in the ν_2 fundamental ro-vibrational wa-

Figure 5.3: The WISP instrument in flight-ready configuration, with the fairing installed. The multipass cell sits in the airstream so that air sampled is wholly undisturbed, preventing potential contamination problems.

ter vapor absorption band at 6.7 μm) and a single near-infrared thermoelectrically cooled III-V semiconductor laser [3] (in the $\nu_1 + \nu_3$ overtone band at 1.37 μm). The estimated sensitivity of the instrument in flight is equivalent to linecenter absorptance of a few parts in 10^5, yielding a predicted SNR of > 10 for all isotopomers up to the tropopause (see figure 6.4). The combined precision and systematic measurement errors are expected to be in the range of a few percent, much larger than the best achievable by laboratory

[3] III-V lasers are so termed because they are manufactured from semiconductors composed of elements from columns III and V of the periodic table.

mass spectrometry, but more than adequate for the science in question where the signals are enormous by geochemical standards. The instrument is designed for use on two different aircraft platforms, the unmanned solar-powered ultra-high-altitude Centurion, built by the AeroVironment Corp., and NASA's more conventional WB-57 stratospheric research aircraft. Test flights on the WB-57 were completed in 1999, and the instrument is scheduled to make science flights in 2001.

5.3 Design Constraints

The WISP design represents the accommodation of two conflicting requirements. The contamination concerns discussed above meant that water vapor isotopomer measurements are most easily made with an open-path configuration, with the measurement cell hanging outside the aircraft in undisturbed air. But the small absorbtances expected would typically require a more stable instrument environment inside the fuselage. Although individual absorption lines for HDO are as strong as the deepest water lines, the isotopomers are far more scarce – HDO levels in the stratosphere are less than a ppb – so the optical pathlength needed for detection is very long ($\approx$ 100 m). Maintaining alignment is therefore more difficult. WISP is the largest open-path aircraft instrument flown without actively-controlled mirror alignment, and as such represented an engineering challenge. The two aircraft for which the instrument is designed also placed conflicting constraints on the instrument. WISP was initially designed for the slow-flying experimental aircraft Centurion, and later adapted for the twin-jet-engine WB-57. Accommodation on the lightweight Centurion – a single flying wing over 200' long whose primary components are carbon fiber and foam – placed severe restrictions on instrument size and weight. Mounting on the WB-57, however, increased the requirements for structural stability, because the plane's faster airspeed exposes the instrument to far greater aerodynamic forces than those experienced on Centurion.

5.3.1 Size and Weight

Centurion payload capacity is only 90 kg at any given mount point (with the maximum total capacity of 300 kg). Because the aircraft's peak altitude and flight duration in the stratosphere are strongly dependent on payload weight, keeping instrument mass well below these limits was strongly desirable. The Centurion has no payload bays, and what parts of the instrument cannot fit within the 12" wing depth must hang in the airstream below. The wing dihedrals sharply in flight, meaning that the instrument would be subjected to unacceptable stresses if it were mounted horizontally from two distinct points. Instead it must hang vertically from a single mount point, and therefore must be contained within the vertical clearance from ground to top of wing spar of only 70". Figure 5.4 shows the original mounting arrangement for the instrument, which set its size constraints.

5.3.2 Contamination Issues

Contamination concerns meant that the payload constraints listed above could be met only with an open-path system, in which the optical cell is simply mounted in the free airstream, and measurements made in the ambient air. A gas handling system designed to minimize contamination would have added unacceptably to the size, weight, cost, and power requirements of the instrument.

5.3.3 Structural Stability

The primary concerns for the mechanical design of the instrument were the stability of the optical system and multipass cell, and the safety of the aircraft mounting mechanism. Both are of great concern for an instrument mounted external to any aircraft, and in this case especially so on the WB-57. The instrument had to be sufficiently rigid against vibration and against flexure from wing movement to maintain alignment of the mirrors, but still had to present minimal surface area to reduce drag. Combined with the size constraints above, this mandated an extremely compact instrument, designed around a

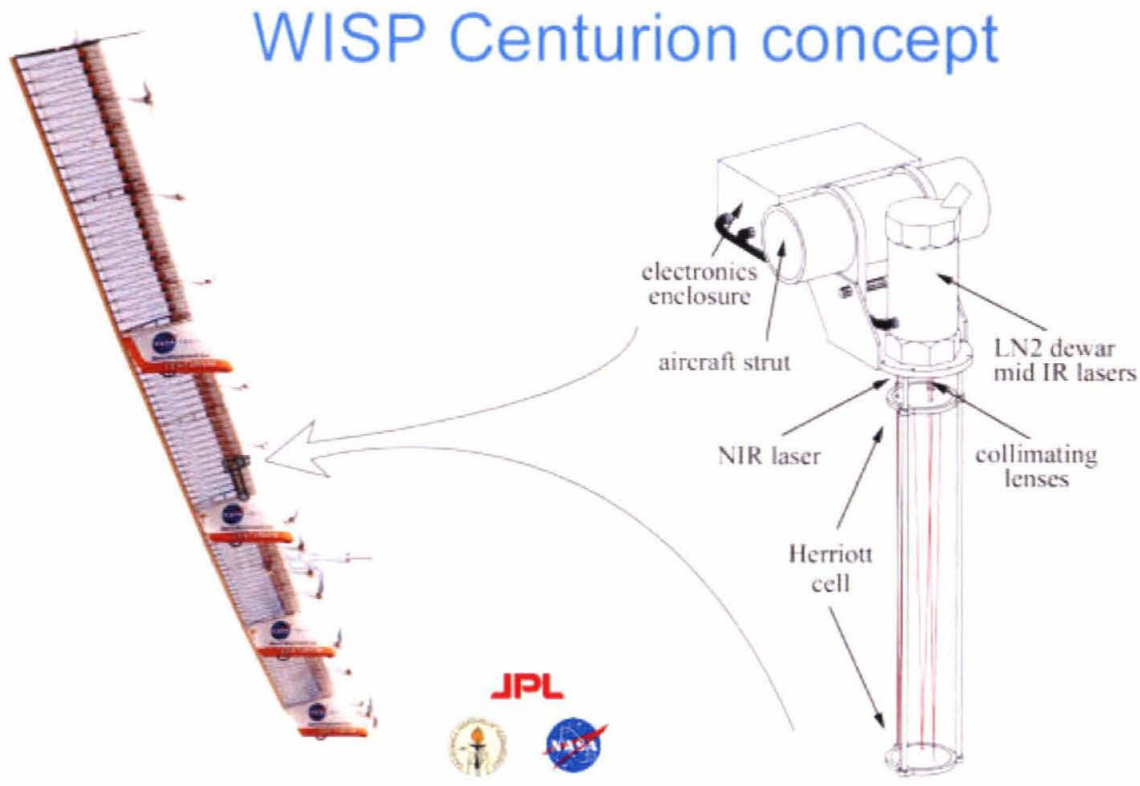

Figure 5.4: The WISP instrument and its mounting configuration on the Centurion aircraft. The flexibility of the Centurion wings mandates a vertical mounting arrangement. The height of the main aircraft spar then limits the size of the instrument.

single bulkhead, with as short an optical path as possible before the multipass cell.

5.3.4 Thermal Stability

During ascent to the tropopause the externally mounted instrument sees a drop of over 100 degrees Celsius in ambient temperature. Although strip heaters on the surface of the instrument can mitigate temperature changes to some extent, the large thermal mass of the instrument means that it it is not possible to hold it at a constant temperature without prohibitive power consumption. It was therefore necessary to engineer the instrument so as to avoid distortion of its optical system by differences in thermal expansion and con-

traction of its components. (The multipass cell used loses alignment if mirror separation changes by 0.25 mm, or input beam angle by a third of a degree.) Within the nitrogen dewar, on the other hand, the diode lasers must be held at temperatures constant to 10 mK during an 8 - 15 hour flight to prevent their wavelengths from drifting away from the desired spectral region.

5.3.5 Instrument Control

Because the WB-57 has no active telemetry capability, the instrument must operate autonomously for the duration of the flight, with only a single "on" switch under the control of the pilot. There is no opportunity for in-flight monitoring of instrument performance or adjustment of measurement parameters by the scientist. Instrument operation must therefore be robust enough for stand-alone performance.

5.4 Mechanical Design

The resulting WISP mechanical design is both rugged and compact, and can be used on a variety of aircraft platforms with only minor modifications. The instrument consists of five main subsystems: 1) a liquid nitrogen dewar containing two mid-infrared lead-salt lasers, 2) a pressurized optics enclosure (the "optics can") containing a near-infrared laser and focusing and collimating optics for all three channels and pressurized to 1 atm. of dry N_2, and 3) a multipass Herriott cell consisting of two spherical mirrors spaced exactly 1.004 meters apart by three support rods, 4) mounting attachments for the WB-57 (or other) aircraft, and 5) a separate electronics box. The optical systems (1-3) are discussed in more detail in the following section.

The primary attachment point to the aircraft is the mount plate, which forms the central bulkhead of the instrument, with the optics head (collectively, the dewar and optics can) on one side and the Herriott cell on the other The beam path is direct, allowing all steering optics to fit in a can only 2.5" in height. On the Centurion, the instrument is mounted vertically; on the WB57, horizontally, with the far mirror supported by a beam

attached to the wing hatch covers, and the optical head enclosed by a fairing extending from an instrument spearpod. The entire instrument is 65" in length, with a mass of 38 kg in its WB57 configuration (including 8 kg of electronics and cabling, and excluding the fairing). By comparison, the predecessor 4-channel ALIAS spectrometer built by the same JPL group weighs 72 kg, and the balloon-borne 2-channel open-path ALIAS-II 40 kg (76, 67).

5.4.1 Thermal control

The optical head and electronics box of the instrument are maintained at 20 °C by strip heaters and self-regulating heater controllers (Minco, Inc.) and Nomex fiber cloth insulation. The bulk of the power usage on the instrument – up to 300 W – goes to these structural heaters; signal processing and laser control consume less than 10 W. The multipass cell, on the other hand, cannot be thermally regulated without prohibitive power consumption. Although the mirrors are heated slightly above ambient to prevent condensation on their surfaces, thermal strategy is primarily to engineer the multipass cell so that it maintains alignment even while experiencing large temperature changes. Thermal contraction causing the mirror separation to shorten by 0.25 mm, for example, would cause all signal on the detector to be lost. While the mirror mounts are 7075 Aluminum, the three rods separating the multipass cell mirrors are made of Invar 36, a nickel-iron alloy with coefficient of thermal expansion 1.3 $\mu m/m$°C at 20 °C, an order of magnitude lower than steel or most composite compounds, and the mirror substrate is Zerodur glass ceramic (Schott), with CTE 0.1 $\mu m/m$°C. The expected change in the relative positions of the mirror surfaces throughout the range of temperatures experienced in flight is less than 0.15 mm.

5.4.2 WB-57 Interface

The instrument mounts below the right wing of the WB-57, with the dewar and optics can mounted on a reinforced wing tiedown point and fully enclosed by a composite fairing

(Zivko Aeronautics). (The separate electronics box mounts within the wing itself, about 3' from the tiedown point). The Herriott cell mirrors and support rods extend outboard from the fairing in the free air, perpendicular to the direction of flow (see figures 5.2, 5.3). The far (outboard) mirror is supported by an external sheet metal beam transverse to the airflow that spans two preexisting wing hatch covers. The external beam was needed because concern for the integrity of the fuel storage in the front third of the wing precluded the use of the forward wing spar. Mounting was also complicated by the fact that the WB-57 wings flex strongly: although the wings are flat in flight, the wingtips can drag on the runway on landing, especially if fuel tanks are still close to full. To isolate the instrument from this flexing, it is mounted with three pivots, one at the near side and two at the far side. The pivots (Aurora Bearings) are designed to accommodate a maximum of 1.5" of vertical wing flex, a margin of nearly ten over the estimated actual maximum wing flex of 0.19". To prevent wing flex from stressing the support beam, the near side beam bolt holes are slotted, and the beam is free to slide along a Teflon interface with the wing.

The maximum aerodynamic loads experienced by the WB-57 occur at takeoff (190 knots, or 98 m/s), at a dynamic pressure of 0.85 psi. To reduce the resulting moments on the hatch cover bolts (as well as to minimize turbulence within the volume of air sampled) the Herriott cell support rods are covered with an aerodynamic fairing that is estimated to reduce their drag coefficient by a factor of 3. The rods are relatively large in cross-section (1.25" OD) because of the need for stiffness: rod bending and relative motion must be kept below a level that would unacceptably distort the optical cell (Δ0.25 mm mirror spacing, Δ0.3° relative mirror tilt, Δ0.3° change in beam input angle), and the natural frequency of vibration of the instrument must be kept considerably above the scan frequency of the spectrometer to prevent artifacts in the baseline scan power. To minimize weight, the Invar rods are custom-drawn tubing with 0.05" wall thickness (Specialty Steel). A stiffening plate midway along the Herriott cell further increases the system's rigidity. The instrument sits below the boundary layer of the aircraft wing and far enough outboard to be unaffected by airflow along the fuselage.

The instrument's exposure beneath the aircraft wing means that the consequences of mechanical failure would be drastic. Although engineering safety margins are generous throughout, the instrument design incorporates numerous safety features to prevent any possibility of dropped objects in worst-case scenarios. The support rods are fastened to the mount plate (and mirror mounts) with 2-piece split-ring clamps (Ringfeder), but are also secured with roll pins. In the event that the far mirror attachment fails, a bumper prevents the instrument from pivoting down below the level of the aircraft landing gear, and snap rings provide backup security to keep the mirrors from sliding off the rods. The fairing which surrounds the optical head of the instrument has an air ramp just before the instrument aperture to prevent air scoop. All structural bolts are either locking or are secured with safety wire before flight. Flight preparation also includes covering the edges of the main fairing with flight tape and sealing the edges of the rod fairings with silicone adhesive. The total time required to mount and secure the instrument for flight is approximately two hours, of which 45 minutes are required for the beam and far mirror swingarm, which can be left in place between flights.

5.5 Optical Design

The optical train of the instrument contains the bare minimum of elements, both for compactness and to minimize optical fringing. The latter is usually the limiting factor governing the sensitivity of TDL instruments. The instrument therefore has a direct optical path and no beam steering mirrors. Light from the lasers in the dewar (channels 2 and 3) passes directly into a sealed optics can containing all focusing and collimating lenses. The optics can also contains the channel 1 near-IR laser mounted directly on the dewar cover (figure 5.5. In the optics can, light from each channel is collected by a collimating lens which steers the beam into the multipass cell (through a hole in the near side mirror) at the appropriate injection angle and focuses it at cell midpoint. Within the cell light passes back and forth 94 times before exiting out its original entrance hole and returning to the optics can, where it is directed onto a detector by a focusing lens. Detectors for all

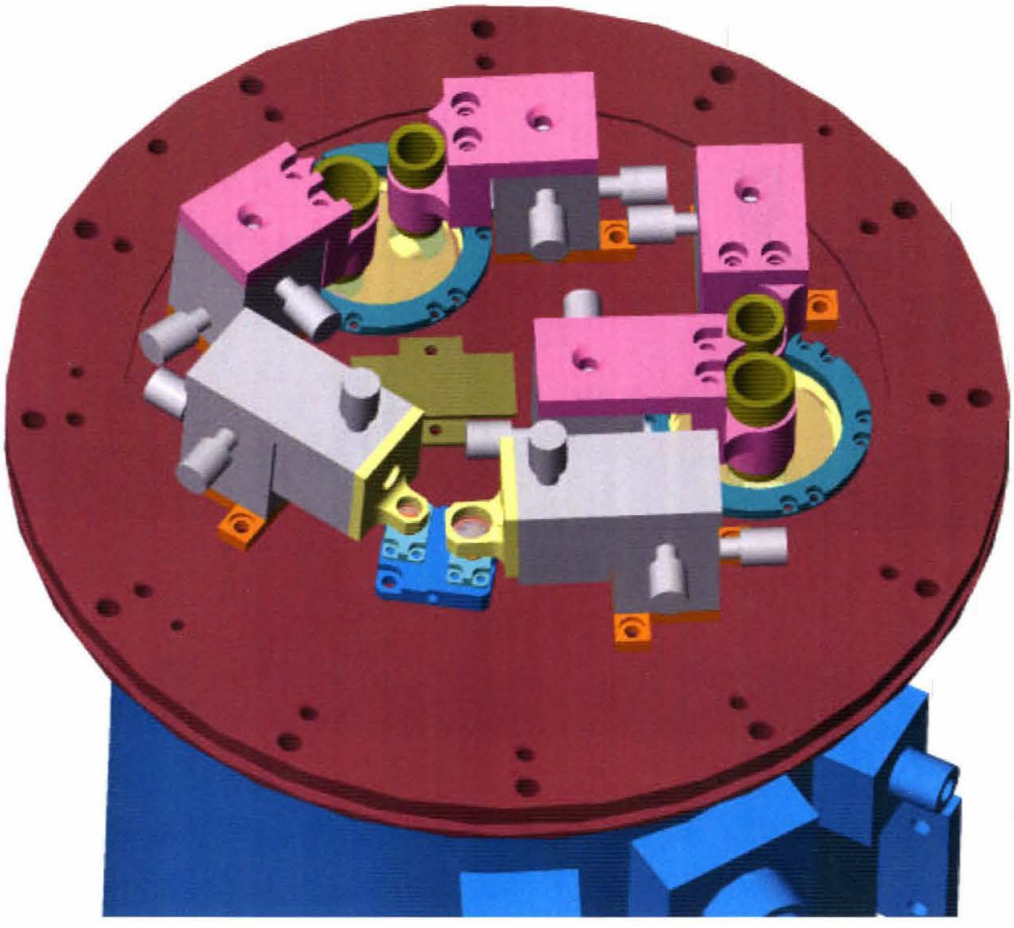

Figure 5.5: Focussing/collimating optics on the dewar cover, with the optics can removed. The lead-salt laser channels 2 and 3 are in the rear, with lenses in lens barrels; the near-IR channel 1 is in the foreground, with laser and detector mounted on a thermoelectric cooler (blue).

channels are mounted beside the lasers, i.e. within the dewar for channels 2 and 3, and on the dewar cover for channel 1. For best possible collimation with this simple system, laser and lens mounts are machined to pre-steer each beam into the multipass cell and keep the lens perpendicular to the beam. On the WB-57, the instrument is mounted so that the optics can surface is flush with the edge of the main fairing. The channels then see no dead air space other than the can, which is either evacuated or backfilled with dry nitrogen. In this way the system measures absorption only in the free airstream.

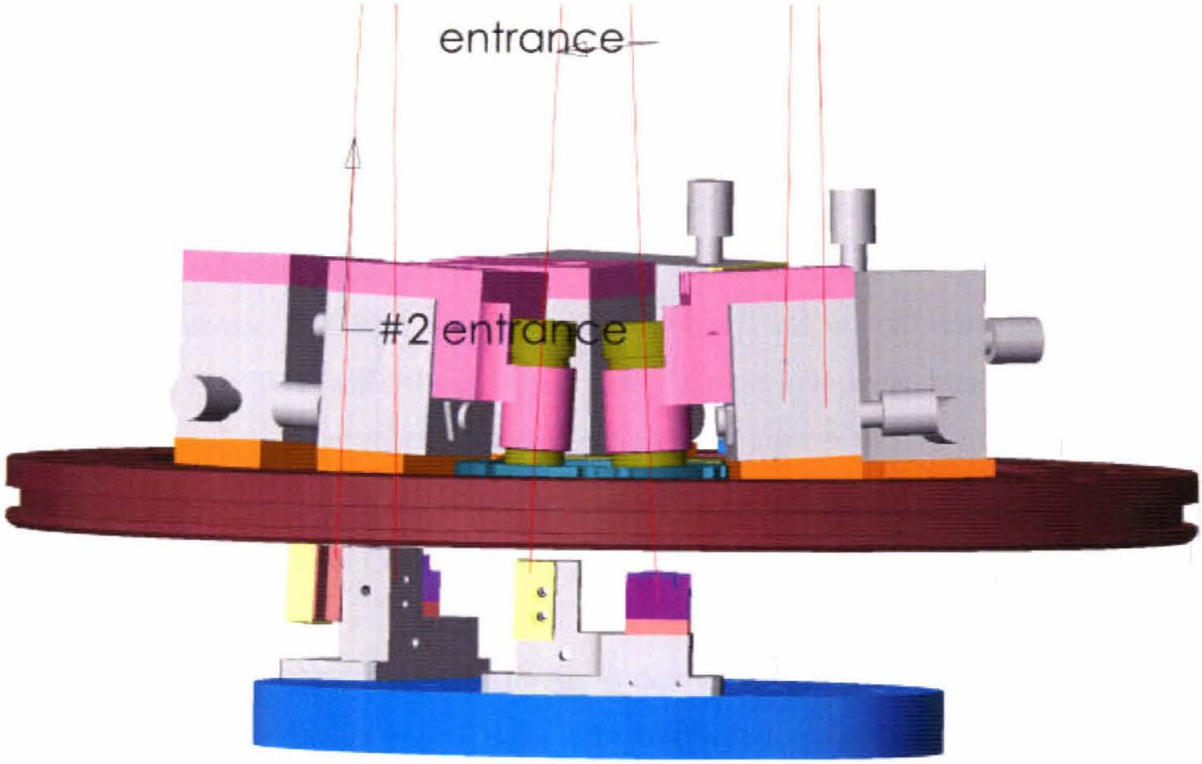

Figure 5.6: Laser and detector assembly within the dewar, with the beam paths modeled in red.

5.5.1 Dewar

The two mid-infrared lead-salt lasers on WISP operate only at cryogenic temperatures. They (and their associated detectors) are housed in a 2.2 l aluminum LN2 dewar (Kadel Engineering). Figure 5.6 shows the elements of the laser/detector assembly within the dewar. All elements mount to a ⌀ 5.5" aluminum cold plate in direct contact with LN2, and are shielded from thermal emission from the warm dewar skin (at 300 K) by a cold shield of polished, gold-plated aluminum. The TDLs are mounted on separate cold fingers of high-conductivity oxygen-free copper electroplated with gold, each paired with its detector. Since lasers may require very different temperatures to operate at the desired wavelengths (anywhere between 78 and 105 °K), they are heated individually by resistive heating elements mounted on the laser package. The lead-salt TDLs are currently operated with only passive temperature regulation, with constant applied voltage for the

duration of each flight. The separation of the cold fingers is intended to facilitate the addition of active temperature control at a later date, by minimizing thermal feedback that would cause oscillations in the control circuits. Because the laser package is not electrically floating – the laser case is laser ground – sapphire shims (.01" thick, Boston Piezo) isolate the cold fingers from the cold plate and dewar body to prevent noise pickup on the laser current. Sapphire is an electrical insulator, but an excellent heat conductor, with conductivity 23 W/mK (about 1/10th that of copper). Indium shims are used around the sapphire and on other metal-to-metal junctions to ensure good thermal contact.

Temperature stability of the dewar is ensured by regulating the vapor pressure above the LN2 with two high-precision pressure relief valves in series (Tavco Corp.). The dewar hold time is $>$ 24 hours with no applied heat load, and typically 17 hours when lasers are operated. The heat load of the dewar is dominated by parasitic heat load (largely conduction through the internal wiring). The heat applied to the lasers for thermal regulation is less important. Resistive heating in the lasers themselves is significant only for very high-current ($>$ 1 A) lasers. To minimize parasitic heat load, most wiring is 32-gauge phosphor-bronze, with lower thermal conductivity than copper (LakeShore DuoTwist and QuadTwist). The dewar is designed to be used in either horizontal or vertical configuration. For horizontal use, an internal foamed metal wick maintains thermal contact with the cold plate when the nitrogen reservoir is low.

The mid-infrared TDLs are narrow-linewidth lead-salt diode lasers (Laser Photonics, Laser Components), emitting a few mW power. Their associated detectors are 2 mm $\times$ 2 mm HgCdTe photoconductive detectors (Electro-Optical), with rated detectivity of $D^* = 3.5 \times 10^{10}$ cmHz$^{1/2}$/W at 6.7 $/mu$m. The detectors are enclosed in an additional 77K cold shield with a 0.14" aperture to reduce thermal noise (Figure 5.7). In this configuration, optical fringing rather than detector noise is the limiting factor on measurement precision. Laser and coldfinger temperatures are monitored with four silicon diode temperature detectors (LakeShore). To prevent direct backreflections of laser light on laser or detector, the inner roof of the detector cold shield and the cold finger surface below the laser are machined so that no surfaces are perpendicular to the beam. The inner surface of the cold

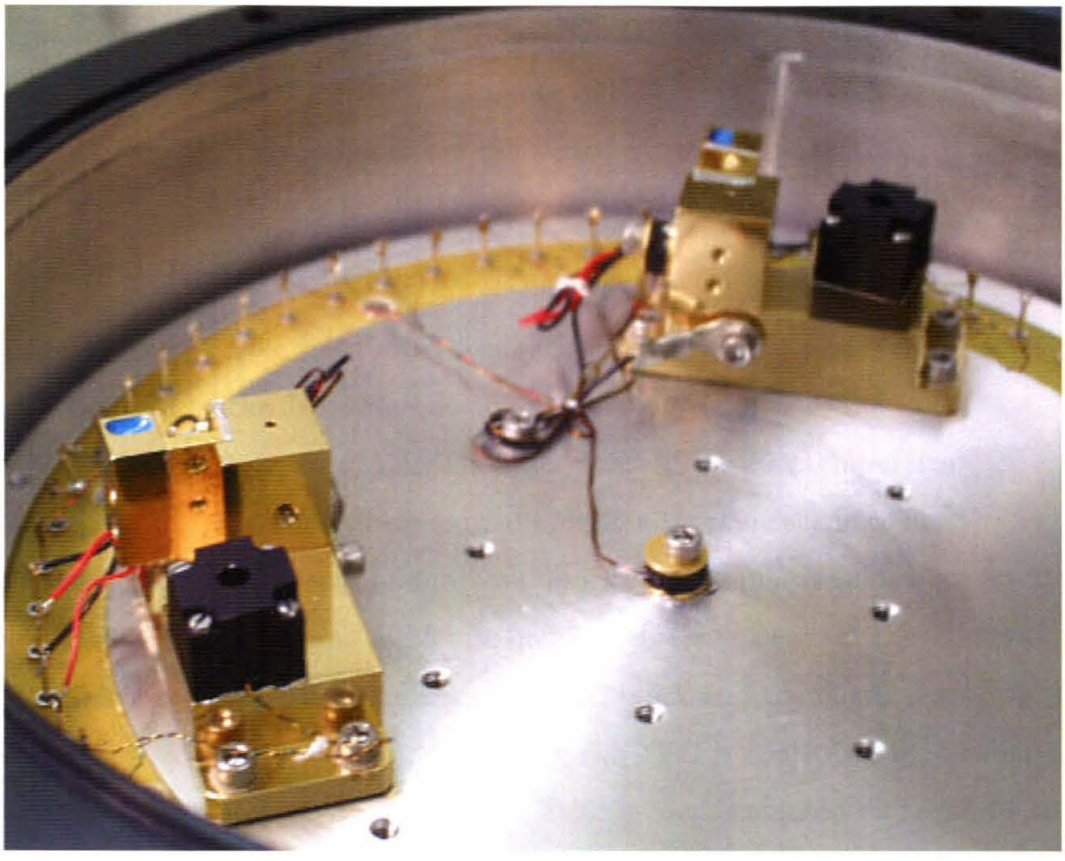

Figure 5.7: Lasers and detectors mounted in the dewar.

shield is also matte black anodized to minimize reflections, while the outer is gold-plated to decrease emissivity. dewar windows are ZnSe, 1.5" OD and 0.2" center thickness, with a 1 degree wedge and narrowband anti-reflection coatings to prevent fringing of laser power (II-VI Corp.). Windows are sealed with an aluminum flange and ethylene-propylene (EPR) O-rings. To reduce the distance between the lasers within the dewar and the collimating optics mounted outside, the windows are recessed into the dewar cover.

5.5.2 Optics Can

The optics can is a pressure-sealed aluminum container which mounts directly to the face of the dewar, and encloses all collimating and focusing lens assemblies, plus the NIR laser, detector, and thermal regulation system. The space constraints imposed by Centurion,

the original aircraft platform, mandated an extremely compact design, with this entire assembly no more than a few inches in height, and all components mounted on a surface only 7.5" in diameter. Figure 5.5 shows the arrangement within the optics can.

NIR laser and detector

The channel 1 source is a distributed feedback (DFB) indium phosphide diode laser at 1.37 μm developed by the JPL Microdevices Laboratory, similar to that used on the JPL-H_2O water vapor spectrometer (41). The laser operates CW at temperatures well above 200 K, allowing it to be temperature-regulated with a thermoelectric cooler (TEC) rather than a cryogen. A miniature aluminum "cold block" (1.1" square) holds both the laser, in a a standard 9 mm TO can, and a 1.5 mm diameter InGaAs detector (Fermionics). A 5.3 W TEC (Melcor) is sandwiched between this cold block and the dewar cover, which acts as the heat sink for the TEC. Current through the TEC is controlled by a subminiature proportional controller (Hytek) only 1.1" $\times$ 0.9" in size, mounted adjacent to the cold block.

Windows

Light in the three channels enters and exits the optics can through three wedged and AR-coated windows, again ZnSe for the mid-IR channels 2 and 3 and BK7 for the near-IR channel 1. As on the dewar cover, windows are sealed with flanges and EPR O-rings.

Lenses

Because the mid-infrared lasers used in WISP have low power and large divergences (up to 30 degrees emergence cone), and the lasers are necessarily removed from their collimating lenses by at least the thickness of the dewar cover, it is desirable that collimating lenses be as large as possible to maximize light collection. That is, it is desirable to have low f/D, or "f-number", where f is focal length and D is lens diameter. However, in the WISP design the need for compactness of the instrument constrained the allowable size of the

collimating and focusing lenses.

The Herriott cell mandates a specific opening angle for the entrance and exit beams of each channel passing through a single hole in the near Herriott cell mirror. This opening angle in turn determines the relative positions of laser and detector. The need to keep the The small opening angles (maximum 6°) and tight spacing (9" dewar-mirror) in the WISP instrument produce beam separations of only 0.7" (ch. 1) to 0.9" (ch. 3) at the positions of the lenses. Even this separation is only achieved by orienting the wedged windows of the optics can such that refraction further separates the input and output beams. For the mid-IR channels, this permits collimating and focusing lens diameters of only 0.375" and 0.5", respectively, with some room left for positional adjustment Lenses are ZnSe meniscus, narrowband AR-coated (II-VI Corp.). On WISP the dewar windows are recessed into the dewar cover to bring the lenses closer to the lasers and minimize the power lost: collimating lenses have focal length 0.8", or $f/2.1$. Light collection is not a problem for the dewar-cover-mounted channel 1, since here the collimating lens can be brought arbitrarily close to the laser. The channel 1 collimating lens is ∅ 0.25" (6.4 mm), with a focal length of only 4.5 mm, for an f-number of 0.7. (Ch. 1 focusing lens is $f/0.8$, with ∅ 0.39" (9.9 mm) and 8 mm focal length; both are AR-coated glass aspherics, New Focus).

Positioning for all lenses is accomplished via miniaturized commercial translation stages (Newport). In order to fit all components on the dewar cover, only channel 1 uses a relatively large 3-axis positioner, and channels 2 and 3 use smaller XY positioners with custom-designed lens barrels for the third axis. Each positioner is mounted on an angle plate machined to orient the lens perpendicular to the beam.

5.5.3 Multipass cell

Because absorption by scarce isotopomers of water is small, especially in the dry stratosphere, the instrument needs a long pathlength to obtain measurable signal. The practical constraints of an aircraft-mounted instrument mean that a long pathlength must be folded

into a small volume in a multipass cell. The WISP instrument uses a Herriott cell, an extremely stable multipass optical cavity consisting of two concave spherical mirrors. When light is injected into the cell at the appropriate off-axis angle it forms a circular spot pattern on mirrors as it passes back and forth (26, 2). If the mirror spacing and focal length are chosen appropriately, light returns out the hole from which it entered after the desired number of passes, at a beam angle that allows it to be directed on to a detector. The Herriott cell has the advantage that the position and angle of the exit beam is exceptionally robust to most distortions of the cell, a feature necessary for flight environments, where maintaining exact alignment is difficult. Although the spot pattern of beams within the cell warps and becomes elliptical as mirrors tilt or entrance beam angle deviates, the effect is minimum at the position of the entrance hole, so that beam position on the detector is far more stable. The one variable to which the cell is extremely sensitive is the relative mirror spacing; changes of less than a mm can cause the loss of all signal, or the shift to a configuration with a different number of passes. (See section 5.4 for a discussion of the related engineering issues.) However, the fact that the number of passes is acutely sensitive to mirror spacing, but the requisite input angle much less so, means that the same cell can conveniently be used for experiments at a variety of pathlengths without changing the foreoptics.

The WISP cell mirrors have a radius of curvature R=1.93294 m; the base WISP configuration is a 94 meter pathlength, with mirror spacing of 1.004 m apart (d/f of 1.0388, yielding 94 passes). The three channels are injected at different mirror radii and form three concentric spot patterns. Because the Herriott cell acts to continually refocus the beam near the center of the cavity, spot sizes remain constant. Figure 5.8 shows the modeled patterns on the WISP near mirror. The mirrors are 6" ∅, 5/8" thick, Zerodur substrates (Rocky Mountain Instruments) coated with silver plus a dielectric layer to protect from oxidation in the high-ozone environment of the lower stratosphere (Opticoat).

A high number of passes (n) in the Herriott cell is desirable since measured absorption is directly proportional to pathlength, but the n used is limited by mirror size, and also by

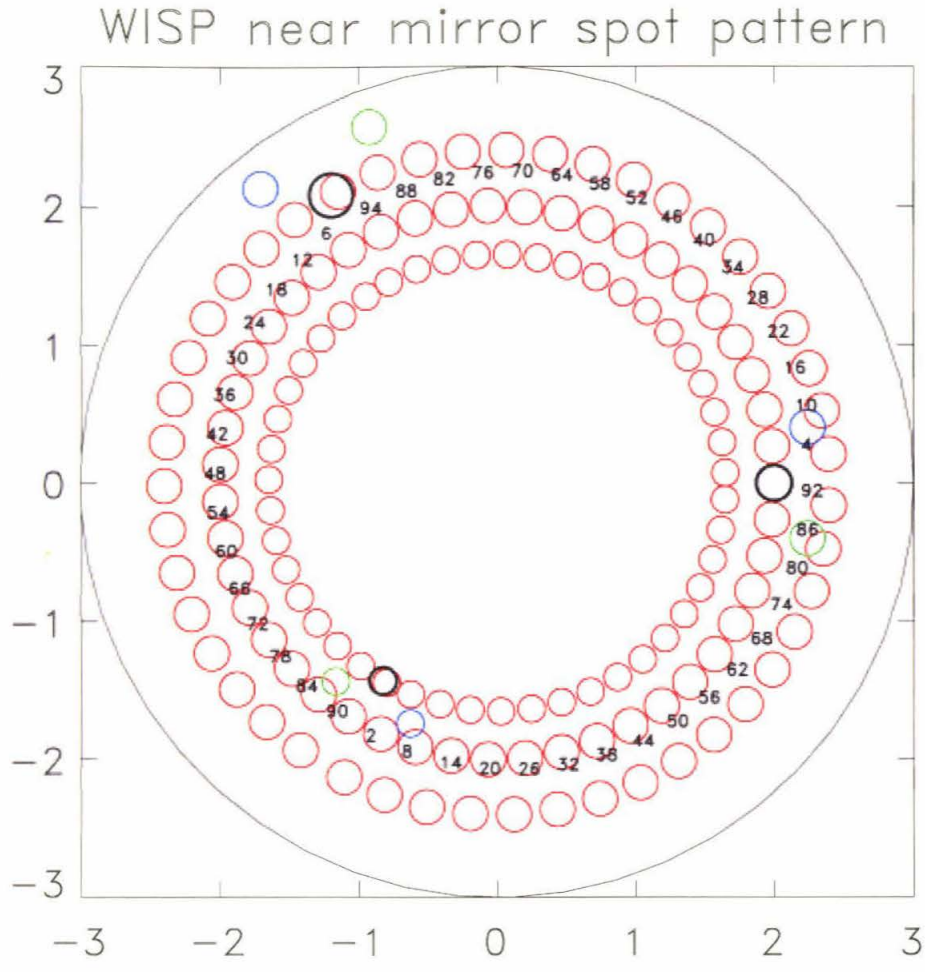

Figure 5.8: WISP Herriot cell spot pattern. The three WISP lasers are directed into the multipass cell so as to make concentric 92-pass patterns before exiting out their entrance holes. The near mirror is shown here, with the beam footprints in red. The spot pattern is approximately C3; i.e. the pattern has nearly 3-fold symmetry, and successive spots migrate $\approx 120^\circ$ around the mirror. The entrance holes are shown in black at their actual size and position; layout constraints on the dewar cover required that they be spaced 120° apart. Beam positions at the laser/detector plane for each channel are shown in blue and green. Note the off-center position of the exit beam through the entrance hole of the outer channel (3); this effect occurs because of the finite curvature of the mirror surface, which mandates slightly different Herriot cell solutions for channels at different radii. It is not possible to construct a cell perfectly aligned for all three channels. The configuration chosen here produces the minimum misalignment.

the increased sensitivity of the cell to misalignments at higher n. We chose 94 passes for WISP as the optimum tradeoff given the absorption strengths of the target spectral region. (Light losses on each reflection are less important; with mirror coatings of R $>$ 99%, total loss in the 94-pass Herriott cell is $<$ 61%, not enough to make photon limitation a source of noise). The WISP mirror diameter was then chosen as the smallest that could accommodate all three channels without 1) overlap of spots that would produce optical fringing or 2) bleeding of light from adjacent spots through the exit hole or 3) clipping of the spot pattern when mirror tilt or deviations in beam input angle warp the pattern into an ellipse. The near-IR beam (channel 1) occupies the innermost spot pattern, because its smaller divergence and closer collimating lens produce a smaller beam footprint on the mirror, allowing closer spot packing.

Although Herriott cells in general are relatively stable to distortion, some configurations are significantly more stable than others. Because WISP was to be used in an environment involving large mechanical stresses, it was important to choose the most robust configuration possible, and to determine the design tolerances for movement of its components. Herriott cell behavior in an undistorted case is typically modeled by approximating each reflection as passage through an infinitely thin lens (2). To conduct sensitivity studies, we constructed a three-dimensional ray-tracing model (described further in appendix B). The results from these studies drove the choice of d/f for WISP close to 1. In perfectly aligned system, we would prefer a higher d/f configuration, since higher d/f produces a greater opening angle between input and output beams, reducing most of the layout difficulties discussed above. However, the mispositioning of the exit beam produced by most mechanical distortions (mirror tilt, deviations in input angle, and changes in mirror separation) increases with d/f. In addition, at high d/f it is not possible to use three different channels at different pattern radii in the same Herriott cell. Model runs were used to determine a simple empirical relationship for the the correction to the mirror separation from the thin lens approximation required because of the finite curvature of the mirror (see Appendix B). The result is a function of spot pattern radius, meaning that a Herriott cell with multiple channels must necessarily be misaligned for all

but one of them. This misalignment produces an error in the position of the exit beam that increases with d/f, such that for WISP-sized mirrors, $d/f > 2$ would be unworkable.

5.6 Data Acquisition and Electronics

WISP uses the standard TDLAS technique of sweep integration and second-harmonic (2f) detection. Absorption spectra are generated by applying a sawtooth current ramp to the lasers, which scans the laser output wavelength across the spectral region of interest. An amplitude modulation (AM) scheme is used to improve SNR: the laser current is modulated by a sinusoidal waveform at a frequency much higher than that of the current ramp (50-80 kHz as opposed to 4 Hz), and the signal is detected by a lock-in amplifier at twice the modulation frequency. The demodulated signal represents the 2nd Fourier component of the absorption spectrum, and noise at other frequencies is rejected (figures 6.2). In this way the contributions of white noise on the laser current, optical interference at fringe spacings other than the spectral linewidth, and cross-talk between the channels (each channel has a different modulation frequency) are sharply reduced.

Laser control and data acquisition are handled by a single compact computer stack in PC-104 format, running under DOS and a C++ operating code. The stack consists of a commercial 80486 CPU board (Ampro Little Board), a custom-built analog board for laser current production and signal demodulation, a custom digital board for data acquisition, and a commercial A/D board (VersaLogic) that records engineering data from thermistors and accelerometers. Preamps for all three channels are mounted directly on the dewar, as close as possible to the detectors, to minimize noise pickup. The preamps incorporate an analog feedback "null circuit" that removes the slowly fluctuating detector offset caused by the thermal background. Laser current is turned off for a brief period before each sawtooth ramp, and the detector signal measured during this time is used the zero the preamp. The amplified signal is demodulated by a lock-in circuit on the analog board, and both demodulated and direct (dc) signals are recorded for each laser on each scan. The dc signal is used both to determine the returned power at the line position, needed in data

reduction, and to provide a clean absorption spectrum for reference when the modulation is periodically turned off. Although 2f detection is required for measurements in the dry stratosphere, HDO absorptions in parts of the upper troposphere can reach 1%, allowing detection by direct absorption. Comparison of the direct and 2f measurements at these altitudes is then used for calibration. The laser control and signal acquisition electronics are based closely on those used in the JPL-H_2O and ALIAS TDLAS instruments (76, 41)

Individual dc and 2f scans for each channel are recorded via fast direct memory access, with successive scans then averaged digitally to produce slower reported data. Because the WISP mid-IR lasers scan over a large spectral region (> 1 cm^{-1}) containing several absorption features, up to 5000 points/scan are recorded to obtain reasonable spectral resolution (figure 6.3). With three lasers on the instrument and a 4 Hz scan rate this yields a data input rate of > 240 Kbyte/s. The number of bytes recorded during an 8 hour flight far exceeds the capacity of affordable solid-state memory, so data is stored on a miniature laptop-PC format hard drive in a pressurized enclosure, as is required for operation at stratospheric altitudes. The hard drive box measures only $4.5'' \times 6.2''$, and contributes negligibly to the overall weight of the electronics.

A second electronics box handles thermal control and basic power conditioning. Temperature of various components of the instrument is regulated by sensorless controllers providing pulse-width modulated voltage to strip heaters (Minco). The entire instrument runs off aircraft 28V power, converted to the relevant voltages by low-noise dc-dc converters (Vicor). Because both these functions can be a source of noise to the signal electronics, they are kept in a separate enclosure. The combination of computer and power/thermal boxes is a package $12 \times 9 \times 10''$ in size and 20 pounds in weight that fits within the WB57 wing, mounted on a removable hatch cover. Instrument control is by a single relay switch from the airplane cockpit (figure 5.9).

Figure 5.9: WISP electronics during WB57 power check. The electronics box on the cart contains all power conditioning, laser current supply, 2f demodulation, heater controls, and data acquisition and storage functions for the instrument. The box mounts within the wing, through the open hatch cover. The monitor is used for pre-flight testing only. The exposed cable provides power and switching from the aircraft.

Chapter 6

WISP Expected Sensitivity

6.1 Introduction

The measurement of water vapor isotopic composition by TDLAS is difficult because the isotopomers of water - in particular HDO, the species of primary scientific interest - are scarce in the dry upper troposphere and lower stratosphere. The mixing ratio of water vapor in the stratosphere is on the order of 5 ppm, and the ratio $[HDO]/[H_2O]$ in Standard Mean Ocean Water is 3×10^{-4}. Even in the absence of isotopic depletion during ascent to the stratosphere, HDO would be present at ppb levels. Remote sensing observations show that stratospheric HDO is in fact depleted by nearly 70%, bringing it to sub-ppb levels (see chapter 2), approaching the detection threshold of absorption spectroscopy techniques for most atmospheric molecules. This abundance limitation determines the upper altitude cutoff for feasible TDLAS measurements of HDO. Measurement precision is greater at lower altitudes, where the atmosphere is significantly wetter.

An open-path instrument like WISP, with no ability to modify the pressure of the gas measured, also has a lower altitude cutoff imposed by pressure-broadening of the target spectral lines. Although HDO remains scarce enough through the middle troposphere that the absorption signal does not saturate, pressure-broadening blends adjacent lines and makes measurement difficult below a certain altitude. For the target spectral range

chosen for WISP, we estimate the lower cutoff is $\approx$ 300 mb (see figure 6.2).

Measurement by TDLAS methods cannot produce the high accuracy of laboratory mass spectrometry (with measurements typically to ± 0.1 ‰ or .01% deviation from standards). In the dry upper troposphere / lower stratosphere region (UT/LS), where HDO abundance is the limiting factor, TDLAS instrument error will reach tens of ‰ relative to SMOW. However, the scientific problems addressed by water vapor isotopes do not require stringent accuracy. The scenarios for stratosphere-troposphere exchange shown in figure 5.1 produce differences in δD of several hundred ‰ in the uppermost troposphere and lower stratosphere. The projected error for WISP measurements of the various isotopomers of water vapor over the UT/LS region are shown in table 6.1. Precision degrades with altitude for the isotopomers as their abundance becomes low enough that SNR is limiting. We assume a 5% accuracy for individual gas measurements, typical for the TDLAS instruments that WISP closely resembles (76, 41). The accuracy for isotopic ratios is assumed to be improved over that for individual species. Even when gas abundance is not limiting, TDLAS instruments similar to WISP show an $\approx$ 1% baseline precision due to electronic and thermal fluctuations (76, 41). In the dry UT/LS, instrument sensitivity also becomes a factor in measurements of scarce water isotopomers. Total precision is then taken as the root sum square of the baseline precision and the predicted instrument SNR. Expected SNR is determined from the calculated linecenter absorption of the target spectral lines, assuming an atmospheric profile of the species to be measured, and an assumed noise threshold for the instrument. The calculation of SNR is discussed further in sections 6.2.1 and 6.4.1, and the change in expected SNR with altitude is shown in Figure 6.4. The range of errors in table 6.1 above reflects the range of expected instrument SNR in the UT/LS region. Accuracy/precision issues are discussed further in section 6.2.2.

We view the predicted instrument performance as sufficient for the science in question. Although error is greater for δD than for δ^{18}O and δ^{17}O, the latter are less useful for discriminating between scenarios of water vapor transport, because the fractionation of the oxygen isotopomers is much lower than for HDO. (The maximum expected change

Species	Accuracy	Precision	Total
HDO	5%	1.5-15%	(3.5-14%)
δD	3%		10-45 ‰
$H_2{}^{18}O$	5%	1.5-2%	(3-3.5%)
$\delta^{18}O$	3%		25-30 ‰
$H_2{}^{17}O$	5%	1.5-8%	(3-8.5%)
$\delta^{17}O$	3%		30-80 ‰
$H_2{}^{16}O$	5%	1%	5%
CH_4	5%	1%	5%

Table 6.1: Expected accuracy and precision for the different species measured by WISP. The total error for the isotopomers is given as error when species are ratioed (in parentheses), i.e. using the lower accuracy figure. The ‰ error in the δs is computed assuming stratospheric compositions of $\delta D = -670‰$, $\delta^{18}O = -100‰$, and $\delta^{17}O = -50‰$.

in $\delta^{18}O$ is of order 100 ‰). However, oxygen isotope measurements with the projected level of accuracy are still useful as a diagnostic of supersaturation-induced kinetic effects, which can produce positive enrichment in oxygen isotopic composition. The remainder of this chapter discusses how those projections were determined.

6.2 TDLAS instrument performance

6.2.1 Sensitivity

The projection of WISP sensitivity draws on results from existing TDL absorption spectrometry instruments. The sensitivity of absorption spectroscopy instruments is typically described in terms of the noise-equivalent absorption, (the absorption that would produce a signal of the magnitude of the 1σ noise level). TDLAS instruments typically report laboratory sensitivities of a few $\times 10^{-5}$ for instruments with 50-100 m pathlengths, or $\approx 4 \times 10^{-10}$ cm^{-1}Hz$^{-1/2}$ (76, 41). The latter value is the per-point instrument sensitivity

with a 1 s averaging time, here with the assumption of 3s scans of 1024 points. These units are a standard means of describing the sensitivity of absorption spectroscopy techniques, but are not necessarily the most relevant for TDLAS instruments, where the limiting factor is usually not Gaussian noise but semi-stationary etalons. In this case longer integration times do not necessarily improve instrument precision. We assume that WISP would achieve a similar noise threshold.

In the mid-infrared, the region of the strongest rotational-vibrational absorption bands, typical atmospheric species have peak integrated linestrengths on the order of $S_{296K} = 10^{-19}$ cm/molec. Over a hundred meter pathlength at stratospheric pressure and temperature, this produces absorptions of $\approx 5^{-4}$/ppb. It is clear that measurement of HDO, at sub-ppb in lower stratosphere, approaches the sensitivity limits of the TDLAS technique, with signal-to-noise ratio (SNR) likely < 10 in the stratosphere. Obtaining reasonable signals requires careful choice of strong absorption lines. Successful measurement also requires attention to several other issues that can reduce sensitivity. Noise in the current supply, for example, translates into jitter of the laser frequency, and so increases the apparent laser linewidth. If laser linewidth is comparable to the width of the target absorption line then the spectral contrast and so sensitivity are reduced. For typical laser current tuning rates of .03 cm^{-1}/mA and spectral lines of .007 cm^{-1} (200 MHz) at 100 mb, noise on the laser current must be kept below 0.2 mA on a current ramp of order 100 mA in order for the effective linestrength to be unaffected. The projected sensitivities in table 6.1 assume baseline noise of 2×10^{-5} in 100 m., typical of TDLAS instruments, absorption linestrengths for the target lines discussed below (see section 6.3), and no signal attenuation due to current noise.

6.2.2 Accuracy / precision

Typical reported accuracies for TDLAS instruments are $\approx 5\%$. [1] As in any instrument, accuracy problems can be caused by instability in the electronics. For instruments with

[1] "Accuracy" here is used to refer to systematic error that is approximately constant for the duration of an eight-hour aircraft flight, and "precision" to scatter within data taken on a given flight.

open-path arrangements, where T and p in the measured gas vary widely, uncertainties in spectral line parameters can also be important, as are uncertainties in T and p themselves. The second harmonic detection technique used by many TDLAS instruments imposes additional difficulties. Second-harmonic (2f) detection increases signal gain and so sensitivity, necessary for small absorptions, at the cost of introducing additional variables into the calibration. The 2f signal is a function both of modulation frequency and of laser power at the line position, which must be separately monitored and used in the data reduction. Both of these factors can introduce systematic error into the measurement of a single gas. For water vapor, and especially for water vapor isotopic composition, it is prohibitively difficult to construct a reliable standard for in-flight calibration to compensate for potential drifts. The WISP open-path arrangement also means that any calibration standard would have to be measured in a separate optical cell, making it of doubtful utility.

Measurements of an isotopic ratio by TDLAS can however be intrinsically more accurate than the numbers quoted above, if errors in the two species are correlated. If the two ratioed species can be obtained in the same scan, or at minimum with the same laser and detector in successive scans, then errors associated with fluctuations in both amplifier gain and modulation frequency will cancel to some extent. Errors due to inaccurate measurement of T or p may also cancel if line spectral parameters are similar. For this reason the measurement of a ratio can be more accurate than measurements of individual gases. In table 6.1 we assume an accuracy for the ratioed quantities of 3% and a precision unrelated to SNR of 1%. SNR limitations become increasingly important at higher altitudes.

6.3 Target spectral region

Obtaining the best possible measurement of water vapor isotopomers requires careful choice of the target spectral region. To take advantage of error-compensation in the ratio measurement it is desirable to capture absorption lines of water and its isotopomers in

a single laser scan. Because the oxygen isotopomers of water vapor are also of interest, and methane is a useful in-flight calibrator in the troposphere, the ideal spectral region would contain lines of H_2O, HDO, $H_2{}^{17}O$, $H_2{}^{18}O$, and CH_4 within 1.5 cm^{-1}, a typical single-mode tuning range for a lead-salt diode laser. Absorptions by all species should be comparable, and the HDO absorption line must be among the strongest accessible. The spectral region must be free of interferences from other atmospheric gases, including water vapor itself: the wings of strong water lines can swamp the tiny absorptions produced by HDO. Finally, the lines should have low ground state energies so that their intensities are not overly temperature-sensitive; it is difficult to measure ambient temperature in an open-path system to better than a degree K.

6.3.1 Water vapor spectra

As a non-linear triatomic molecule, water vapor has three fundamental vibrational modes, corresponding to the bend (ν_2) and the symmetric and asymmetric stretches of the H_2O molecule (ν_1 and ν_3, at almost identical frequencies). The rotational-vibrational IR spectrum of water has three bands corresponding to these modes, with two nearly superimposed. Because water is a light molecule, the fundamental vibrations fall at relatively high frequencies in the mid-infrared and the rotational transitions are well-spaced, making it readily accessible to absorption spectroscopy techniques. The overtone and combination bands in the near-infrared are significantly weaker than the fundamental bands, making them a poor choice for measurements where sensitivity is critical. Isotopic substitution introduces shifts in absorption line positions because of changes in the vibrational frequencies and rotational constants; the shift in bandcenter position is greater for substitution of hydrogen than of oxygen atoms because of the larger percentage change in mass. This separation allows spectroscopic measurement of the different isotopomers. Figure 6.1 shows the absorption spectra of H_2O and HDO throughout the infrared region, with the HDO absorptions scaled by its relative abundance to facilitate comparison. Substitution of a deuterium atom shifts the ν_2 bandcenter by 200 cm-1 and ν_3 by more than 1000 cm^{-1},

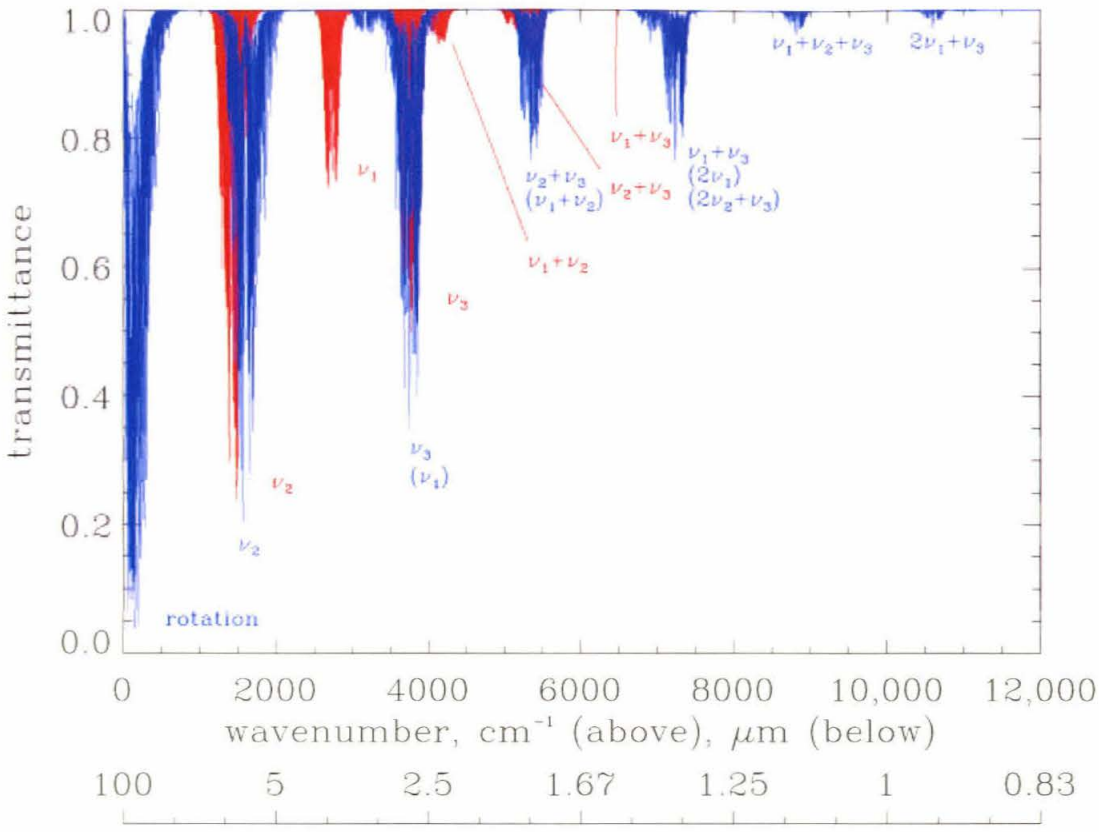

Figure 6.1: Infrared spectra of H_2O (blue) and HDO (red). The absorption spectra here were calculated using the Modtran program for mean atmospheric conditions at 300 mb, with a 100 m pathlength. For comparison, HDO absorption is scaled so that the ν_3 band matches that for H_2O; actual absorption by HDO is a factor of 10^4 smaller. The apparent difference in the overtone bands between H_2O and HDO is due to this scaling. The near-saturation of the water vapor fundamental bands means that the ratio of fundamental to overtone absorptions is less than the ratio of their respective linestrengths. No absorption is shown at the HDO $\nu_1 + \nu_3$ or higher combination bands because of the lack of line information in the HITRAN line compilation (64, 65).

so that ν_1 and ν_3 are now well-separated, corresponding to the O-H and O-D stretches, respectively.

6.3.2 Choice of spectral region

The target spectral region for TDLAS measurements of HDO is limited to the mid-IR fundamental rotational-vibrational bands: the overtone bands are too weak, and laser sources in the far-IR region are problematic. Of these, the ν_3 band at 3700 cm^{-1} (2.7 μm) is unusable because of interferences from the (10^01) overtone of CO_2 and the ν_3 of $H_2{}^{16}O$, both of which sit directly over the HDO band. Use of the ν_1 over the ν_2 region would seem preferable, both because detector technology is better there - InSb detectors at 2.7 μm region are preferable to the HgCdTe detectors used at longer wavelengths - and because interferences are less. However, the isotopic separation at ν_1 is so great that it hinders isotopic ratio measurements: there is no possibility of accessing both HDO at ν_1 and $H_2{}^{16}O$ with a single lead-salt diode laser. Accuracy considerations make it strongly preferable to make both measurements with the same laser and detector. Careful searching of the published linelist for the ν_2 region produces several candidate HDO lines free of interferences, and one spectral region containing well-spaced lines of HDO, $H_2{}^{17}O$, $H_2{}^{18}O$, and CH_4 within a narrow 1.5 cm^{-1} interval from 1483.7 to 1485.2 cm^{-1} (64, 65). This is the target region chosen for the WISP instrument. Figures 6.2 and 6.3 show synthetic and laboratory spectra, and line parameters are listed in table 6.2. The laboratory measurements confirm the published line positions.

There is little sacrifice of sensitivity for the benefit of obtaining multiple measurements in a single scan: the 1484.1 cm^{-1} HDO linestrength is two-thirds that of the strongest line clear of interferences. The weak water line at 1495.1 cm^{-1} is not useful for obtaining isotopic ratios because of its strong temperature dependence (see section 6.4.2). Obtaining an accurate isotopic ratio requires "jump-scanning" the laser to another spectral region to acquire a stable $H_2{}^{16}O$ measurement. The abundance of water lines in the vicinity provides a large number of candidates.

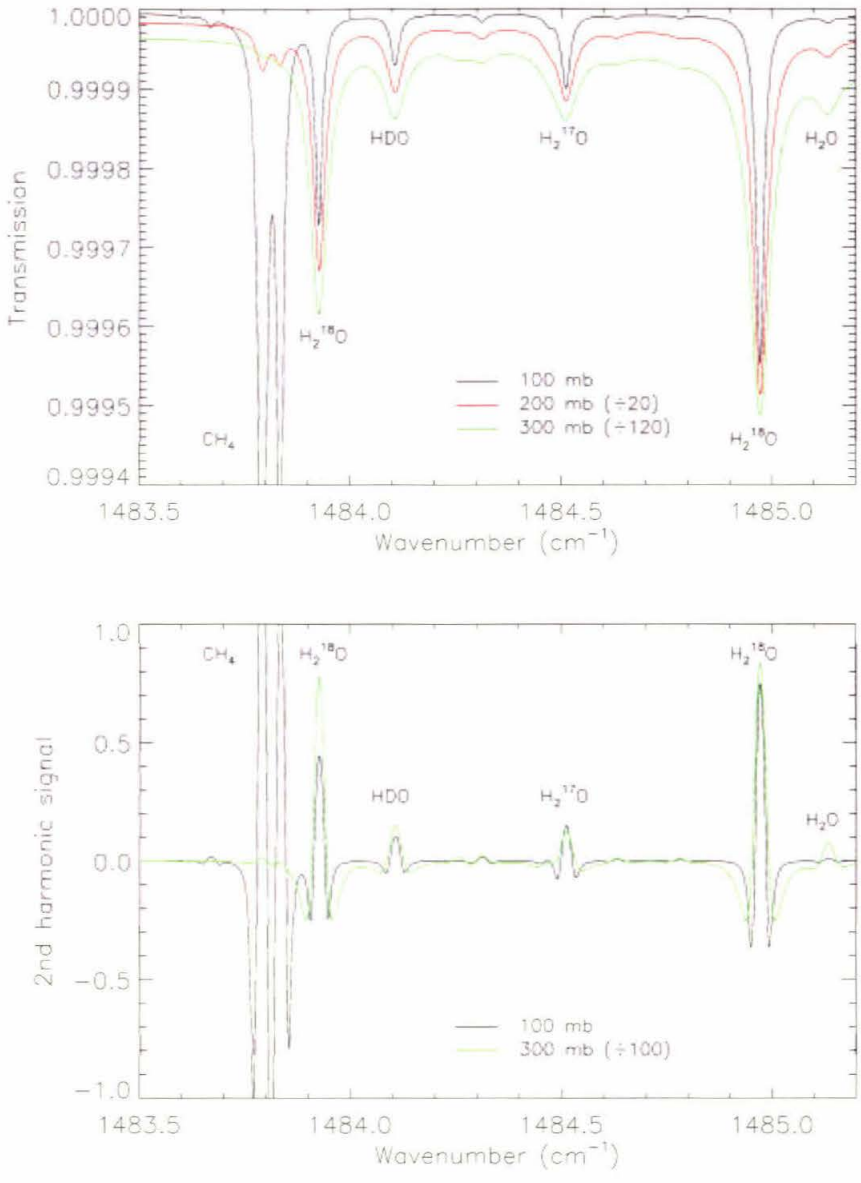

Figure 6.2: Synthetic spectrum of the WISP target region, showing line broadening with increasing pressure. The top panel shows absorption in a 100 m pathlength, with temperature as in a standard tropical atmosphere, water vapor at 5 ppm at 100 mb and 50% RH in the troposphere, and δD varying from -250 to -670 ‰ with altitude. The bottom panel shows the same data as it would appear in second-harmonic detection; again, the higher-pressure spectra are scaled to facilitate comparison. This scaling makes the CH_4 lines at 1483.8 less apparent at higher p, because CH_4 is relatively constant while water increases by two orders of magnitude. The T-sensitive $H_2{}^{16}O$ line at 1484.1, on the other hand, is apparent at 300 mb but vanishes at the cold tropopause.

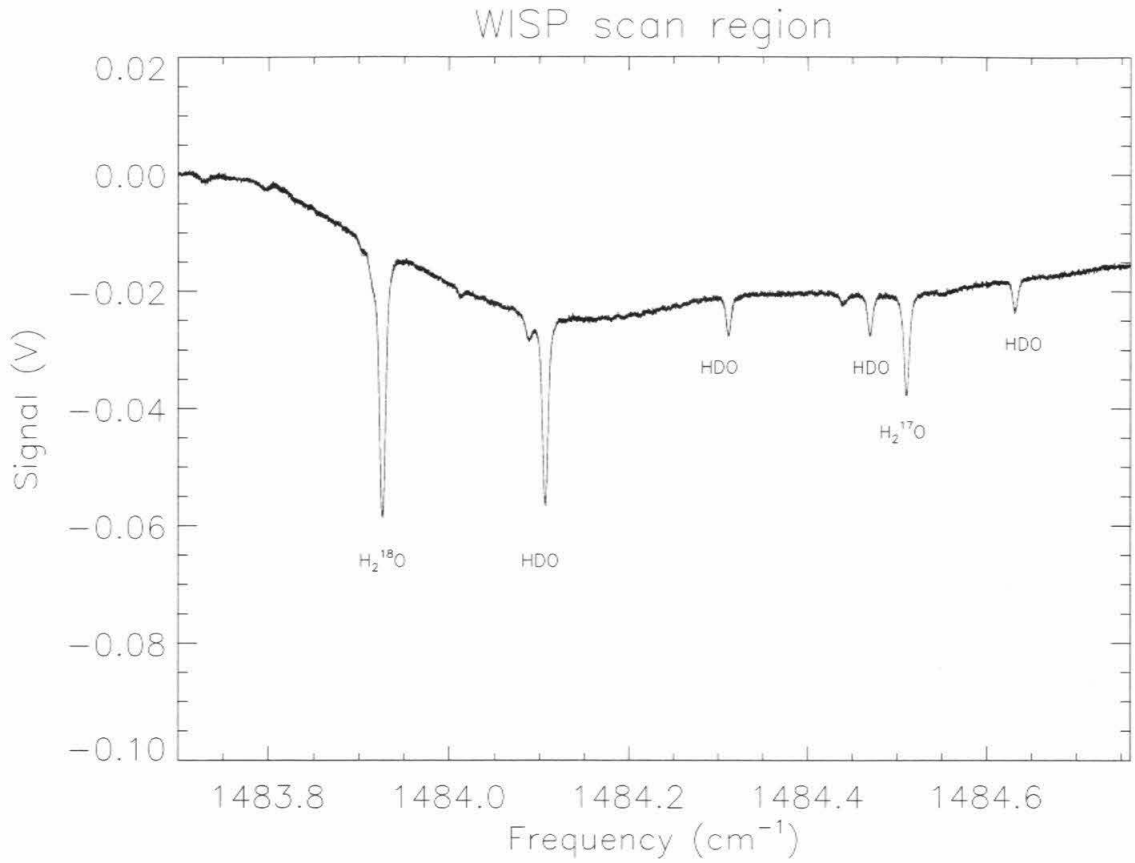

Figure 6.3: The target spectral region. The spectrum was obtained with the WISP optical head and a reference cell containing isotopically enriched water vapor. [HDO]/[H_2O] in the sample is ≈ 0.1. The relative enrichments in $H_2{}^{18}O$ and $H_2{}^{17}O$ are somewhat smaller than that in HDO, making the HDO lines appear disproportionately strong. The triplet of weak HDO lines apparent in this scan are in fact too weak to be measurable in atmospheric spectra. The undulating background signal is an etalon produced by the uncoated cell windows. The wavelength scale was calibrated using a Ge etalon, with the 1484.1 cm^{-1} HDO line as the reference frequency.

Species	$\nu(\mathrm{cm}^{-1})$	S (296 K)	$\tilde{\nu}_m(\mathrm{cm}^{-1})$	$\gamma_l^0(\mathrm{cm}^{-1})$
$H_2{}^{18}O$ (a)	1483.93	4.1×10^{-20}	550	.075
HDO	1484.11	8.1×10^{-20}	226	.092
$H_2{}^{17}O$	1484.51	4.8×10^{-20}	205	.098
$H_2{}^{18}O$ (b)	1484.97	4.9×10^{-20}	325	.086
$H_2{}^{16}O$	1485.13	6.4×10^{-23}	1907	.088

Table 6.2: Line parameters for the WISP target region, from the HITRAN compilation (64, 65). Columns show, from left to right, linecenter, integrated linestrength, ground state energy, and foreign-broadening coefficient. Linestrengths are given per molecule, rather than scaled for an assumed isotopic composition, as they are in HITRAN. The SMOW standard ratios for $HDO/H_2{}^{16}O$, $H_2{}^{17}O/H_2{}^{16}O$, and $H_2{}^{18}O/H_2{}^{16}O$ are 3.1×10^{-4}, 3.7×10^{-4}, and 2.0×10^{-3}, respectively.

6.4 Expected instrument performance

6.4.1 Sensitivity

The expected WISP sensitivity for measurements of the water vapor isotopomers exceeds SNR=10 throughout the troposphere and lower stratosphere (figure 6.4). Instrument sensitivity was calculated by assuming the water vapor profile of a standard tropical atmosphere and calculating linecenter absorption for the WISP target lines using HITRAN line parameters listed above. δD was assumed to vary linearly from oceanic to stratospheric values. The worst-case instrument error listed in table 6.1 for HDO is the case where linecenter absorption is only 10× the baseline noise; the SNR 10 position here is shown as a dashed line. The intersection of this line with the HDO profile marks the upper altitude limit for the instrument - above this point, error increases to the point where the relevant science is compromised. The line blending apparent at 300 mb in the synthetic spectra (see figure 6.2) leads us to consider this pressure level as the approximate lower limit for WISP measurements.

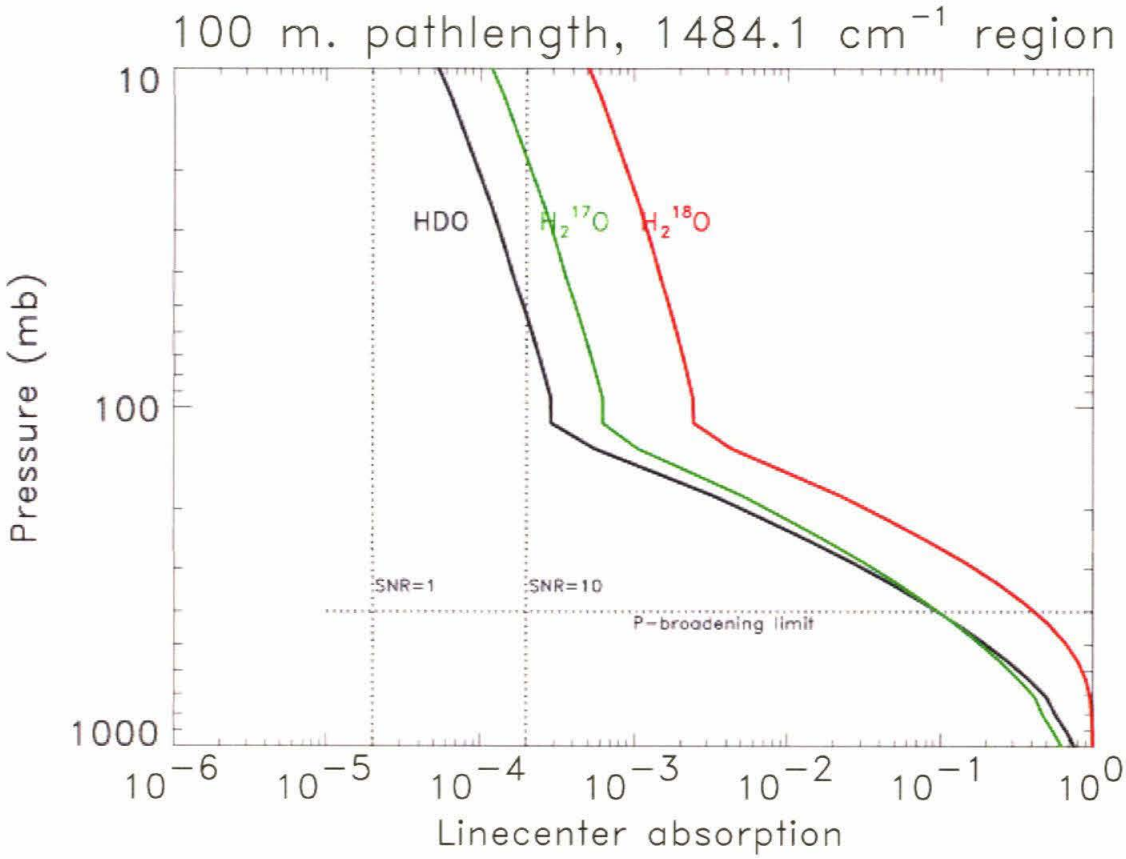

Figure 6.4: Linecenter absorption for water isotopomers in the WISP target spectral region. T,p, and water profiles are taken from a standard tropical atmosphere. Linecenter absorptions are computed assuming no fractionation for the oxygen isotopes, and a linear decline in δD through the troposphere to mean stratospheric values. The dashed horizontal line marks the lower altitude limit for WISP measurements; the upper limit for each species is given by the intersection of the SNR=10 linewith the each absorption profile. WISP baseline noise is assumed to be 2×10^{-5}.

6.4.2 Temperature and pressure uncertainties

Uncertainties in the temperature and pressure of the air within the multipass cell are a significant source of error for TDLAS measurements. Maintaining and measuring a uniform T and p throughout a cell is difficult even with an enclosed and thermally regulated system; in an open-path system on a moving aircraft the measurement of T and p is still more difficult, because T and p readings must be calibrated to remove ram pressure effects. We would expect that pressure measurements within the WISP cell can be made to 0.5% accuracy and temperature to 1° K. Minimizing the temperature sensitivity of the measurements by choosing spectral lines appropriately is vital for measurement accuracy. In addition to the uncertainties introduced by errors in T and p, the large range in T and p experienced by the air sampled mandates a thorough understanding of the response of linestrengths and lineshapes to changes in T and p. As no in-flight calibration is used, error in the assumed line parameters propagates directly into error in the measurement. Careful laboratory calibration over the full range of T and p is necessary to validate or correct published line parameters.

Conversion from molecules to mixing ratio

The absorption spectrometer provides a measurement of absolute abundance of molecules of the target gas in the optical cell, but the relevant quantity of interest for science is the mixing ratio of that gas (χ). Ambient temperature and pressure enter directly into the conversion from number density to mixing ratio. The accuracy of measurement of mixing ratio is then directly affected by errors in T and p, independent of any effect on the absorption lines themselves.

$$\frac{\sigma_\chi}{\chi} = \left(\left(\frac{\sigma_\mathrm{p}}{\mathrm{p}} \right)^2 + \left(\frac{\sigma_\mathrm{T}}{\mathrm{T}} \right)^2 \right)^{\frac{1}{2}} \tag{6.1}$$

Errors of $\sigma_\mathrm{T} = 1\mathrm{K}$ out of 200K and $\sigma_\mathrm{p} = 0.5$ mb out of 100 mb produce an unavoidable 0.7% measurement uncertainty. This is included in the total accuracy estimation of table 6.1.

Effect on spectral linestrengths and shapes

Temperature and pressure also affect line intensities and lineshapes, and so uncertainties in T and p can introduce error into the interpretation of measured absorption lines. Integrated line intensity is a function of temperature both because the population in the lower state of the transition is governed by the Boltzman distribution, and because rotational and vibrational partition functions are temperature-dependent. The temperature dependence is then given by

$$S \propto (T/To)^n \times \exp\left(-\mathrm{hc}\tilde{\nu}_\mathrm{m}/\mathrm{kT}\right) \tag{6.2}$$

where, for a non-linear molecule, $n = 3/2$. Absorption lines whose ground state is high-energy ($\tilde{\nu}_\mathrm{m}$ is large) are strongly affected by temperature, since their strength depends on the population in the tail of the Boltzman distribution (figure 6.5). The $H_2{}^{16}O$ line at 1485.1 cm^{-1} with $\tilde{\nu}_\mathrm{m} = 1900$, for example, has a linestrength that is temperature dependent by 6%/oK, an unacceptably large source of measurement error. To minimize error it is crucial to choose low $\tilde{\nu}_\mathrm{m}$ lines. This makes measurement of $H_2{}^{16}O$ somewhat problematic, since most intrinsically weak lines (the $H_2{}^{16}O$ absorption must be comparable in strength to that of HDO despite the fact that $H_2{}^{16}O$ is more abundant by a factor of 10^4) are derived from "hot bands". Nevertheless, there are sufficient candidates within the range of a lead-salt laser that this is not a major measurement obstacle. The ground state energies of the water isotopomer lines in WISP target region are nearly optimal at 200-325 cm^{-1}, yielding T-dependence of $0.03 - 0.3\%/\,\mathrm{o\,K}$. Temperature uncertainty is not a significant factor for the strength of the target absorption lines.

Temperature and pressure uncertainties are more important for their effect on lineshapes. In the troposphere, linewidths are determined largely by collisional broadening, producing Lorentzian shapes with widths governed by:

$$\gamma_\mathrm{l} \propto \mathrm{p} \times \mathrm{T}^{-n}, \tag{6.3}$$

where n is on the order of 0.6 for the target lines. At higher altitudes, in the tropopause region, the pressure-broadening declines to the same magnitude as Doppler broadening

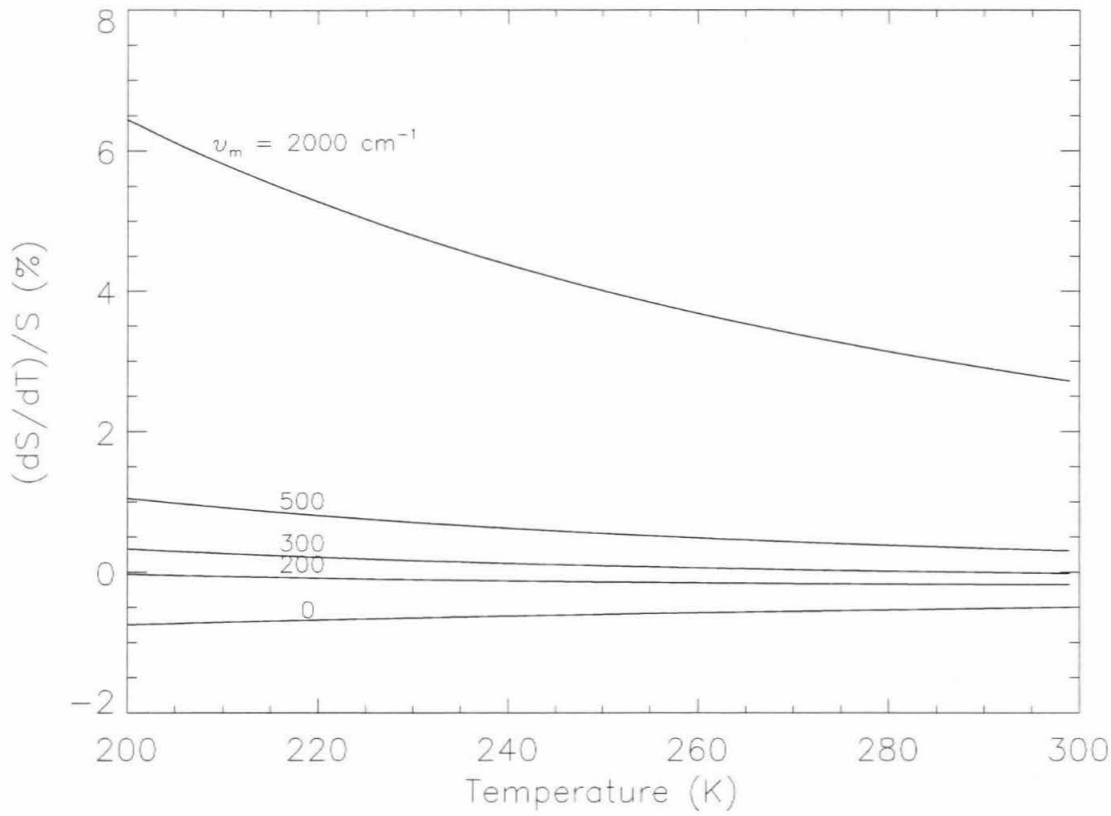

Figure 6.5: Temperature dependence of integrated line intensity for a non-linear molecule. The ordinate is the fractional change in S that results from a 1K temperature change. Temperature dependences grow stronger as T decreases. Note that the lowest possible ground state energy does not lead to the minimal temperature sensitivity: $\tilde{\nu}_{\mathrm{m}} = 0$ yields a 1/T dependence from the partition function term.

with:

$$\gamma_{\mathrm{d}} \propto \mathrm{T}^{\frac{1}{2}}, \tag{6.4}$$

and the resulting lineshape can be approximated by a Voigt function. Although in principle the measured lineshape can be fit to determine temperature and and pressure self-consistently, in practice this is generally not possible to significantly better than the uncertainties in the T and p measurements. Fitting to determine T and p is especially difficult for the second harmonic signal, where the modulation frequency is an additional

variable. The exact measurement error introduced by inaccuracies in assumed lineshape will depend on the fitting routine used in data analysis and is best determined numerically. Simplistic analysis as in section 6.4.2 gives a maximum error is 0.6% in the direct absorption signal. It is worth noting, however, that spectroscopic studies suggest that the larger contribution to linewidth-related error is uncertainty in n itself (the temperature dependence of the pressure broadening coefficient), which requires extensive calibration (41).

Second-harmonic detection

Error analysis for the second-harmonic signal is more complicated; the amplitude of the 2f signal, as well as its shape, are a function of the absorption line shape. The increased gain of second-harmonic detection is dependent on choice of appropriate modulation frequency: the optimal gain occurs for modulation of amplitude approximately twice the linewidth. Changes in linewidth therefore strongly affect the 2f signal, and errors in assumed linewidth propagate into the measurement. Again, fitting of the 2f signal to determine T and p is possible in theory, although it can be difficult in practice. The effects of T and p uncertainties are minimal, however, at the region for which modulation is optimized: in the case of a weak absorber such as HDO, the lower stratosphere, where signals are weakest and gain is needed. Numerical studies show that even when no fit is attempted and only the amplitude of the 2f signal is considered, error induced at 300 mb is under a percent. These effects are factored into the error estimates of table 6.1.

6.4.3 Conclusion

Sensitivity analysis indicate that WISP should produce scientifically useful measurements of water vapor isotopomers throughout the upper troposphere and up to the lowermost stratosphere. Although instrument errors are larger than those for laboratory mass spectrometry, the science requirements are sufficiently loose that data from the instrument can be effectively used to address questions of water vapor transport. To date there have

been no viable means of obtaining measurements of water vapor isotopic composition in this altitude region that can be used to address these issues. *In-situ* measurements by TDLAS instruments such as WISP have great potential for increasing our understanding of the controls on tropospheric humidity and the transport of air between troposphere and stratosphere.

Bibliography

[1] M.M Abbas et al. Seasonal variations of water vapor in the lower stratosphere inferred from ATMOS/ATLAS-3 measurements of H_2O and CH_4. *Geophys. Res. Lett.*, 23, 1996.

[2] J. Altmann, R. Baumgart, and C. Weitkamp. Two-mirror multipass absorption cell. *Appl. Optics*, 20:995–999, 1981.

[3] J.G. Anderson, W.H. Brune, and M.H. Proffitt. Ozone destruction by chlorine radicals within the antarctic vortex - the spatial and temporal evolution of ClO-O_3 based on *in situ* ER-2 data. *J. Geo. Res.*, 94:11465–11479, 1989.

[4] A.E. Andrews, K.C. Boering, B.C. Daube, S.C. Wofsy, et al. Empirical age spectra for the lower tropical stratosphere from in situ observations of CO_2: implications for stratospheric transport. *J. Geo. Res.*, 104:26581–26595, 1999.

[5] World Meteorological Association. Scientific assessment of ozone depletion: 1994. Technical Report 37, WMO global ozone research and monitoring project, Geneva, 1995.

[6] M.G. Balluch and P.H. Haynes. Quantification of lower stratospheric mixing processes using aircraft data. *J. Geo. Res.*, 102:23487–23504, 1997.

[7] K.A. Boering, E.J. Hintsa, S.C. Wofsy, J.G. Anderson, et al. Measurements of stratospheric carbon dioxide and water vapor at northern midlatitudes: implications for troposphere-to-stratosphere transport. *Geophys. Res. Lett.*, 22:2737–2740, 1995.

[8] K.A. Boering, S.C. Wofsy, B.C. Daube, et al. Stratospheric mean ages and transport rates from observations of carbon dioxide and nitrous oxide. *Science*, 274:1340–1343, 1996.

[9] A.W. Brewer. Evidence for a world circulation provided by the measurement of helium and water vapor distribution in the stratosphere. *Q. J. R. Meteo. Soc.*, 75:351–363, 1949.

[10] B. Carli and J. Park. Simultaneous measurement of minor stratospheric constituents with emission far-infrared spectroscopy. *J. Geo. Res.*, 93:33851, 1988.

[11] J.G. Charney and P.G. Drazin. Propagation of planetary-scale disturbances from the lower into the upper stratosphere. *J. Geo. Res.*, 66:83–109, 1961.

[12] P. Chen, J.R. Holton, A. O'Neill, and R. Swinbank. Isentropic mass exchange between the tropics and extratropics in the stratosphere. *J. Atmos. Sci.*, 51:3006–3018, 1994.

[13] E.F. Danielsen. A dehydration mechanism for the stratosphere. *Geophys. Res. Lett.*, 9:605, 1982.

[14] E.F. Danielsen. In situ evidence of rapid, vertical, irreversible transport of lower tropospheric air into the lower tropical stratosphere by convective cloud turrets and by larger-scale upwelling in tropical cyclones. *J. Geo. Res.*, 98:8665–8681, 1993.

[15] W.B. DeMore et al. Chemical kinetics and photochemical data for use in stratospheric modeling, evaluation number 12. Technical report, JPL, 1997.

[16] B.M. Dinelli et al. Measurement of stratosopheric distributions of $H_2^{16}O$, $H_2^{17}O$, $H_2^{18}O$, and $HD^{16}O$ from far-infrared spectra. *J. Geo. Res.*, 96:7509, 1991.

[17] D.H. Ehhalt. Methane in the atmosphere. In D.H. Woodwell and E.V Pecan, editors, *Carbon and the Biosphere*, 1973.

[18] D.H. Ehhalt. Vertical profiles of HTO, HDO, and H_2O in the troposphere. Technical report, Natl. Cent. for Atmos. Res., 1974.

[19] J.W. Elkins, D.W. Fahey, J.M. Gilligan, et al. Airborne gas chromatograph for in situ measurements of long-lived species in the upper troposphere and lower stratosphere. *Geophys. Res. Lett.*, 23:347–350, 1996.

[20] A.R. Frederick, J.E. ann Douglass. Atmospheric temperatures near the tropical tropopause: temporal variations, zonal asymmetry, and implications for stratospheric water vapor. *Mon. Weather Rev.*, 111:1397, 1983.

[21] A. Fried, Drummond. J.R., and B. Henry. Versatile integrated tunable diode-laser system for high-precision-application for ambient measurements of OCS. *Appl. Optics*, 30:1916–1932, 1991.

[22] M.R. Gunson et al. The atmospheric trace molecular spectroscopy (ATMOS) experiment deployment on the ATLAS-3 space shuttle mission. *Geophys. Res. Lett.*, 23, 1996.

[23] R. Hageman et al. Absolute d/h ratio for smow. *Tellus*, 22:712, 1970.

[24] J. Hansen et al. The greenhouse effect of chlorofluorocarbons and other trace gases. *J. Geo. Res.*, 94:16417, 1989.

[25] J.E. Harries. The greenhouse earth: a view from space. *Q. J. R. Meteo. Soc.*, 122:799, 1996.

[26] D. Heriott, H. Kogelnik, and R. Kompfner. Off-axis paths in spherical mirror interferometers. *Appl. Optics*, 3:523–526, 1964.

[27] R.L. Herman. *In-situ measurements of chemical tracers in the stratosphere: CO, N_2O, and CH_4*. PhD thesis, California Institute of Technology, 1998.

[28] R.L. Herman, C.R. Webster, R.D. May, D.C. Scott, H. Hu, E.J. Moyer, P.O. Wennberg, T.F. Hanisco, E.J. Lanzendorff, R.J. Salawitch, Y.L. Yung, J.J. Margitan, and T.P. Bui. Measurements of CO in the upper troposphere and lower stratosphere. *Chemosphere*, 1:1, 1998.

[29] J.R. Holton, P.H. Haynes, M.E. McIntyre, A.R. Douglass, R.R. Rood, and L. Pfister. Stratosphere-troposphere exchange. *Reviews of Geophysics*, 33:403–439, 1995.

[30] R.A. Houze. Observed structure of mesoscale convective systems and implications for large-scale heating. *Q. J. R. Meteo. Soc.*, 115:425, 1989.

[31] F.W. Irion et al. Stratospheric observations of C_3D and HDO from ATMOS infrared solar spectra: enrichments of deuterium in methane and implications for HD. *Geophys. Res. Lett.*, 23, 1996.

[32] H. Jost, M. Loewenstein, and L. Pfister. Laminae in the tropical middle stratosphere: origin and age estimation. *Geophys. Res. Lett.*, 25:4337–4340, 1998.

[33] J. Jouzel and L. Merlivat. Deuterium and oxygen-18 in precipitation: modeling of the isotopic effects during snow formation. *J. Geo. Res.*, 89:11749, 1984.

[34] D.W. Keith. Stratosphere-troposphere exchange: inferences from the isotopic composition of water vapor. *J. Geo. Res.*, 105:15167–15173, 2000.

[35] R.G. Knollenberg et al. Measurements of high number densities of ice crystals in the tops of tropical cumulonimbus. *J. Geo. Res.*, 98:8639, 1993.

[36] W. Kouker et al. Streamers observed by the CRISTA experiment and simulated in the KASIMA model. *J. Geo. Res.*, 104:16405–16418, 1999.

[37] M.A. Kritz et al. Radon measurements in the lower tropical stratosphere: evidence for rapid vertical transport and dehydration of tropical air. *J. Geo. Res.*, 98:8725–8736, 19919933.

[38] W.A. Lahoz et al. Vortex dynamics and the evolution of water vapour in the stratosphere of the southern hemisphere. *Q. J. R. Meteo. Soc.*, 122:423–450, 1996.

[39] C.B. Leovy, C.R. Sun, M.H. Hitchman, E.E. Remsberg, J.M. Russell, L.L. Gordley, J.C. Gille, and L.V. Lyjak. Transport of ozone in the middle stratosphere: evidence for planetary wave breaking. *J. Atmos. Sci.*, 42:230–244, 1985.

[40] M. Majoube. Fractionation of oxygen 18 and of deuterium between water and its vapor. *J. Chem. Phys.*, 68:1423, 1971.

[41] R.D. May. Open-path, near-infrared tunable diode laser spectrometer for atmospheric measurements of H_2O. *J. Geo. Res.*, 103:19161–19172, 1998.

[42] G.M. McFarquhar, A.J. Heymsfield, J. Spinhirne, and B. Hart. Thin and subvisual tropopause tropical cirrus: observations and radiative impacts. *J. Atmos. Sci.*, 57:1841–1853, 2000.

[43] M.E. McIntyre and T.N. Palmer. Breaking planetary waves in the stratosphere. *Nature*, 305:593–600, 1983.

[44] L. Merlivat and G. Nief. Isotopic fractionation of the solid-vapor and liquid-vapor changes of state of water at temperatures below 0c. *Tellus*, 19:122, 1967.

[45] P.W. Mote, K.H. Rosenlof, M.E. McIntyre, et al. An atmospheric tape recorder: the imprint of tropical tropopause temperatures on stratospheric water vapor. *J. Geo. Res.*, 101:3989–4006, 1996.

[46] E.J. Moyer, F.W. Irion, Y.L. Yung, and M.R. Gunson. ATMOS stratospheric deuterated water and implications for troposphere-stratosphere transport. *Geophys. Res. Lett.*, 23:2385–2388, 1996.

[47] R.E. Newell and S. Gould-Stewart. A stratospheric fountain? *J. Atmos. Sci.*, 38:2789–2796, 1981.

[48] P.A. Newman, D.W. Fahey, W.H. Brune, and M.J. Kurylo. Photochemistry of ozone loss in the arctic region in summer (POLARIS) CACGP/IGAC 1998 symposium - preface. *J. Geo. Res.*, 104:26481–26496, 1999.

[49] R.A. Plumb, D.W. Waugh, R.J. Atkinson, P.A. Newman, L.R. Lait, M.R. Schoeberl, E.V. Browell, A.J. Simmons, and M. Loewenstein. Intrusions into the lower

stratospheric arctic vortex during the winter 1991-1992. *J. Geo. Res.*, 99:1089–1105, 1994.

[50] J. Podolske and M. Loewenstein. Airborne tunable diode-laser spectrometer for trace-gas measurement in the lower stratosphere. *Appl. Optics*, 32:5324–5333, 1993.

[51] W. Pollock et al. Measurement of stratospheric water vapor by cryogenic collection. *J. Geo. Res.*, 85:5555, 1980.

[52] B.E. Potter and J.R. Holton. The role of monsoon convection in dehydration of the lower tropical stratosphere. *J. Atmos. Sci.*, 52:1034, 1994.

[53] H.R. Pruppacher and J.D. J.D. Klett. *Microphysics of clouds and precipitation.* D. Reidel Co., New York, 1980.

[54] V. Ramanathan and W. Collins. Thermodynamic regulation of ocean warming by cirrus clouds deduced from observations of the 1987 El Nino. *Nature*, 351:27, 1991.

[55] W.J. Randel, J.C. Gille, A.E. Roche, J.B. Kumer, J.L. Mergethaler, J.W. Waters, E.F. Fishbein, and W.A. Lahoz. Stratosheric transport from the tropics to middle latitudes by planetary-wave mixing. *Nature*, 365:533–535, 1993.

[56] E.A. Ray, F.L. Moore, J.W. Elkins, et al. Transport into the northern hemisphere lowermost stratosphere revealed by in situ tracer measurements. *J. Geo. Res.*, 104:26565–26580, 1999.

[57] H. Riehl and J. S. Malkus. On the heat balance in the equatorial trough zone. *Geophysica*, 6:503, 1958.

[58] C.P. Rinsland et al. Simultaneous stratospheric measurements of H_2O, HDO, and CH_4 from balloon-borne and aircraft infrared solar absorption spectra and tunable diode laser laboratory spectra. *J. Geo. Res.*, 89:7259, 1984.

[59] C.P. Rinsland et al. Stratospheric profiles of heavy water isotopes and CH_3D from analysis of the ATMOS Spacelab 3 infrared solar spectra. *J. Geo. Res.*, 96:1057, 1991.

[60] G.D. Robinson. The transport of minor atmospheric constituents between troposphere and stratosphere. *Q. J. R. Meteo. Soc.*, 106:227–253, 1980.

[61] R.R. Rogers and M.K. Yau. *A short course in cloud physics.* Pergamon Press, New York, 1989.

[62] K.H. Rosenlof. The seasonal cycle of the residual mean meridional circulation in the stratosphere. *J. Geo. Res.*, 100:5173–5191, 1995.

[63] K.H. Rosenlof and J.R. Holton. Estimates of the stratospheric residual circulation using the downward control principle. *J. Geo. Res.*, 98:10465–10479, 1993.

[64] L.S. Rothman, R.R. Gamache, A. Goldman, L.R. Brown, R.A. Toth, H.M. Pickett, R.L. Poynter, et al. The HITRAN database: 1986 edition. *Appl. Optics*, 26:4058–4097, 1987.

[65] L.S. Rothman, R.R. Gamache, R.H. Tipping, C.P. Rinsland, et al. The HITRAN molecular database: editions of 1991 and 1992. *J. Quant. Spectrosc. Radiat. Transfer*, 48:469–507, 1992.

[66] G.W. Sachse, G.F. Hill, L.O. Wade, and M.G. Perry. Fast-response, high-precision carbon-monoxide sensor using a tunable diode-laser absorption technique. *J. Geo. Res.*, 92:2071–2081, 1987.

[67] D.C. Scott, R.L. Herman, C.R. Webster, R.D. May, G.J. Flesch, and E.J. Moyer. Airborne laser infrared absorption spectrometer (ALIAS-II) for *in-situ* atmospheric measurements of N_2O, CH_4, CO, HCl, and NO_2 from balloon or remotely piloted aircraft platforms. *Appl. Optics*, 38:4609–4622, 1999.

[68] S.C. Sherwood and A.E. Dessler. A model for transport across the tropical tropopause. *J. Atmos. Sci.*, 58:765–779, 2001.

[69] C.B. Taylor et al. The vertical variations of the isotopic concentrations of tropospheric water vapour over continental europe and their relationship to tropospheric structure. Technical report, Rep. N. Z. Dep. Sci. Ind. Res., Inst. Nucl. Sci., 1972.

[70] C.R. Trepte et al. The poleward dispersal of Mt. Pinatubo aerosol. *J. Geo. Res.*, 98:18563–18573a, 1993.

[71] A.E. Tuck et al. Intercomparison of HALOE and ER-2 H_2O and CH_4 observations collected during AASE II. *Geophys. Res. Lett.*, 20:1299–1302, 1992.

[72] P.H. Wang, P. Minnis, M.P. McCormick, G.S. Kent, and K.M. Skeens. A 6-year climatology of cloud occurrence frequency from Stratospheric Aerosol and Gas Experiment II observations (1985-1990). *J. Geo. Res.*, 101:29407–29429, 1996.

[73] D.W. Waugh. Seasonal variation of isentropic transport out of the tropical stratosphere. *J. Geo. Res.*, 101:4007–4023, 1996.

[74] D.W. Waugh, R.A. Plumb, P.A. Newman, M.R. Schoeberl, L.R. Lait, M. Loewenstein, J.R. Podolske, J.W. Elkins, and K.R. Chan. Fine-scale, poleward transport of tropical air during AASE 2. *Geophys. Res. Lett.*, 21:2603–2606, 1994.

[75] D.W. Waugh, W.J. Randel, S. Pawson, P.A. Newman, and E.R. Nash. Persistence of the lower stratospheric polar vortices. *J. Geo. Res.*, 104:27191–27201, 1999.

[76] C.R. Webster, R.D. May, C.A. Trimble, R.G. Chave, and J. Kendall. Aircraft (ER-2) laser infrared absorption spectrometer (ALIAS) for *in-situ* stratospheric measurements of HCl, N_2O, CH_4, NO_2, AND HNO_3. *Appl. Optics*, 33:453–472, 1994.

[77] E.M. Weinstock, E.J. Hintsa, D.B. Kirk-Davidoff, J.G. Anderson, A.E. Andrews, R.L. Herman, C.R. Webster, M. Loewenstein, J.R. Podolske, and T.P. Bui. Constraints

on the seasonal cycle of stratospheric water vapor using *in situ* measurements from the ER-2 and a CO photochemical clock. *J. Geo. Res.*, (accepted), 2001.

[78] P.O. Wennberg et al. Aircraft-borne, laser-induced fluroescence instrument for the *in situ* detection of hydroxyl and hydroperoxyl radicals. *Rev. Sci. Inst.*, 65:1858–1876, 1994.

[79] Y.L. Yung, C. Shia, and R.L. Herman. Is the biomass burning source of CO decreasing? *Chemosphere*, 1:83–90, 1999.